TU WIEN
DEPARTMENT OF GEODESY
AND GEOINFORMATION
RESEARCH UNITS
PHOTOGRAMMETRY & REMOTE SENSING

DISSERTATION

Advancing the understanding of active microwave remote sensing of soil moisture and vegetation

Ausgeführt zum Zwecke der Erlangung des akademischen Grades einer

Doktorin der technischen Wissenschaften (Dr.techn.)

Unter der Leitung von

Univ.Prof. Dipl.-Ing. Dr.techn. Wolfgang Wagner

E120.1

Department für Geodäsie und Geoinformation

Forschungsgruppe Fernerkundung

Eingereicht an der Technischen Universität Wien

Fakultät für Mathematik und Geoinformation

von

Dipl.Ing.[in] Isabella Greimeister-Pfeil

Matrikelnummer: 01026550

Wien, Österreich, 20. Juli 2022

Isabella Greimeister-Pfeil

DISSERTATION

Advancing the understanding of active microwave remote sensing of soil moisture and vegetation

A thesis submitted in fulfilment of the academic degree of

Doktorin der technischen Wissenschaften (Dr.techn.)

Under the supervision of

Univ.Prof. Dipl.-Ing. Dr.techn. Wolfgang Wagner

E120.1

Department of Geodesy and Geoinformation

Research Group Remote Sensing

Research conducted at TU Wien

Faculty of Mathematics and Geoinformation

by

Dipl.Ing.[in] Isabella Greimeister-Pfeil

Matriculation number: 01026550

Vienna, Austria, July 20, 2022

Isabella Greimeister-Pfeil

Supervisor: **Prof. Dr. Wolfgang Wagner**
TU Wien
Department of Geodesy and Geoinformation
Research Group Remote Sensing
Wiedner Hauptstraße 8/E120.1, 1040 Vienna, Austria
E-Mail: wolfgang.wagner@geo.tuwien.ac.at

Referees: **Prof. Dr. Günter Blöschl**
TU Wien
Faculty of Civil Engineering
Institute of Hydraulic Engineering and Water Resources Management
Karlsplatz 13, 1040 Vienna, Austria
E-Mail: bloeschl@hydro.tuwien.ac.at

      JProf. Dr. Matthias Forkel
TU Dresden
Institute of Photogrammetry and Remote Sensing
Helmholtzstr. 10, 01069 Dresden, Germany
E-Mail: matthias.forkel@tu-dresden.de

Isabella Greimeister-Pfeil

Advancing the understanding of active microwave remote sensing of soil moisture and vegetation

Dissertation, July 20, 2022

TU Wien

Department of Geodesy and Geoinformation

Research Group Remote Sensing

Wiedner Hauptstraße 8/E120.1, A-1040 Vienna, Austria

Erklärung zur Verfassung der Arbeit – Author's Statement

Hiermit erkläre ich, dass ich diese Arbeit selbstständig verfasst habe, dass ich die verwendeten Quellen und Hilfsmittel vollständig angegeben habe und dass ich die Stellen der Arbeit – einschließlich Tabellen, Karten und Abbildungen – die anderen Werken oder dem Internet im Wortlaut oder dem Sinn entnommen sind, auf jeden Fall unter Angabe der Quelle als Entlehnung kenntlich gemacht habe.

I hereby declare that I independently drafted this manuscript, that all sources and references are correctly cited, and that the respective parts of this manuscript - including tables, maps, and figures - which were included from other manuscripts or the internet either semantically or syntactically are made clearly evident in the text and all respective sources are correctly cited.

Wien, Österreich, 20. Juli 2022

Isabella Greimeister-Pfeil

Abstract

Active microwave remote sensing techniques provide a means for the monitoring of biogeophysical variables over land, independent of weather and cloud conditions and daylight. Several missions are in place nowadays which provide regular observations of the entire Earth surface. Observations provided by these sensors have for example been used for the retrieval of soil moisture (SM) and vegetation optical depth, a measure of canopy water content, density and structure. Some of these datasets are available publicly and on an operational basis. Despite the long history of active microwave remote sensing research, going back into the 1960s, there is a constant need to extend the understanding of how active microwave sensors perceive the land surface on the respective spatial scale of the satellite observations.

The aim of this thesis was to study the multi-angular backscatter signal ($\sigma°$) observed by the Advanced Scatterometer (ASCAT) sensor over the land surface. The focus was on the backscatter dependence on the incidence angle (σ'), as this relationship is crucial for the separation of SM and vegetation effects on the observed signal. Thereby, I aimed at advancing the understanding of how SM and vegetation dynamics influence $\sigma°$ and σ' on the relatively coarse spatial scale of the ASCAT footprint. The main objectives can be summed up as follows: i) increase the understanding of the ASCAT backscatter incidence-angle relationship, in particular the first derivative σ', ii) investigate the potential of a regional adjustment of parameter values for SM and vegetation optical depth retrieval, iii) improve the understanding of structural effects of vegetation canopies on σ', and iv) reassess the assumption that σ' is not or only weakly affected by SM.

The conducted research highlighted the great potential of the coarse-scale ASCAT sensor for the retrieval of biogeophysical variables such as SM and vegetation dynamics. One main new finding was that ASCAT is highly sensitive to the water uptake of deciduous broadleaf trees in early spring, allowing for the monitoring of spring reactivation in deciduous forests across wide regions, potentially even on a global level. Thanks to the increasing temporal coverage, (ASCAT) backscatter time series may be exploited for the study of growing season shifts as a reaction to climate change. The study clearly showed that canopy structure can have large effects on ASCAT observations, even if the responsible vegetation type makes up only a small fraction of the entire footprint.

The thesis also revealed potentials for improvements in existing retrieval algorithms, such as the benefits of a stronger vegetation correction for the retrieval of SM in temperate-climate, agricultural regions. Moreover, it was shown that despite the clear and dominant control of σ' by vegetation dynamics, there are short-term secondary effects in σ' caused by SM, which need to be taken into account when interpreting σ' time series or applying σ' as vegetation dynamics indicator.

The results of the thesis show that future studies of ASCAT $\sigma°$ and its dependence on the incidence angle should be set up as broad as possible in order to take into account the numerous variables and processes that ASCAT is sensitive to, including combined effects that might cancel each other out or reinforce each other. However, detailed studies of selected processes will always be necessary in order to understand how individual components contribute to the signal.

High resolution backscatter datasets, for example provided by Sentinel-1, and enhanced observation techniques, for example foreseen for the upcoming Metop-SG missions, ensure the availability of long backscatter time series, and open up new possibilities for investigating, understanding and monitoring backscatter from land surfaces. This thesis shall contribute to these efforts and support the way forward by shedding light on topics that were not studied in detail previously.

Kurzfassung

Die aktive Mikrowellenfernerkundung bietet eine Möglichkeit zur Beobachtung biogeophysikalischer Variablen über Land, unabhängig von Wetter- und Wolkenbedingungen und Tageslicht. Es gibt heute bereits mehrere Missionen, die regelmäßige und konsistente Beobachtungen der gesamten Erdoberfläche liefern. Die von aktiven Mikrowellensensoren gelieferten Beobachtungen werden beispielsweise für die Ermittlung der Bodenfeuchtigkeit und der optischen Tiefe der Vegetation (VOD), einem Maß für den Wassergehalt, die Dichte und die Struktur der Vegetation, verwendet. Einige dieser Datensätze sind öffentlich und auf operationeller Basis verfügbar. Trotz der langen Geschichte der aktiven Mikrowellenfernerkundung, die bis in die 1960er Jahre zurückreicht, besteht ein ständiger Bedarf, das Verständnis dafür zu verbessern, wie aktive Mikrowellensensoren die Landoberfläche auf der jeweiligen räumlichen Skala der Satellitenbeobachtungen wahrnehmen.

Ziel dieser Arbeit war es, das vom Advanced Scatterometer (ASCAT)-Sensor über der Landoberfläche beobachtete multi-angulare Rückstreusignal (σ°) zu untersuchen. Der Schwerpunkt lag dabei auf der Abhängigkeit des Rückstreukoeffizienten vom Einfallswinkel (σ'), da diese Beziehung entscheidend für die Trennung von Bodenfeuchte- und Vegetationseffekten auf das beobachtete Signal ist. Auf diese Weise wurde das Verständnis dafür verbessert, wie Bodenfeuchte und Vegetationsdynamik σ° und σ' auf der relativ groben räumlichen Skala des ASCAT-Footprints beeinflussen. Die Hauptziele der Arbeit lassen sich wie folgt zusammenfassen: i) die Verbesserung des Verständnisses der Abhängigkeit des ASCAT-Rückstreukoeffizienten vom Einfallswinkel, insbesondere der ersten Ableitung σ' dieser Abhängigkeit, ii) die Untersuchung des Potenzials einer regionalen Anpassung der Parameterwerte für die Berechnung von Bodenfeuchte und VOD, iii) die Verbesserung des Verständnisses der Auswirkungen der Vegetationsstruktur auf σ', und iv) die Neubewertung der Annahme, dass σ' nicht oder nur schwach durch die Bodenfeuchte beeinflusst wird.

Die durchgeführten Studien unterstrichen das große Potenzial des ASCAT-Sensors für die Erfassung biogeophysikalischer Variablen wie Bodenfeuchte und Vegetationsdynamik. Eine wichtige neue Erkenntnis war, dass ASCAT sehr empfindlich auf die Wasseraufnahme von Laubbäumen im Frühjahr reagiert, was die Beobachtung des

Beginns der Vegetationsperiode in Laubwäldern über weite Regionen, möglicherweise sogar auf globaler Ebene, ermöglicht. Dank der zunehmenden zeitlichen Abdeckung können (ASCAT-)Rückstreuzeitreihen somit für die Untersuchung von Verschiebungen der Wachstumsperiode im Laubwald als Reaktion auf den Klimawandel genutzt werden. Die Studie hat deutlich gezeigt, dass die Vegetationsstruktur große Auswirkungen auf ASCAT-Beobachtungen haben kann, selbst wenn die betreffende Vegetationsart nur einen kleinen Teil der gesamten Fläche ausmacht.

Die Arbeit zeigte auch Verbesserungsmöglichkeiten für bestehende Algorithmen auf, wie z.B. die Vorteile einer stärkeren Vegetationskorrektur für die Ableitung von Bodenfeuchte in landwirtschaftlich genutzten Regionen mit gemäßigtem Klima. Darüber hinaus wurde gezeigt, dass es trotz der eindeutigen und dominanten Kontrolle von σ' durch die Vegetationsdynamik kurzfristige sekundäre Effekte in σ' gibt, die durch die Bodenfeuchte verursacht werden und die bei der Interpretation von σ'-Zeitreihen oder der Anwendung von σ' als Indikator für die Vegetationsdynamik berücksichtigt werden müssen.

Die Ergebnisse der Arbeit zeigen, dass künftige Untersuchungen des ASCAT-Rückstreukoeffizienten und seiner Abhängigkeit vom Einfallswinkel so breit wie möglich angelegt sein sollten, um die zahlreichen Variablen und Prozesse zu berücksichtigen, die das Signal beeinflussen, einschließlich kombinierter Effekte, die sich gegenseitig aufheben oder verstärken können. Detaillierte Studien ausgewählter Prozesse werden jedoch weiterhin notwendig sein, um jede einzelne Komponente zu verstehen, die zum Signal beiträgt.

Hochauflösende Rückstreudatensätze, wie sie z.B. von Sentinel-1 geliefert werden, und verbesserte Beobachtungstechniken, wie sie für die kommenden Metop-SG-Missionen vorgesehen sind, gewährleisten die Verfügbarkeit langer Rückstreuzeitreihen und eröffnen neue Möglichkeiten für die Erforschung, das Verständnis und das Monitoring der Rückstreueigenschaften von Landoberflächen. Die vorliegende Arbeit soll einen Beitrag zu diesen Bemühungen leisten und zukünftige Studien unterstützen, indem sie Themen beleuchtet, die bisher nicht im Detail untersucht wurden.

Acknowledgement

Doing a PhD is like going on a long train ride. You start by asking yourself if it's worth going on the trip, knowing that there might be some times of struggle, delays, and unclear turnouts, but that the end will be very rewarding and you will have made so many new experiences along the way. Six years ago, I decided to go on this journey, and would like to express my gratitude to everybody who I met and who supported me along the way.

I would like to thank the people who were next to me in the wagon. That is first of all my supervisor, Wolfgang Wagner – thank you for your scientific guidance and support, for sharing your vast experience, and also for encouraging me to submit my papers when I was still looking for the perfect final touch for the hundredth time. Thank you also for giving me the opportunity to participate in a number of conferences inside and outside of Austria, which were all very beneficial for my work and personal development. I would also like to thank all colleagues of our research groups – microwave remote sensing, CLIMERS, and photogrammetry. It was a wonderful experience to work together with you on so many projects, and to share our common love of science but sometimes also our frustration. My special thanks go to Mariette Vreugdenhil, who always had an open ear for my questions and new ideas when I seemed to have got stuck. I really enjoyed working on projects together and value very much the knowledge that I gained from your experience in so many different topics. I would also like to thank the two referees, Günter Blöschl and Matthias Forkel, for their support during certain phases of my PhD, and their willingness to be the ticket inspectors at the end of the trip.

A big thank you goes to everybody who joined me in the Speisewagen – my family and friends who supported me during the last few years and helped me to get my head off work. Thank you to my parents, Edith and Klaus, my sister Victoria and my brother Max, for your unconditional support, for conversations about my research, and for making me explain and question my work. Mostly however I would like to thank you for always being there and providing me with fresh energy and courage to take the next steps, and for all the understanding we have for each other.

Music has always been a part of my life, but during the last three years, singing with my vocal group Routes and Roots has become an indispensable activity that

has brought me so much joy and helped me refresh my brain. Thank you guys for your support and understanding at all times! A big thank you also to my OÖ Mädels, Rasselbande, Sävelmä-Ladies... for all the fun, advice, and swapped clothes :)

My largest thank you goes to my husband Patrick. Thank you for always providing me with a safe and calm place at home, thank you for making me laugh so much, and thank you for your support during the last years – not only related to my PhD but also to all the other big adventures that we took on together. I'm excited to see where our next journey(s) will take us.

(And yes, this text was written on a beautiful train ride.)

Contents

List of Figures

List of Tables

Introduction

<div style="text-align:right">

1

</div>

> *Science makes people reach selflessly for truth*
> *and objectivity; it teaches people to accept reality,*
> *with wonder and admiration, not to mention the*
> *deep awe and joy that the natural order of things*
> *brings to the true scientist.*

— **Lise Meitner**
(Austrian nuclear physicist)

1.1 Motivation and problem statement

In December 1968, Bill Anders, a NASA astronaut and member of the Apollo-8 crew, took a picture that would later be seen as a milestone in the history of Earth observation (Figure 1.1). The iconic picture shows the Earth coming up from beyond the lunar surface, and it has inspired the development of ever and ever improving methods for observing and monitoring Earth from space. More than 50 years later, monitoring the status of the marine and terrestrial ecosystems on our planet is as important as ever, especially in order to protect them from the many challenges and threats they are exposed to. Just as in 1968, this is – amongst a number of other techniques – still done by taking "remote pictures" from space, however, nowadays several types of sensors in addition to cameras exist.

In this thesis, the focus is on remote sensing of terrestrial ecosystems using an active microwave sensor. Microwaves differ from optical waves in their wavelength and their very special characteristic to sustain oriental polarization of water molecules, making them highly sensitive to the presence of water in the sensor footprint. Over land, microwave measurements allow the derivation of soil moisture status and vegetation water content. Active microwave sensors, i.e., sensors that measure the backscattered fraction of a previously transmitted electromagnetic wave, include scatterometers and synthetic aperture radars (SAR). SARs have the advantage of enabling measurements with a high spatial resolution (around 10 m), however,

Fig. 1.1: "Earthrise", taken aboard Apollo-8 by Bill Anders (December 24, 1968). Image Credit: NASA.
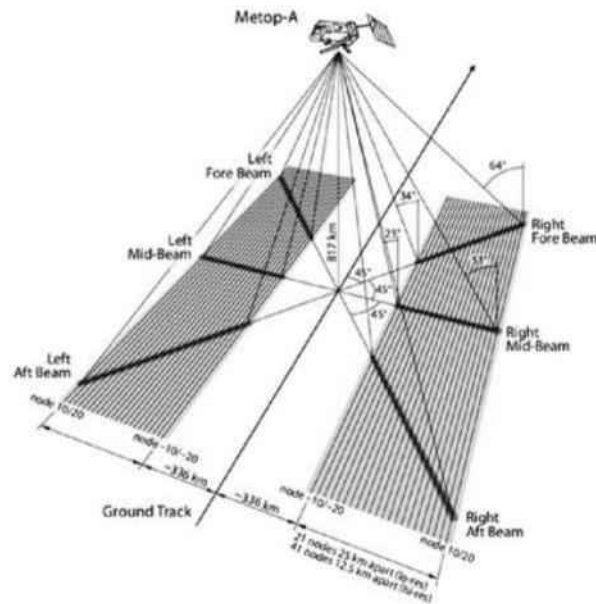
Fig. 1.2: Multi-angular observation geometry of the Metop ASCAT sensor (Wagner et al., 2013).

this comes at a reduced temporal coverage. Scatterometers have footprints of several km^2, but provide measurements of the same location with a frequency of a few days or higher. Despite the coarse spatial resolution, scatterometer observations are very useful in the context of environmental remote sensing as many climatic, meteorological and ecological processes occur at a regional scale and are highly dynamic in time. The aim of the research presented within this thesis was to study in detail the multi-angular backscatter signal measured by the C-band scatterometer on-board the Metop satellites (*ASCAT*; Figure 1.2), and thereby advance the understanding of how soil moisture (SM) and vegetation dynamics influence the signal on a coarse scale. The following paragraphs give an overview of the basic principles and assumptions in active C-band microwave remote sensing that this thesis builds upon.

Influences on C-band backscatter measurements An observed backscatter value (σ°) depends on the characteristics of the land surface in the sensor footprint and the different scattering mechanisms that are activated. This, in turn, is primarily controlled by the sensor's frequency and polarization, and the incidence angle of the observation (Ulaby et al., 1981). In the case of bare soil, the radiation is reflected on the surface, and with increasing surface roughness, a larger part of the radiation is scattered back to the sensor. If a surface appears rough or smooth to a scatterometer is defined by the size of the surface height variations relative to the wavelength of the radar beam. In addition, the soil water content plays a fundamental role, as wet soil increases σ° due to its high dielectric constant and consequently higher scattering strength. As opposed to bare soil, a vegetation canopy appears as an inhomogeneous medium with a higher penetration depth, which scatters the incident radiation diffusely in all directions. In this case, the backscattered radiation fraction depends less on the incidence angle. Over vegetation, C-band radiation is typically scattered mostly by plant constituents in the order of a few centimetres, e.g., twigs and small branches of trees, and crop stems, leaves and heads.

Coarse-scale footprints & heterogeneous land cover Due to the coarse spatial resolution, each ASCAT footprint covers several different land cover types in most regions. Each backscatter measurement is thus a combination of the individual scatterers in the footprint, including bare soil and vegetation canopies. The semi-empirical TU Wien change detection model has been developed to disentangle SM and vegetation effects in the backscatter signal, making use of the different scattering mechanisms that are activated and which affect backscatter differently depending on the incidence angle of the observation (Wagner et al., 1999b; Wagner et al., 1999c; Wagner et al., 1999a; Vreugdenhil et al., 2016; Hahn et al., 2017). This model with
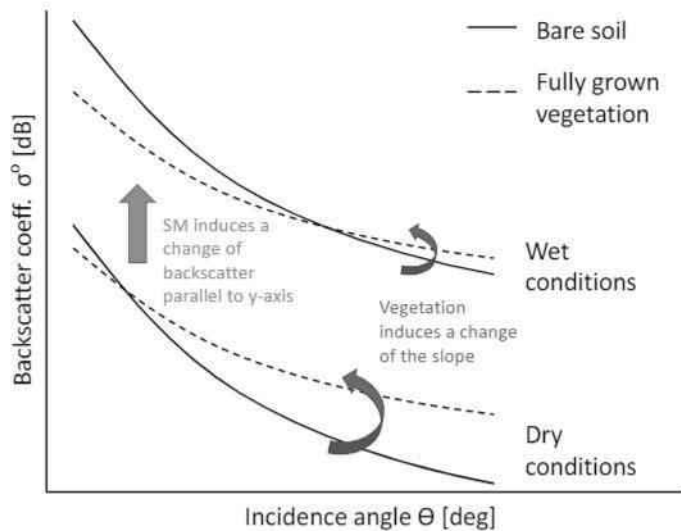
Fig. 1.3: Dependence of the backscatter coefficient on the incidence angle under dry and wet conditions, for bare soil and fully grown vegetation (after Wagner et al. (1999c)).

globally defined parameters works well in general, but can be improved when tuned to regional land surface characteristics (Hahn et al., 2020).

Incidence angle dependence As stated above, SM and vegetation effects on σ° vary depending on the incidence angle of an observation (θ). Whereas backscatter from bare soils depends highly on the incidence angle and drops quickly with increasing θ due to increased scattering away from the sensor, backscatter from vegetation canopies is high across a large range of incidence angles (Figure 1.3). This dependence, which is often formulated using the first and second derivatives (slope σ', curvature σ'') of a second-order Taylor polynomial fit to the σ°-θ-relationship, can be used to separate SM and vegetation effects in σ°. σ' and σ'' can be robustly estimated for each day based on ASCAT observations from a few weeks (Melzer, 2013; Hahn et al., 2017). The temporal dynamics of σ' have been shown to be highly correlated with vegetation development (Vreugdenhil et al., 2017; Steele-Dunne et al., 2019).

Retrieval of biogeophysical variables from C-band backscatter The TU Wien change detection model has been developed to retrieve SM from the scatterometers on board of the European remote sensing satellites (Wagner et al., 1999b), and was later adapted and improved for ASCAT (Naeimi et al., 2009b). Many studies have evaluated the ASCAT SM product over different regions and found high correlations with in-situ measurements of SM. The model makes use of ASCAT's multi-angular backscatter observations, and more specifically the thereof derived σ' and σ'' of the σ°-θ-relationship, to correct for the vegetation component in the backscatter

signal (Hahn et al., 2017). It has been shown that this vegetation characterization can be converted into vegetation optical depth (τ) (Vreugdenhil et al., 2016), which is an indicator of the vegetation water content, and both the leaf and woody components of the total above-ground biomass (Liu et al., 2011).

1.2 Study objectives

Despite the extensive research foundation in the topic of remote sensing of SM and vegetation using scatterometers, open questions remain. The focus of this thesis is on selected aspects related to ASCAT's sensitivity to vegetation dynamics and the complex combined representation of SM and vegetation in $\sigma°$ and σ'.

The overall aim is to further advance the understanding of vegetation and soil moisture effects on C-band backscatter. To do so, different analyses are conducted using ASCAT backscatter timeseries. The main objectives of the thesis can be summed up as follows:

- Increase the understanding of the ASCAT backscatter incidence-angle relationship, in particular the first derivative (σ')

- Investigate the potential of a regional adjustment of parameter values for SM and vegetation optical depth retrieval

- Improve the understanding of structural effects of vegetation canopies on σ'

- Reassess the assumption that σ' is not or only weakly affected by SM

These objectives were addressed in three studies, aiming at answering the following research questions.

1.3 Research questions and summary of results

Article 1: Does the ASCAT surface soil moisture product benefit from a stronger vegetation correction in a temperate-climate, agricultural region?

The ASCAT SM product has been found to be of high quality in several validation studies. However, over- and underestimation of SM during different times of the year suggest a need for improving the retrieval algorithm. We analyzed whether adapting the vegetation characterization improves the seasonal representation of SM

and vegetation optical depth (τ). Therefore, we compared SM and τ retrieved from ASCAT using a weaker and a stronger vegetation correction, as well as including and excluding inter-annual dynamics (σ'_{dyn}, σ'_{clim}). The study was conducted for a region in Austria with predominantly agricultural land use. We found that a stronger vegetation correction improves the retrieved SM dataset considerably. The vegetation product derived with a dynamic vegetation characterization compares well to the reference datasets and reflects vegetation dynamics such as start and peak of season and harvest.

Two findings of this study were unexpected. First, a characteristic peak was observed in the σ'_{dyn} timeseries each year around March/April that could not be linked to the typical crop growing cycles of the study region. Second, including inter-annual dynamics in the vegetation correction, i.e., using σ'_{dyn} instead of σ'_{clim}, did not lead to an improvement of the SM product. These two observations were investigated in two follow-up studies.

Article 2: Does ASCAT observe the spring reactivation in deciduous broadleaf forest?

The aim of the second study was the investigation of the characteristic peak in σ'_{dyn} that was observed in the agricultural study region of the first study. Therefore, a peak detection method was developed and applied over central Europe, revealing that the characteristic peak occurred predominantly over areas with deciduous broadleaf forest cover. As the peak occurred around March/April each year, we investigated if it was caused by leaf emergence by comparing σ'_{dyn} timeseries with phenological observations, temperature data, and satellite-derived leaf area index. We found that the peak was indeed linked to ecophysiological processes. We concluded that water uptake of deciduous trees in preparation for leaf emergence causes a strong scattering effect that ASCAT is sensitive to, followed by an attenuation of the scattering effect due to the growing canopy.

Article 3: Are short-term variations in the ASCAT backscatter-incidence angle slope caused by soil moisture?

In a third study, we investigated a potential SM effect on σ'_{dyn}. Radiative transfer models suggested the presence of such an effect, however, the effect has been assumed to be weak and negligible in the context of SM retrieval based on early studies with limited data availability. We exploited the long backscatter timeseries

available from the Metop satellites in order to investigate correlations between σ', SM, and leaf area index. The results clearly indicate that there is a secondary, short-term SM effect in σ'_{dyn} on top of the dominant vegetation signal. The SM effect is lowest over dense forest and strongest over sparse vegetation cover, where it can be as large as a fifth of the total annual variation of σ'_{dyn}. Short-term secondary effects are mitigated when using a climatology slope (σ'_{clim}) due to long-term averaging, which is the case in the operational ASCAT SM product. However, σ' must be used with caution in vegetation studies that look at interannual variability.

1.4 Relevant publications and author contributions

The conducted analyses and results of this thesis have been presented to the scientific community in the form of three research articles and seven conference contributions, which are listed in the following.

Research articles

1. Pfeil, I., Vreugdenhil, M., Hahn, S., Wagner, W., Strauss, P., & Blöschl, G. (2018). Improving the seasonal representation of ASCAT soil moisture and vegetation dynamics in a temperate climate. *Remote Sensing*, 10(11), 1788.

   Author contributions: I. Greimeister-Pfeil conceived and designed the experiments together with M. Vreugdenhil, S. Hahn, and W. Wagner. I. Greimeister-Pfeil analyzed the data, and wrote the manuscript. P. Strauss and G. Blöschl contributed their expertise. All authors participated in the proof reading and revision of the manuscript.

2. Pfeil, I., Wagner, W., Forkel, M., Dorigo, W., & Vreugdenhil, M. (2020). Does ASCAT observe the spring reactivation in temperate deciduous broadleaf forests?. *Remote Sensing of Environment*, 250, 112042.

   Author contributions: I. Greimeister-Pfeil conceived and designed the experiments, analyzed the data and wrote the manuscript. W. Wagner and M. Vreugdenhil were the supervisors. M. Forkel and W. Dorigo helped with scientific discussions. All authors participated in the proof reading and revision of the manuscript.

3. Greimeister-Pfeil, I., Wagner, W., Quast, R., Hahn, S., Steele-Dunne, S., & Vreugdenhil, M. (2022). Analysis of short-term soil moisture effects on the ASCAT backscatter-incidence angle dependence. Science of Remote Sensing, 100053.

   Author contributions: Conceptualization, I. Greimeister-Pfeil and W. Wagner; methodology, I. Greimeister-Pfeil, W. Wagner, M. Vreugdenhil, S. Hahn, S. Steele-Dunne, R. Quast; investigation, I. Greimeister-Pfeil; visualization, I. Greimeister-Pfeil; writing—original draft preparation, I. Greimeister-Pfeil; writing—review and editing, all authors. All authors have read and agreed to the published version of the manuscript.

Relevant conference contributions

1. Pfeil, I. M., Vreugdenhil, M., Strauss, P., Oismueller, M., Wagner, W., & Bloeschl, G. (2017). Validation of SMAP soil moisture over a complex agricultural catchment in Austria. In *EGU General Assembly Conference Abstracts* (p. 14665).

2. Pfeil, I., Hahn, S., Bauer-Marschallinger, B., Hochstöger, S., Vreugdenhil, M., & Wagner, W. (2017): Sentinel-1 Surface Soil Moisture: Comparison against an optimized Metop ASCAT soil moisture product and in-situ data in Lower Austria. Published in *Satellite Soil Moisture Validation & Application Workshop and the CCI Soil Moisture User Workshop.*

3. Pfeil, I., Vreugdenhil, M., Forkel, M., Dorigo, W., & Wagner, W. (2019). Tracking the Leaf Emergence in Deciduous Broadleaf Trees Using Microwave Remote Sensing. In *EGU General Assembly Conference Abstracts* (p. 8021).

4. Pfeil, I., Vreugdenhil, M., Dostalova, A., Wagner, W., Forkel, M., & Dorigo, W. (2019): Detection of spring leaf-out in deciduous broadleaf trees with ASCAT and Sentinel-1. *ESA Living Planet Symposium.*

5. Pfeil, I., Wagner, W., Vreugdenhil, M., Forkel, M., & Dorigo, W. (2020). C-band microwave sensors reflect the spring water uptake of temperate deciduous broadleaf trees. In *EGU General Assembly Conference Abstracts* (p. 9955).

6. Pfeil, I., Wagner, W., Hahn, S., Quast, R., Steele-Dunne, S., & Vreugdenhil, M. (2021). Soil moisture and vegetation effects on the ASCAT backscatter-incidence angle dependence. In *EGU General Assembly Conference Abstracts* (pp. EGU21-10806).

7. Greimeister-Pfeil, I., Wagner, W., Quast, R., Hahn, S., Steele-Dunne, S., & Vreugdenhil, M.: Disentangling soil moisture and vegetation effects on the AS-CAT backscatter-incidence angle relationship, *EGU General Assembly 2022*, Vienna, Austria, 23–27 May 2022, EGU22-5128, https://doi.org/10.5194/egusphere-egu22-5128, 2022.

1.5 Other research contributions

During the pursuit of my PhD I contributed to the following studies which have been published in peer review journals and conference proceedings, but are not directly related to the focus of my PhD and thus not included in this thesis.

First-author conference contributions

1. Pfeil, I. M., Hochstöger, S., Amarnath, G., Pani, P., Enenkel, M., & Wagner, W. (2017). Predicting Vegetation Condition from ASCAT Soil Water Index over Southwest India. In *EGU General Assembly Conference Abstracts* (p. 14216).

2. Pfeil, I., Vreugdenhil, M., Silasari, R., Oismüller, M., Strauss, P., Wagner, W., & Blöschl, G. (2018). ASCAT soil moisture validation with in situ data: comparing the suitability of permanent and temporary sensors. In *EGU General Assembly Conference Abstracts*.

3. Pfeil, I., Wagner, W., Dorigo, W., & Vreugdenhil, M. (2018). Satellite surface soil moisture trends in Austria. 8th *GEWEX Open Science Conference: Extremes and Water on the Edge*.

4. Pfeil, I., Reuß, F., Vreugdenhil, M., Navacchi, C., & Wagner, W. (2020). Classification of Wheat and Barley Fields Using Sentinel-1 Backscatter. In *IGARSS 2020-2020 IEEE International Geoscience and Remote Sensing Symposium* (pp. 140-143). IEEE.

5. Pfeil, I., Vreugdenhil, M., Camici, S., Brocca, L., Preimesberger, W., Crocetti, L., Reuß, F., Enenkel, M., Bavandi, A., Dorigo, W., & Wagner, W. (2020): Tracking Rainfall Deficits Along the Water Cycle Using Multiple EO-based Datasets Over Africa. *ESA Earth Observation for Water Cycle Science*.

6. Greimeister-Pfeil, I., Vreugdenhil, M., Preimesberger, W., Brocca, L., Camici, S., Enenkel, M., Bavandi, A., & Wagner, W. (2022): Tracking rainfall deficits through the water cycle using earth observation datasets: A case study in Senegal. In *IGARSS 2022 IEEE International Geoscience and Remote Sensing Symposium*. IEEE.

Co-authored research articles

1. Enenkel, M., Reimer, C., Dorigo, W., Wagner, W., Pfeil, I., Parinussa, R., & De Jeu, R. (2016). Combining satellite observations to develop a global soil moisture product for near-real-time applications. Hydrology and Earth System Sciences, 20(10), 4191-4208.

2. Vreugdenhil, M., Wagner, W., Bauer-Marschallinger, B., Pfeil, I., Teubner, I., Rüdiger, C., & Strauss, P. (2018). Sensitivity of Sentinel-1 backscatter to vegetation dynamics: An Austrian case study. Remote Sensing, 10(9), 1396.

3. Vreugdenhil, M., Navacchi, C., Bauer-Marschallinger, B., Hahn, S., Steele-Dunne, S., Pfeil, I., ... & Wagner, W. (2020). Sentinel-1 cross ratio and vegetation optical depth: A comparison over Europe. Remote Sensing, 12(20), 3404.

4. Xaver, A., Zappa, L., Rab, G., Pfeil, I., Vreugdenhil, M., Hemment, D., & Dorigo, W. A. (2020). Evaluating the suitability of the consumer low-cost Parrot Flower Power soil moisture sensor for scientific environmental applications. Geoscientific Instrumentation, Methods and Data Systems, 9(1), 117-139.

5. Colliander, A., Reichle, R. H., Crow, W. T., Cosh, M. H., Chen, F., Chan, S., ... & Yueh, S. H. (2021). Validation of soil moisture data products from the NASA SMAP mission. IEEE Journal of Selected Topics in Applied Earth Observations and Remote Sensing, 15, 364-392.

6. Dorigo, W., Himmelbauer, I., Aberer, D., Schremmer, L., Petrakovic, I., Zappa, L., Greimeister-Pfeil, I., ... & Sabia, R. (2021). The International Soil Moisture Network: serving Earth system science for over a decade. Hydrology and earth system sciences, 25(11), 5749-5804.

7. Kubáň, M., Parajka, J., Tong, R., Pfeil, I., Vreugdenhil, M., Sleziak, P., ... & Hlavčová, K. (2021). Incorporating Advanced Scatterometer Surface and Root Zone Soil Moisture Products into the Calibration of a Conceptual Semi-Distributed Hydrological Model. Water, 13(23), 3366.

8. Reuß, F., Greimeister-Pfeil, I., Vreugdenhil, M., & Wagner, W. (2021). Comparison of Long Short-Term Memory Networks and Random Forest for Sentinel-1 Time Series Based Large Scale Crop Classification. Remote Sensing, 13(24), 5000.

9. Tong, R., Parajka, J., Salentinig, A., Pfeil, I., Komma, J., Széles, B., ... & Blöschl, G. (2021). The value of ASCAT soil moisture and MODIS snow cover data for calibrating a conceptual hydrologic model. Hydrology and Earth System Sciences, 25(3), 1389-1410.

10. Tong, R., Parajka, J., Széles, B., Pfeil, I., Vreugdenhil, M., Komma, J., ... & Blöschl, G. (2021). The value of satellite soil moisture and snow cover data for the transfer of hydrological model parameters to ungauged sites. Hydrology and Earth System Sciences Discussions, 1-27.

11. Wagner, W., Lindorfer, R., Melzer, T., Hahn, S., Bauer-Marschallinger, B., Morrison, K., ..., Greimeister-Pfeil, I., & Vreugdenhil, M. (2022). Widespread occurrence of anomalous C-band backscatter signals in arid environments caused by subsurface scattering. Remote Sensing of Environment, 276, 113025.

12. Dostálová, A., Navacchi, C., Greimeister-Pfeil, I., Small, D., & Wagner, W. (2022). The effects of radiometric terrain flattening on SAR-based forest mapping and classification, Remote Sensing Letters, 13:9, 855-864.

1.6 Outline

The next three chapters each comprise one of the research articles that originated in the framework of this doctoral thesis. In each study, the motivation and research objective, the applied methods, as well as the results and conclusions are presented and discussed in detail. Chapter 5 provides a summary of the overall findings of the thesis, implications for the research field, as well as an outlook on remaining and new open questions.

2

Improving the Seasonal Representation of ASCAT Soil Moisture and Vegetation Dynamics in a Temperate Climate

> *You can't write a script in your mind and then force yourself to follow it. You have to let yourself be.*
>
> — **Chimamanda Ngozi Adichie**
> (Nigerian writer)

Abstract Previous validation studies have demonstrated the accuracy of the Metop-A ASCAT soil moisture (SM) product, although over- and underestimation during different seasons of the year suggest a need for improving the retrieval algorithm. In this study, we analyzed whether adapting the vegetation characterization based on global parameters to regional conditions improves the seasonal representation of SM and vegetation optical depth (τ). SM and τ are retrieved from ASCAT using both a seasonal (mean climatological) and a dynamic vegetation characterization that allows for year-to-year changes. The retrieved SM and τ are compared with

in situ and satellite SM, and with vegetation products (SMAP, AMSR2, and SPOT-VGT/PROBA-V). The study region is set in an agricultural area of Lower Austria that is characterized by heterogeneous land cover and topography, and features an experimental catchment equipped with a SM network (HOAL SoilNet). We found that a stronger vegetation correction within the SM retrieval improves the SM product considerably (increase of the Spearman correlation coefficient r_s by 0.15 on average, and r_s comparable to SMAP and AMSR2). The vegetation product derived with a dynamic vegetation characterization compares well to the reference datasets and reflects vegetation dynamics such as start and peak of season and harvest. Although some vegetation effects cannot be corrected by the adapted vegetation characterization, our results demonstrate the benefits of a parameterization optimized for regional conditions in this temperate climate zone.

2.1 Introduction

Soil moisture (SM) plays an important role in the water and carbon cycle and needs to be considered in a number of related applications. SM datasets are used in hydrological model calibration and runoff predictions (Wanders et al., 2014b; Wanders et al., 2014a; Brocca et al., 2010), irrigation scheduling (Ling, 2004; Soulis et al., 2015), rainfall estimation (Koster et al., 2004; Brocca et al., 2015), drought monitoring (Svoboda et al., 2002; Hao et al., 2014; Martínez-Fernández et al., 2016), modeling of groundwater depletion (Rodell et al., 2009), and vegetation and crop growth monitoring (Wagner et al., 2013), amongst many others. These applications require accurate and readily available datasets on different scales.

Over the past 30 years, remote sensing missions have emerged that observe global SM conditions from space (Wagner et al., 2012). The Soil Moisture Ocean Salinity (SMOS) (Kerr et al., 2001) and Soil Moisture Active Passive (SMAP) (Entekhabi et al., 2010) missions are dedicated SM missions operating in L-band, providing global passive SM observations. Another sensor that can be used for the retrieval of global SM, though not designed for this purpose, is the Advanced Microwave Scanning Radiometer 2 (AMSR2), a passive multi-frequency instrument on board GCOM-W1 (Parinussa et al., 2015). An active C-band sensor suitable for SM retrieval is the Advanced Scatterometer (ASCAT) on board the Metop satellites.

At the Vienna University of Technology (TU Wien), a change detection algorithm has been developed to retrieve SM from the scatterometers on board the European remote sensing satellites (ERS) (Wagner et al., 1999b), which was later adapted and

improved for ASCAT (Naeimi et al., 2009b). Many studies have evaluated the ASCAT SM product over different regions. High correlations between ASCAT and in situ data have been observed in the Bibeschbach catchment in Luxembourg (Matgen et al., 2012), in southwestern France (Albergel et al., 2009) and for selected networks across Europe (Brocca et al., 2011). However, weaknesses in the representation of the seasonal cycle in ASCAT SM have been described: Wagner et al. (2014) observed ASCAT SM values in the summer months that are consistently higher than SM values from SMOS and in situ stations in two watersheds in the United States. Three possible reasons were discussed which can lead to high SM in these catchments: Under very dry conditions, sub-surface scattering can increase the backscatter, and consequently the derived SM (Gruhier et al., 2010; Wagner et al., 2013). On the other hand, wet soil surfaces and wetlands can also lead to enhanced backscatter. A third possible reason is a too weak vegetation correction. Barbu et al. (2014) found that, over France, temporal correlations between the satellite data and modeled SM increase by 0.07–0.09 when applying a seasonal correction to the SM values instead of a bias correction that is static throughout the year. This is due to low ASCAT SM values in May, which are adjusted by the seasonal correction.

The TU Wien SM model uses the multi-angle viewing capacity of the ASCAT sensor to correct for vegetation (Hahn et al., 2017). It has been shown that the vegetation characterization can be converted into vegetation optical depth (τ_a) (Vreugdenhil et al., 2016), which is an indicator of the vegetation water content, both the leaf and woody components of the total above-ground biomass (Liu et al., 2011). Similar to SM, vegetation is an important variable in the water and carbon cycle. It has been shown that τ from microwave remote sensing is suitable for continuously monitoring vegetation dynamics (Liu et al., 2011; Tian et al., 2016), and complements datasets from optical satellites such as the normalized difference vegetation index (NDVI) and leaf area index (LAI) (Liu et al., 2011).

The aim of this study was to improve both the ASCAT SM and τ retrievals by optimizing model parameters linked to the vegetation characterization. The representation of the seasonal cycle in the ASCAT SM and τ datasets is assessed against SM and τ from different satellite and in situ datasets. Since the seasonal bias was observed in temperate climate regions, a region in Lower Austria was chosen as a representative area for this analysis. Since 2013, an in situ SM network is operated in an agricultural catchment in this area. Section 2.2 gives an overview of the study area, followed by a description of datasets in Section 2.3. The applied methods are described in Section 2.4. Section 2.5 describes the results of the study for SM and τ, which are discussed in Section 2.6.
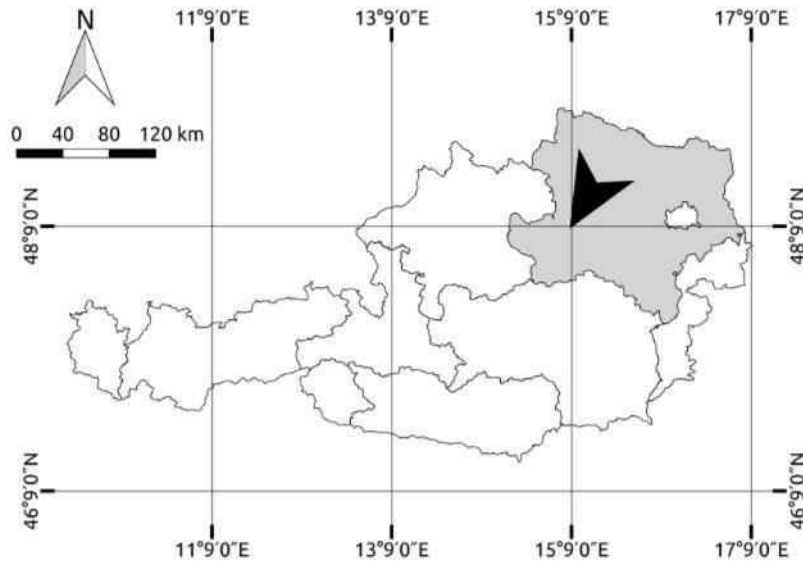
Fig. 2.1: Location of the Hydrological Open Air Laboratory (HOAL) in Lower Austria.

2.2 Study site

The study site is situated in Petzenkirchen, Lower Austria (Figure 2.1). A Hydrological Open Air Laboratory (HOAL) is operated in an agricultural catchment, providing extensive field data used for investigating catchment evapotranspiration, runoff processes, sediment transport, nutrient dynamics, contaminant pathways and spatial patterns in SM (Blöschl et al., 2016). The area is characterized by a humid climate with higher precipitation in summer than in winter. From 1990 to 2014, a mean annual temperature of 9.5 °C and a mean annual rainfall of 823 mm year^{-1} have been observed. Eighty-seven percent of the total area of the HOAL is arable land; the remaining parts are forests (6%), pasture (5%) and paved areas (2%). Two main crop growing seasons are found in the HOAL: winter crops such as wheat, barley and rapeseed are usually planted in autumn and harvested in July. Summer crops (in the HOAL mainly corn) are usually planted in April and harvested in September/October. Between the harvest and seeding of the main crops, green fertilizers are often planted on the fields. Depending on the weather, seeding and harvest dates can vary by a few weeks from year to year. The HOAL catchment is classified as "Cropland, rainfed" by the ESA CCI land cover dataset (Bontemps et al., 2013), but it also features evergreen and deciduous forests and grasslands.

Figure 2.2 (left) shows the area that is (approximately) covered by the ASCAT, AMSR2 and SMAP 3-dB footprints. This area is considerably larger than the catchment, but has similar topographic conditions and land cover as the HOAL. The ESA

Tab. 2.1: Study area characteristics.

	HOAL	Sensor Footprints
Location (center)	48°9′N 15°9′E	approx. 48°9′N 15°9′E
Extent	66 ha	490–1800 km²
Elevation	268–323 m a.s.l.	200–900 m a.s.l.
Mean slope	8%	8.5%
Arable land	87%	approx. 60%
SM stations	31	
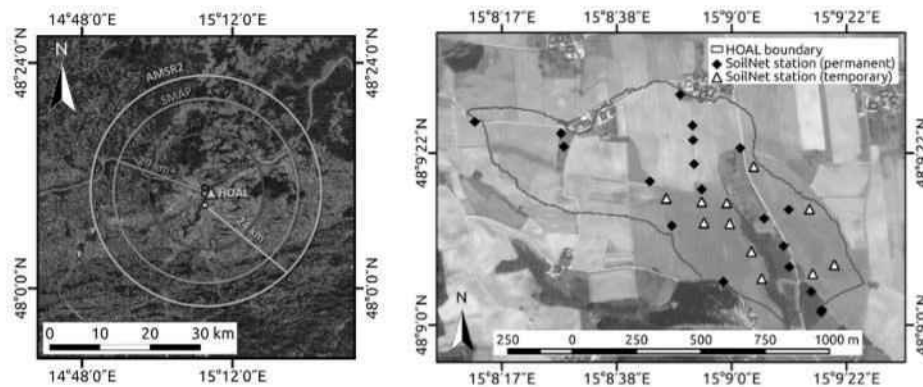
Fig. 2.2: Schematic overview of the 3-dB sensor footprints of ASCAT, SMAP and AMSR2 (**left**); and distribution of permanent and temporary stations in the HOAL catchment (**right**). Map data ©2018 Google.

CCI land cover dataset for the ASCAT, SMAP and AMSR2 footprints is shown in Figure 2.3. The dominant land cover classes found in the study area are rainfed cropland, evergreen needle leaf and deciduous broad leaf forest as well as grasslands. More details about the study area are listed in Table 2.1.

2.3 Datasets

2.3.1 In Situ Soil Moisture

Since 2013, an in situ SM network has been operated in the Hydrological Open Air Laboratory (HOAL), which measures SM at different depths (5, 10, 20, and 50 cm) every 30 min using the Time Domain Transmission (TDT) method. Twenty permanent stations are installed at selected locations that represent the different hydrologic conditions and land cover types present in the catchment. Additionally, 11 stations
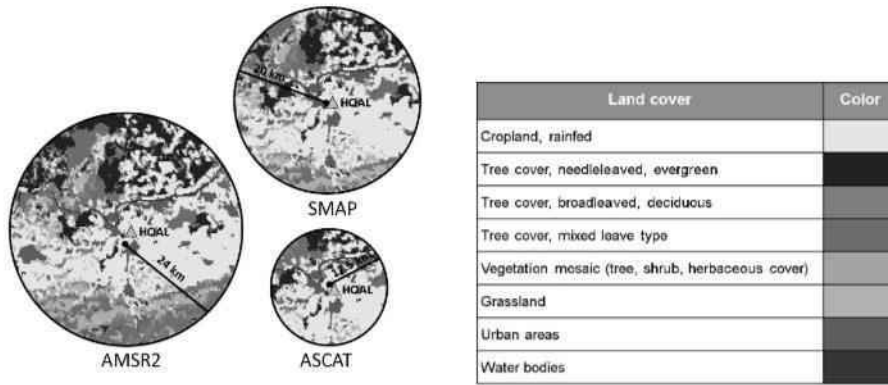
Fig. 2.3: ESA CCI land cover in the 3-dB sensor footprints of ASCAT, SMAP and AMSR2.

are installed temporarily inside agricultural fields, which are removed during farmers' field management practices (planting, harvesting, ploughing, etc.). For this study, the time series of the upper sensors (5 cm) of the in situ stations, averaged over the entire catchment, are used. The network is in the following referred to as HOAL SoilNet. Figure 2.2 (right) shows the distribution of the permanent and temporary SM stations in the catchment.

2.3.2 Satellite Data

ASCAT

Backscatter measurements from the ASCAT sensor on board Metop-A are available since January 2007 and used to retrieve SM and τ_a with the TU Wien model (Wagner et al., 1999b; Naeimi et al., 2009b; Hahn et al., 2017; Vreugdenhil et al., 2016). A schematic overview of the semi-empirical TU Wien modeling scheme is provided in Figure 2.4 (top).

The observed backscattering coefficient σ° is assumed to depend only on the incidence angle (θ), degree of saturation (Θ_s), and vegetation cover (V). Wagner et al. (1999c) found that both a change in Θ_s and in V lead to an increased σ°, and that the effect of V is typically more pronounced at high incidence angles (Figure 2.4, bottom panel). At two incidence angles, seasonal vegetation changes are assumed to not affect the observed σ°; those are the so-called dry and wet cross-over angles (θ_{dry} and θ_{wet}), which were empirically set to 25° and 40° globally (Naeimi et al., 2009b). The incidence angle dependency of σ° is described by a second-order Taylor polynomial in the TU Wien model. The first and second derivatives of the σ°–θ-relationship are referred to as slope (σ') and curvature (σ''). Those can be used to estimate the backscatter at any arbitrary incidence angle (Hahn et al., 2017). In the

TU Wien model

Model parameters	SM	τ

Dependency of σ^o on θ

Seasonal / dynamic vegetation characterization (VC_{seas}, VC_{dyn})

Slope (σ') and curvature (σ'')

Cross-over angles (θ_{dry}, θ_{wet})

Dry and wet reference (σ^o_{dry}, σ^o_{wet})

Water cloud model

Soil moisture

Vegetation optical depth

θ ... incidence angle, σ^o ... backscatter   *(Wagner et al., 1999; Naeimi et al., 2009; Vreugdenhil et al., 2016; Hahn et al., 2017)*

Fig. 2.4: Main steps of the TU Wien algorithm for the retrieval of SM and τ (**top**); and dependency of backscatter (σ^o) on incidence angle θ, soil moisture and vegetation (**bottom**); after Wagner et al., 2013.

TU Wien model, backscatter observations are normalized to a reference incidence angle of 40° to remove the incidence angle dependency (Wagner et al., 1999c); this backscatter time series is termed σ_{40}°.

At θ_{dry} and θ_{wet}, where, as mentioned above, the observed backscatter is assumed to be independent of V, the lowest and highest 10% of backscatter measurements are estimated and averaged to obtain the historically "driest" and "wettest" backscatter values. These two values are then transferred back to the reference incidence angle of 40° using σ' and σ''. Due to σ' and σ'' varying from day to day, time series instead of single values for the driest and wettest backscatter values are obtained. These time series are termed the dry and wet references (σ_{dry}° and σ_{wet}°). They describe the effects of different static and dynamic parameters (e.g., soil roughness, soil texture, and V) on the backscatter observations. Since soil roughness and soil texture are assumed to be static over the retrieval period, dynamics in σ_{dry}° and σ_{wet}° are an indicator of the vegetation state (Wagner et al., 1999a). The difference between σ_{wet}° and σ_{dry}°, also called the sensitivity, determines the dynamic range of the retrieved SM dataset. A small difference leads to a low dynamic range and consequently higher noise in the retrieval (Naeimi et al., 2009b).

In a final step of the TU Wien model, σ_{40}° is scaled between σ_{dry}° and σ_{wet}° to obtain a SM time series that is corrected for the effect of vegetation (see Equation 2.1).

$$\Theta_s = \frac{\sigma_{40}^{\circ} - \sigma_{dry}^{\circ}}{\sigma_{wet}^{\circ} - \sigma_{dry}^{\circ}} \tag{2.1}$$

ASCAT τ (hereafter referred to as τ_a) is derived from σ_{dry}° and σ_{wet}° using a water cloud model (Vreugdenhil et al., 2016). SM and τ_a are retrieved at a spatial resolution of 25 km for every 1–3 days and sampled on a discrete global grid with regular 12.5 km point spacing within the TU Wien model (Wagner et al., 1999b; Naeimi et al., 2009b; Vreugdenhil et al., 2016).

Traditionally, the vegetation state is modeled using seasonal parameters, i.e., one value for each day of the year, and not accounting for year-to-year variations in the vegetation cycle (referred to as seasonal vegetation characterization VC_{seas}). In times of limited backscatter data availability, e.g., the scatterometers on board ERS-1 and ERS-2 (ESCAT), this was necessary to obtain robust estimates of the incidence angle dependency of the observed backscatter. Since the operation of the ASCAT sensor, which has a much higher temporal revisit rate than its predecessor ESCAT, this is no longer necessary. Melzer (2013) introduced a Kernel smoother in order to obtain dynamic parameters not only for each day of the year, but for all years individually.

Chapter 2 Improving the Seasonal Representation of ASCAT Soil Moisture and Vegetation Dynamics in a Temperate Climate

This is referred to as dynamic characterization (VC_{dyn}) in the following. Hahn et al. (2017) showed the robustness of the dynamic characterization globally and Vreugdenhil et al. (2017) showed its sensitivity to inter-annual vegetation dynamics over Australia.

AMSR2

The passive radiometer AMSR2 on-board GCOM-W1 was launched by the Japan Aerospace Exploration Agency (JAXA) in 2012. Similar to its predecessor AMSR-E (Advanced Microwave Scanning Radiometer on the Earth Observing System), it observes brightness temperature at C- and X-band. In this study, SM and τ derived with the Land Parameter Retrieval Model (LPRM) algorithm (version LPRMv05) (Owe et al., 2008a; Parinussa et al., 2015) were selected as reference datasets. To be comparable to the ASCAT datasets, only C-band observations are used in this study. The AMSR2 datasets are provided daily at a spatial resolution of 62 km × 35 km (C-band).

Kim et al. (2015) compared AMSR2 SM derived with the LPRM algorithm to field measurements from COSMOS stations over the USA and found consistent temporal patterns of the two datasets, although AMSR2 tended to overestimate SM (Zreda et al., 2012). Cho et al. (2017) showed AMSR2 to provide a valuable successor to the AMSR-E mission in Australia. More on the validation of the LPRM AMSR2 SM product can be found, e.g., in Kim et al., 2016; Anoop et al., 2017; Yee et al., 2017. To the authors' knowledge, only a brief comparison of the LPRM AMSR2 τ (later referred to as τ_{a2}) to other τ products has been carried out by Cui et al. (2017); τ derived from AMSR-E using the LPRM algorithm has however been evaluated against the widely used NDVI (Liu et al., 2011), applied in agricultural drought monitoring studies (Han et al., 2012) and validated in the Sahel (Tian et al., 2016). Furthermore, it has been applied to the monitoring of global change in the total above ground vegetation water content and biomass over various ecosystems and to the attribution of observed changes to environmental and human drivers (Liu et al., 2013).

SMAP

The SMAP L-band radiometer measures brightness temperature with a revisit time of 1–3 days globally at a spatial resolution of approximately 40 km (Entekhabi et al., 2010). The SM product is derived by inverting a τ-ω-model (Schmugge et al., 1974;

Shutko, 1986; Njoku et al., 1996). Here, the SMAP L3 passive product, version V004, has been selected for a comparison with ASCAT datasets, which is available from 2015 onward. Since SMAP operates in L-band, it is assumed to penetrate deeper into the vegetation than higher frequency bands, and is less affected by radio frequency interference (RFI) (Konings et al., 2017).

A validation of the SMAP SM products was carried out by Colliander et al. (2017), who found that, over 18 core validation sites, the passive product meets the target unbiased root mean square error of 0.04 m^3/m^3 volumetric SM. A comprehensive assessment of the performance of the passive SM product can be found in Chan et al., 2016. The SMAP V004 product includes estimates of vegetation water content (VWC), which is a combined estimate from NDVI (canopy water content) and past field observations and LAI (stem water content) (Chan et al., 2013). For the comparison with τ from ASCAT and AMSR2, SMAP vegetation opacity (VO; later referred to as τ_s) is used, which is equivalent to the VWC product multiplied by a constant scaling factor. To the authors' best knowledge, the τ_s product has so far only been evaluated by Cui et al. (2017); however, an alternate approach for the retrieval of τ from SMAP observations using the multi-temporal dual channel algorithm has been applied and evaluated by Konings et al. (2017).

SPOT-VGT and PROBA-V

SPOT-VGT (1999–May 2014) and its successor PROBA-V (June 2014–ongoing) are global vegetation monitoring missions operating in the optical domain (Dierckx et al., 2014). In this study, leaf area index (LAI) from the satellites is included as a reference for the evaluation of τ_a. The CCI land cover dataset (Bontemps et al., 2013) is used to classify the SPOT-VGT/PROBA-V pixels and to obtain LAI time series for croplands, forests and grasslands.

2.3.3 Pre-Processing

In situ measurements from 20 permanent and 11 temporary sensors installed at 5 cm depth are averaged to a mean in situ SM time series. Frozen conditions and surface snow are masked using average Layer 1 soil temperature (0.00–0.10 m), average surface temperature and snow water equivalent data from the global land data assimilation system (GLDAS; version 2.1) (Rodell et al., 2004). The same masking is applied to the satellite datasets. The soil penetration depth of active C-band systems such as ASCAT ranges from 0.5 and 2 cm under normal, not too

dry conditions; passive systems observe the brightness temperature emissions which originate from the top 0–2 cm (e.g., C-band sensor AMSR2) to 3–5 cm of the soil (e.g., L-band sensor SMAP) (Bartalis et al., 2007; Naeimi et al., 2009b; Entekhabi et al., 2010). To make the satellite and in situ datasets comparable, a soil water index (SWI) (Albergel et al., 2008) with a small time scale parameter (T value of two days) is applied to all satellite SM time series. Thus, the satellite SM values better comply with the measurement depths of the HOAL SoilNet stations (5 cm).

2.4 Methods

Over- or underestimation of SM during spring or summer are likely to be caused by an insufficient correction of vegetation effects on the backscattered signal. The vegetation correction applied in the TU Wien SM retrieval algorithm depends on two components: the choice of cross-over angles and the use of a seasonal or dynamic vegetation characterization. Similar to the vegetation correction needed for the retrieval of SM, τ_a is derived from the dry and wet references. Thus, an improvement of the vegetation characterization should lead to an improvement of both the SM and τ_a datasets. Figure 2.5 shows σ°_{dry} and σ°_{wet} for two selected pairs of incidence angles (10°/30° and 25°/40°) and both VC_{seas} (top) and VC_{dyn} (middle). Metop-A ASCAT backscatter is displayed after its normalization to an incidence angle of 40° (σ°_{40}). To enable a comparison of the time series with meteorological data, air temperature and rainfall and snowfall rates from GLDAS are displayed (bottom).

2.4.1 Type of Vegetation Characterization

Originally, and in the latest released ASCAT SM product (H111), yearly climatologies are used for correction, i.e., every day of the year undergoes the same correction each year (seasonal vegetation correction, VC_{seas}; Figure 2.5a). The approach presented by Melzer (2013), Vreugdenhil et al. (2016) and Hahn et al. (2017) included inter-annual variations in the vegetation dynamics (VC_{dyn}; Figure 2.5b). In this study, the effect of applying VC_{dyn} instead of VC_{seas} was analyzed.

(a) Seasonal vegetation characterization.

(b) Dynamic vegetation characterization.

(c) GLDAS meteorological data.
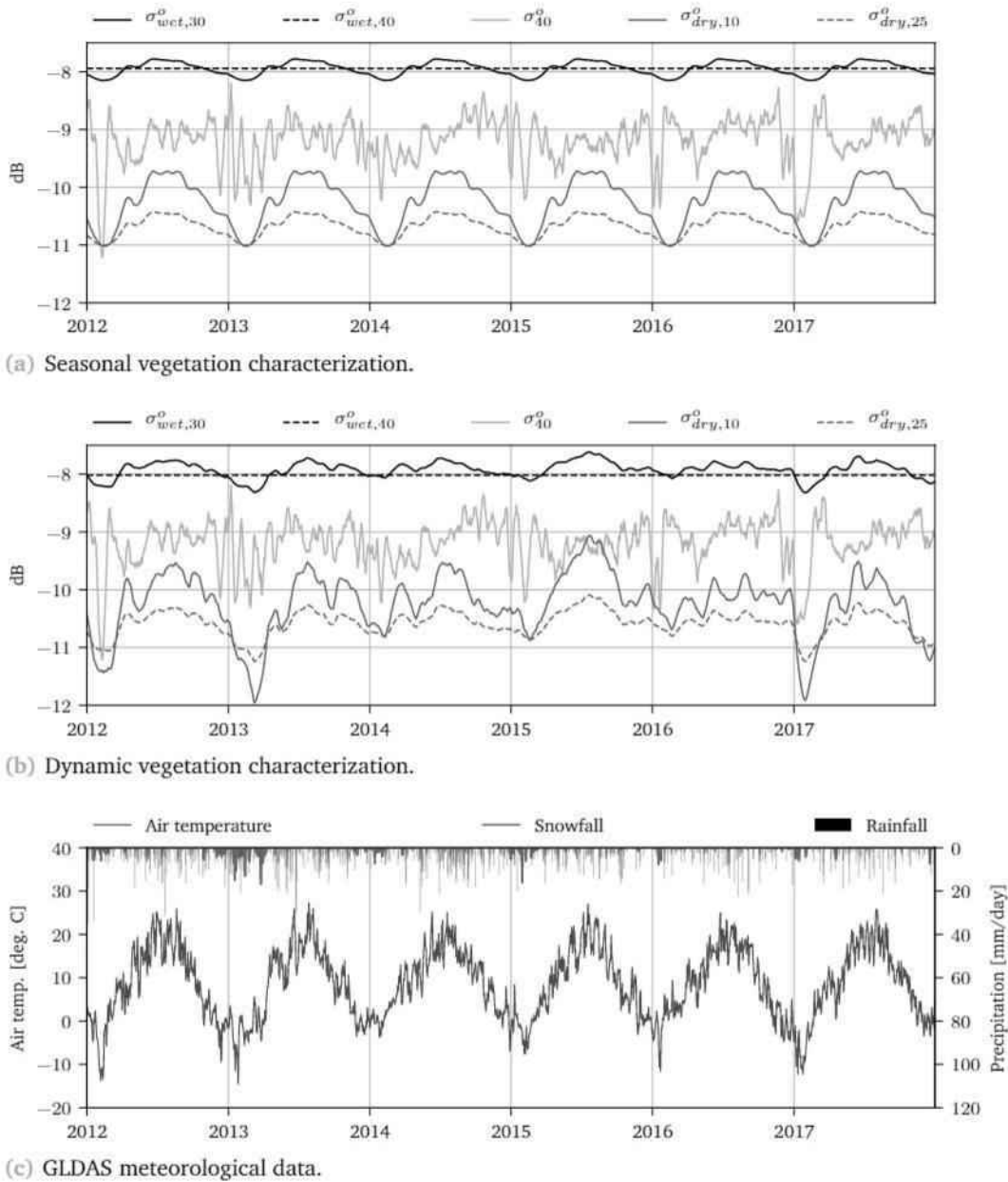
Fig. 2.5: Dry and wet reference derived from Metop-A ASCAT using two different pairs of cross-over angles (10°/30° and 25°/40°) and seasonal (a) and dynamic vegetation characterization (b). Additionally, the backscatter normalized to an incidence angle of 40° (σ_{40}^o) is displayed. (c) GLDAS air temperature, rainfall rate and snowfall rate for the study region.

2.4.2 Selection of Cross-Over Angles

Due to the transferring of the driest and wettest observed values from θ_{dry} and θ_{wet} back to the reference incidence angle of 40°, the amplitude of the vegetation characterization is determined by the choice of the dry and wet cross-over angles; lower cross-over angles lead to a larger amplitude of the vegetation characterization, i.e., the model assumes a stronger effect of vegetation (Figure 2.5). In the following, this is referred to as a stronger vegetation characterization. Wagner (1998) found that the cross-over angle of dry surfaces is lower than for wet surfaces. Globally, the cross-over angles are set to the empirically determined values of 25° (dry soil) and 40° (wet soil; compare Figure 2.4, bottom) (Naeimi et al., 2009b). To optimize the retrieval to regional conditions, the effect of modifying the cross-over angles was analyzed in this study.

2.4.3 Evaluation of the Results

The effect of changing the cross-over angles and selecting VC_{seas} or VC_{dyn} was analyzed for both SM (Section 2.5.1) and τ (Section 2.5.2). For SM, HOAL in situ data were used as a reference, as well as SM from AMSR2 and SMAP. ASCAT τ (τ_a) was compared to τ from AMSR2 (τ_{a2}) and SMAP (τ_s) as well as to LAI retrieved from SPOT-VGT/PROBA-V observations.

For SM, the evaluation was based on the Spearman and Pearson correlation coefficients (r_s and r_p) as well as on the unbiased root-mean-square deviation ($ubRMSD$). In the case of τ, the focus is given to the visual interpretation of the time series, since high r values are mainly associated with smooth τ curves that approximate the mean yearly cycle, but do not necessarily contain interesting features coming from different crop types (see Section 2.5.2). As a reference for the visual interpretation, photos of the HOAL catchment, information on the crop types, planting and harvesting dates as well as meteorological data (see Figure 2.5c) were used.

Although the analyzed spatial scales are considerably different (local in situ network vs. sensor footprints of multiple km^2), we consider the HOAL catchment appropriate for the comparison with satellite data due to the similar land cover types and topographic conditions described in Section 2.2.

(a) Seasonal vegetation characterization.   (b) Dynamic vegetation characterization.
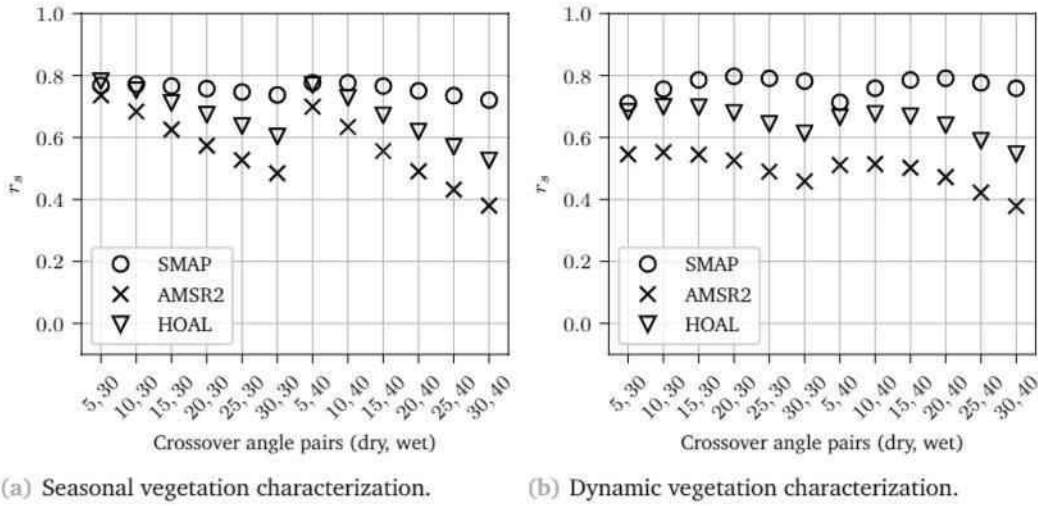
Fig. 2.6: Spearman correlation coefficient (r_s) between different retrievals of ASCAT SM and SMAP (circles), AMSR2 (crosses) and HOAL in situ SM (triangles) for 2012–2017. ASCAT SM was retrieved using: (a) VC_{seas}; and (b) VC_{dyn}.

2.5 Results

2.5.1 Soil Moisture

In the following, retrievals of ASCAT SM using different settings for the above described parameters are compared to satellite and in situ SM.

Cross-Over Angle Optimization

Figure 2.6 shows r_s between different versions of ASCAT SM and the reference datasets. r_s was calculated for the available period of the respective datasets: 2015–2017 for SMAP, 2012–2017 for AMSR2, and 2013–2017 for the in situ data from the HOAL catchment. For all datasets and for both VC_{seas} and VC_{dyn}, higher correlation coefficients (up to 0.8) are obtained with a stronger vegetation correction, i.e., lower cross-over angles than the original pair of 25°/40°. Only when comparing with SMAP, r_s increases with increasing cross-over angles when correlating it with dynamically corrected ASCAT SM (Figure 2.6b). All correlations are highly significant ($p <$ 0.01).

The sensitivity to SM was determined by the selection of cross-over angles. In general, lower cross-over angles ($\theta_{dry} = 5°$–$15°$, $\theta_{wet} = 30°$) lead to a lower dynamic range between σ°_{dry} and σ°_{wet}, because it is expected that vegetation has a stronger effect

on the overall backscatter intensity. However, this leads to a higher noise in the SM retrieval, because the dynamic range of σ°_{dry} and σ°_{wet} defines how sensitive the (remaining) backscatter signal is to changes in soil moisture. Furthermore, low cross-over angles can create more backscatter outliers ($\sigma^{\circ}_{40} < \sigma^{\circ}_{dry}$ and $\sigma^{\circ}_{40} > \sigma^{\circ}_{wet}$), which are typically corrected to 0% ($-25\% > $ SM $ < 0\%$) and 100% ($100\% > $ SM $ < 125\%$). However, extreme outliers (i.e., SM $< -25\%$ or SM $> 125\%$) are marked as invalid SM estimates and therefore set to NaN. Due to these characteristics of the algorithm, the cross-over angle pair of 10° and 30° is considered the optimal choice for the study region, although other cross-over angle pairs lead to higher correlation coefficients (Figure 2.6). In the following, all results are shown for the original and optimized cross-over angles pairs of 25°/40° and 10°/30°.

Quantitative Comparison

As stated by Wagner et al. (2013), validation results of different types of datasets should also be interpreted in a relative context, for example by comparing different satellite datasets with the same in situ dataset. Therefore, r_s and r_p as well as the $ubRMSD$ were calculated between each of the satellite datasets and the HOAL SoilNet time series (Figure 2.7). For each satellite–in situ pair, the time period for which both datasets are available was used; the time periods are limited by the availability of HOAL SoilNet data (from August 2013 onward) and SMAP data (from April 2015 onward). SMAP and AMSR2 show r_s and r_p of 0.77 and 0.78 (SMAP) and 0.71 and 0.69 (AMSR2) with the in situ data. For the respective periods, ASCAT and in situ SM show correlations ranging from 0.57 to 0.75, with higher correlation coefficients clearly associated with a stronger vegetation correction (lower cross-over angles). The $ubRMSD$ between SMAP and AMSR2 and the in situ data is 0.034 and 0.038, and ranges from 0.036 to 0.048 for the different ASCAT datasets. Using cross-over angles of 10° and 30° leads to ASCAT datasets that have a smaller $ubRMSD$ and that are more similar to SMAP and AMSR2. Figure 2.7 also shows that the usage of VC_{seas} or VC_{dyn} has a smaller effect on the metrics than the choice of cross-over angle pair. These results show that in the current SM product, the cross-over angles are not optimal and the applied vegetation correction thus not ideal for the study area.

In a next step, r_s has been calculated between the in situ and satellite datasets for different seasons (spring: March–June; summer: July–September; and autumn and winter: October–February). Figure 2.8 shows r_s and the change obtained from using different cross-over angle pairs. In the spring months, r_s between ASCAT and HOAL increases by 0.16 (VC_{seas}) and 0.12 (VC_{dyn}) when using lower cross-over
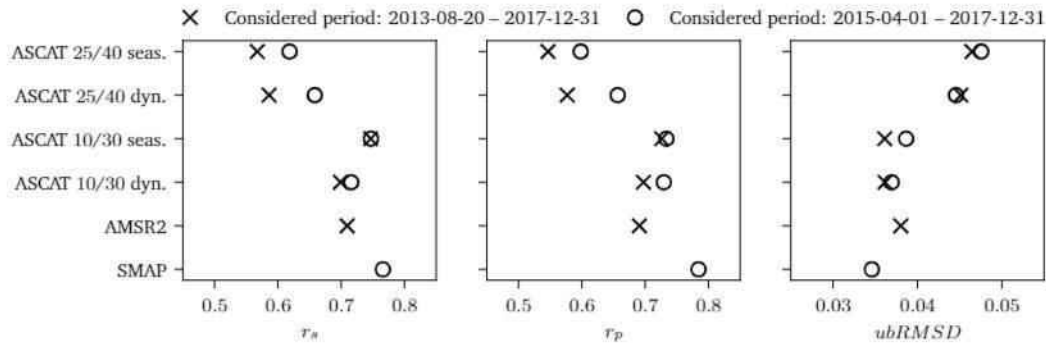
Fig. 2.7: Spearman and Pearson correlation coefficients (r_s and r_p) and $ubRMSD$ between HOAL in situ SM and different satellite SM datasets. The metrics have been calculated for 20 August 2013 (limited by availability of HOAL SoilNet data) and 1 April 2015 (limited by availability of SMAP data) until the end of 2017.

angles, i.e., a stronger vegetation correction. In summer, only little (VC_{seas}) or even negative changes (VC_{dyn}) are achieved; in autumn, both a stronger VC_{seas} and VC_{dyn} improve ASCAT with respect to the HOAL SoilNet (+0.18 and +0.09, respectively). Over the entire period, the change of r_s is positive (+0.15 on average) when applying a stronger vegetation correction, and the HOAL–ASCAT r_s becomes comparable to the HOAL–AMSR2 and HOAL–SMAP r_s. Whether the correlation improves or deteriorates in different seasons probably depends on several reasons. r_s has been calculated over up to six years, all of which experienced different weather conditions. When looking at individual years, larger improvements are made in 2015 and 2017 (rather dry years) than in 2014 and 2016 (rather wet); in 2014 and 2016, r_s also increases, but is significantly higher when using VC_{seas} (not shown). Such differences between the years are also observed in the τ_a time series (see Section 2.5.2). A possible reason could be different temperature and rainfall conditions, leading to differences in the vegetation growth that are not sufficiently represented by the vegetation correction.

Qualitative Comparison

Finally, we examined the time series obtained from different model parameters (Figure 2.9; a moving mean with a 14-day window has been applied on all datasets for better readability). In this figure, it can be seen that, in all years, a stronger vegetation correction for the SM retrieval (blue solid line) leads to a seasonal representation of SM in spring and summer that is closer to the reference datasets, compared to the original SM product (dotted black line). However, not the entire effect is corrected this way; ASCAT SM is still—in some years (e.g., 2014)
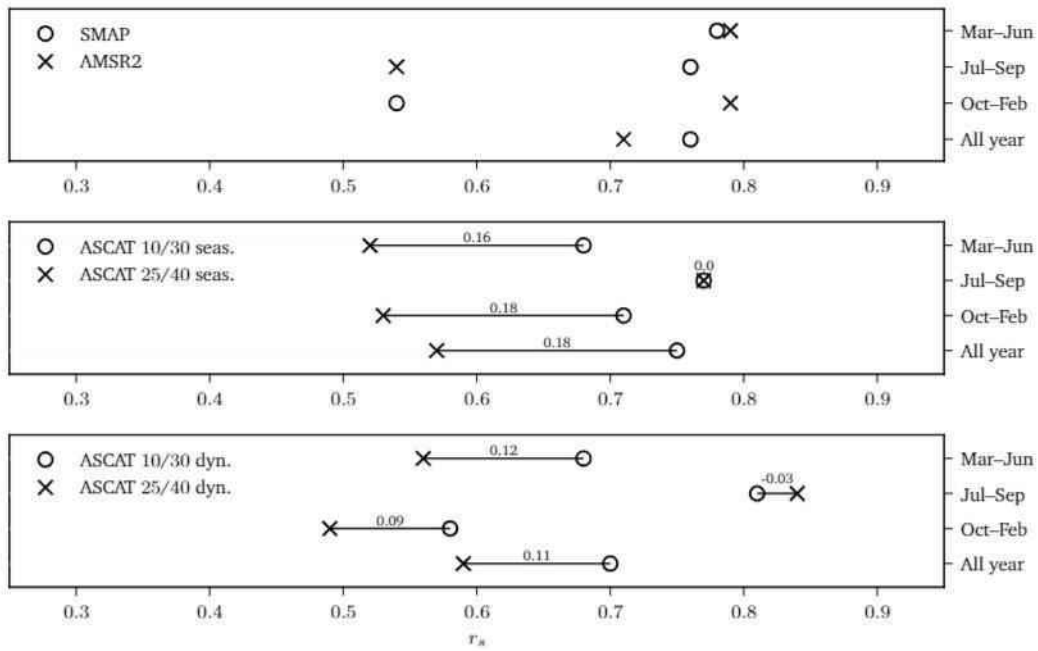
Fig. 2.8: Spearman correlation coefficient (r_s) between HOAL in situ SM and different satellite SM datasets for different seasons.

considerably—lower in spring than the other datasets. This will be further discussed in Section 2.6.

Apart from the mostly positive effect on the seasonal representation, we observe a negative side effect that can occur in years with high vegetation activity. In the study area, 2015 was a very warm and dry year. When choosing VC_{dyn} and cross-over angles of 10° and 30°, the effect of the vegetation correction may be so strong during summer that no SM can be retrieved anymore, leading to a data gap (see Figure 2.9b, solid black line in July–August 2015; also visible in Figure 2.5b).

Another issue to be considered are the penetration depths of the C- and L-band sensors (upper few centimeters of the soil), compared to the installation depth of the in situ sensors (5 cm, i.e., deeper than satellite sensors penetrate under normal, not extremely dry conditions). Although this discrepancy is reduced by the application of the SWI with a T value of two days, there can still be effects such as a faster drying out of the soil that is only seen by satellites but not measured by the deeper in situ sensors. Consequently, lower SM values observed by satellite sensors do not necessarily mean erroneous retrievals, but can simply be caused by different reference depths.

2.5.2 Vegetation Optical Depth (τ)

To evaluate the performance of τ_a in the study area, it is compared to τ_s and τ_{a2}, and LAI from SPOT-VGT/PROVA-V, resampled to the ASCAT footprint.

Quantitative Comparison

In a first step, linear regressions of LAI and satellite τ datasets have been calculated (Figure 2.10). The steeper slopes (0.04–0.05) observed with τ_{a2} and τ_s (right column) are in line with the findings of Lawrence et al. (2014), who observed a slope of 0.05 between MODIS LAI and τ from SMOS. The slope of τ_a and LAI is smaller, whereas larger slopes (0.02) for τ_a are obtained when applying a VC_{seas} (left column). Using a VC_{dyn} (middle column) leads to smaller slopes and more outliers, especially when applying a stronger vegetation characterization. A r_s of 0.79 and 0.75 is observed for τ time series with small amplitudes and no inter-annual variation (τ_s, and τ_a derived with a VC_{seas}). If inter-annual variations are included in a product, r_s decreases significantly to values ranging from 0.29 to 0.55 (τ from AMSR2 and τ_a derived with a VC_{dyn}), but corresponds to correlation values found by Jones et al. (2011) between MODIS LAI and τ from AMSR-E in temperate climates. R^2 and r_s suggest that VC_{dyn} does not add value, but deteriorates the τ_a product. However, effects caused by sensitivities to different vegetation characteristics of optical and microwave sensors, which lead to time lags and varying dynamics between the time series (Liu et al., 2011; Jones et al., 2013), are neglected or wrongly reflected by r_s. Therefore, a qualitative analysis of τ and LAI is given in the following.

Qualitative Comparison

Figure 2.11 shows the different datasets for 2012–2017. In the left column, τ_a is shown as yearly climatologies, i.e., no inter-annual variations (Vreugdenhil et al., 2016); the right column shows τ_a calculated as described by Melzer (2013) and Vreugdenhil et al. (2017) (VC_{dyn}). The τ_a time series retrieved with original (25°/40°) and modified (10°/30°) cross-over angles are displayed as dashed and solid lines, respectively. As can be seen in Figure 2.11, a change to lower cross-over angles leads to a larger range of values, i.e., a stronger vegetation signal. The value range of all τ and LAI time series is relatively similar over all years, but some inter-annual dynamics are visible, e.g., a variable number of main peaks and different timings of those peaks (Figure 2.11). This supports the implementation of dynamic parameters
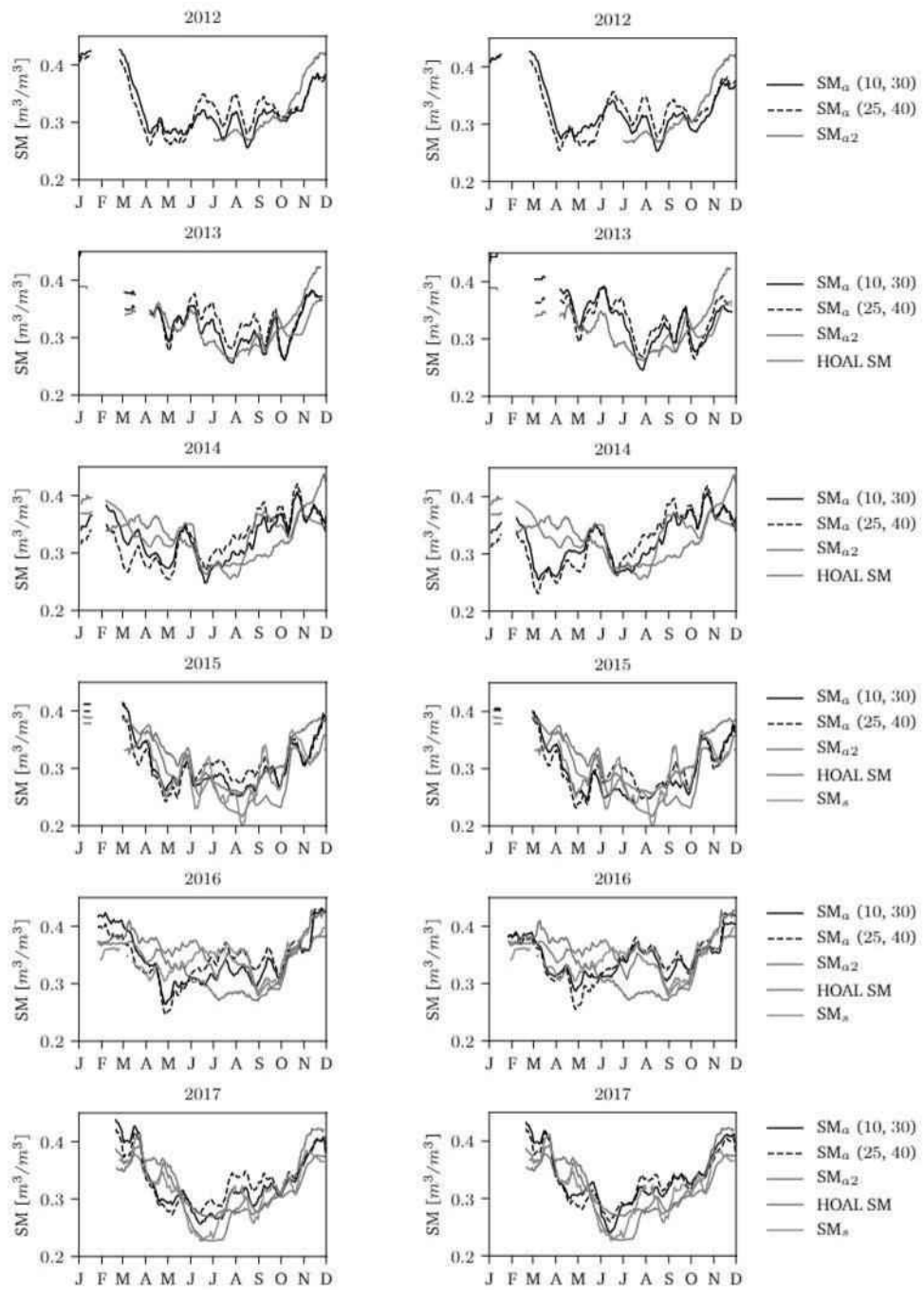
(a) Seasonal vegetation characterization. (b) Dynamic vegetation characterization.

Fig. 2.9: SM from ASCAT (SM_a), AMSR2 (SM_{a2}), SMAP (SM_s) and the in situ network (HOAL SM) for the years 2012 to 2017; SM_a retrieved using: (a) VC_{seas}; and (b) VC_{dyn}. A moving mean (window: 14 days) has been applied to all datasets for better readability.

for the retrieval of τ_a in the study area. The τ_a time series shows significant inter-annual differences, which are likely to reflect different weather conditions. In the study area, 2015 was a warm and dry year, thus encouraging early vegetation growth and leading to a high peak in τ_a. In contrast, 2016 was rather wet, with light and heavy rainfalls the whole year. This is reflected by a relatively flat τ_a time series with some distinct ups and downs throughout the year.

For an interpretation of signal dynamics between years and during each growing season, we examine the reference datasets. Two main peaks occur around June and September in τ_s, which does not include inter-annual variations, and in τ_{a2} in every year. Those two peaks coincide with the peak of season in winter crops (first peak) and summer crops (second peak) and their harvest shortly after. The LAI dataset also shows these two peaks, however not as pronounced in every year. In most of the years, the rise in spring occurs later, but increases more quickly than the microwave datasets. Recurring features can also be identified in the τ_a time series: each year, τ_a starts to rise in February, shows one peak in April/May, one peak around June/July and one peak in August/September, and then drops again in autumn. The two peaks in June/July and August/September coincide with those visible in the reference datasets, however slightly shifted in time compared to LAI. This is likely due to the sensitivity of the different variables to different vegetation characteristics; since LAI is more sensitive to the green canopy, it observes peaks earlier than τ, which is more sensitive to the water content in the vegetation, including the woody parts of the canopy (Jones et al., 2011; Jones et al., 2012; Vreugdenhil et al., 2017). To test this for the datasets used in this study, correlations were calculated between the datasets after introducing negative and positive temporal shifts of 0–12 weeks. Figure 2.12 shows the results of the analysis, which confirm that highest r_s values are obtained when applying a positive temporal shift of two weeks (τ_s) and 6–8 weeks (τ_a, τ_{a2}) to the LAI dataset. The smaller shift between LAI and τ_s can be explained by the fact that τ_s is based on NDVI, which has been found to have a smaller phase shift to LAI than τ in several land cover regions (Jones et al., 2011). Between τ_a and τ_{a2}, r_s is highest with no introduced time shift. Similar results are obtained for τ_s, except when correlating it with τ_a retrieved with cross-over angles 10° and 30° and using VC_{seas}. However, all r_s values obtained between those two time series with positive temporal shifts of 0–6 weeks lie within a range of 0.10, and the maximum r_s value is not as distinct as in other dataset combinations.
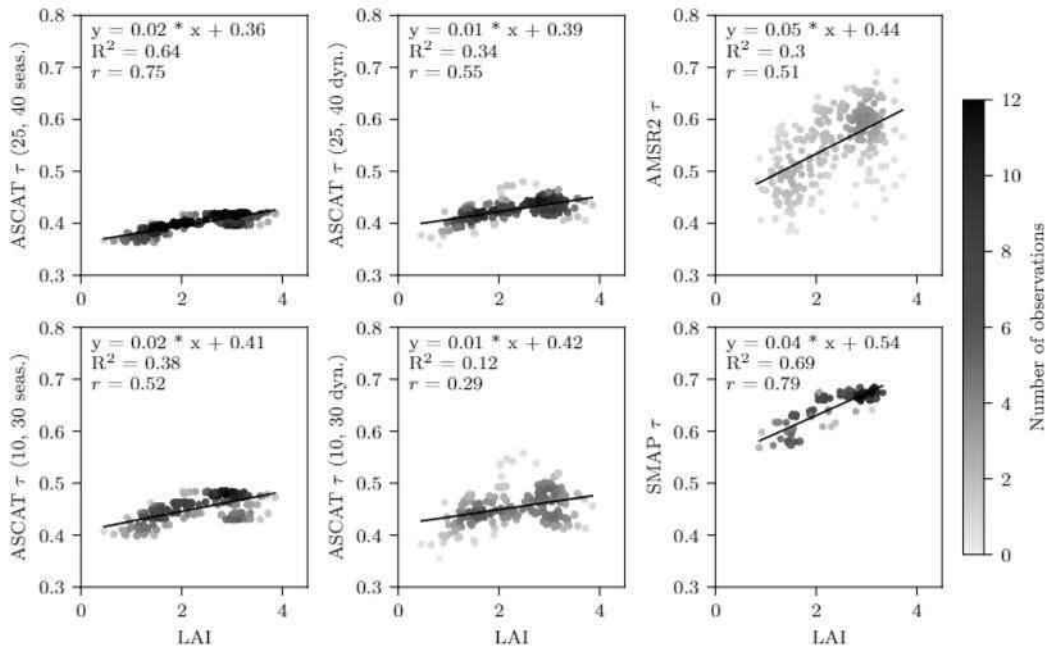
Fig. 2.10: Satellite τ as a function of SPOT-VGT/PROBA-V LAI; the color indicates the number of observations. The black line shows the linear regression. In each panel, the function of the linear regression, the coefficient of determination (R^2) and r_s are given.

Land Cover Effect

Land cover in the study region is mostly cropland, but it also features grasslands and forests (mostly evergreen and mixed evergreen/deciduous). Figure 2.13 shows the LAI time series of up to three selected only-forest (MF, DF, EF), only-cropland (C) and only-grassland (G) areas, as well as the τ_a time series of the 25 km ASCAT footprint over the study region. The three selected cropland LAI time series (Figure 2.13, bottom left) show different peaks due to the planted crop type (winter crops vs. summer crops). As can be seen in the figure, dynamics in LAI and τ_a correlate well, and, as expected, features from all selected land cover types can be found in the τ_a time series of the study area. Differences in the absolute values of τ_a between the years might be caused by different temperature and rainfall conditions.

Every year, a peak is visible in the τ_a signal around April/May (Figure 2.11, right column). This peak is not present in LAI (Figures 2.11 and 2.13) and cannot be explained by a particular change in vegetation water content or biomass. To investigate a possible effect of remained snow or wet snow, we looked at photos taken in the HOAL catchment and analyzed meteorological data from GLDAS (air temperature, rainfall and snowfall). However, the GLDAS snowfall rate was zero in most years (see Figure 2.5c) and no snow was detected on the photos during the

periods of interest. Snow can thus most likely be excluded as a reason for the visible peak in spring. A likely interpretation of the peak could be changes in the scattering behavior of the vegetation or bare surface due to structural changes during this period. The size of the peak varies over the years; in 2014, it is very high and wide, whereas, one year later, it is hardly present. The origin of those peaks and their amplitudes are still under investigation. Because we also see inconsistencies in spring in SM, this issue will be addressed in section 2.6.

2.6 Discussion

This study analyzed the effect of a regionally optimized parameterization of vegetation in the TU Wien algorithm for both the SM and τ_a products derived from Metop-A ASCAT backscatter. The analysis of SM shows that, in the study area, a stronger vegetation correction than the globally optimal parameter is needed. Correlations with reference datasets increase, and seasonal differences such as an underestimation of SM in spring and an overestimation in summer are mitigated; however, they are not fully corrected. The application of VC_{seas} or VC_{dyn} does not affect the SM dataset as much as the choice of the cross-over angles.

To transfer these findings to other regions in temperate climates and test if the problems described in Section 2.1 are mitigated by the application of a stronger vegetation correction, correlations and the $ubRMSD$ between ASCAT and in situ SM have been calculated for the Little River watershed (Georgia, United States; (Wagner et al., 2014)), an area in southwest France (Barbu et al., 2014) and a catchment in western Denmark (hydrological observatory HOBE; (Jensen et al., 2011; Bircher et al., 2012)). At all sites, r_p and r_s increase from 0.64 to 0.71 on average when applying a stronger vegetation correction; the average $ubRMSD$ decreases from 0.031 to 0.028. Table 2.2 shows the metrics for every location. The metrics have been calculated for the period 2012–2017 (LR and southwest France) and 2012–2015 (HOBE), and periods with negative temperatures or snowfall have been masked out, as described in Section 2.3.3.

When analyzing the τ_a time series, the added value of a dynamic vegetation parameterization becomes obvious. Inter-annual differences due to different weather conditions are visible, and vegetation dynamics such as start and peak of season and harvest of different crop types are reflected in the signal. As for SM, discrepancies between ASCAT and the reference datasets are observed in spring. This discrepancy in spring, where the effect of vegetation is over- and SM underestimated, is currently
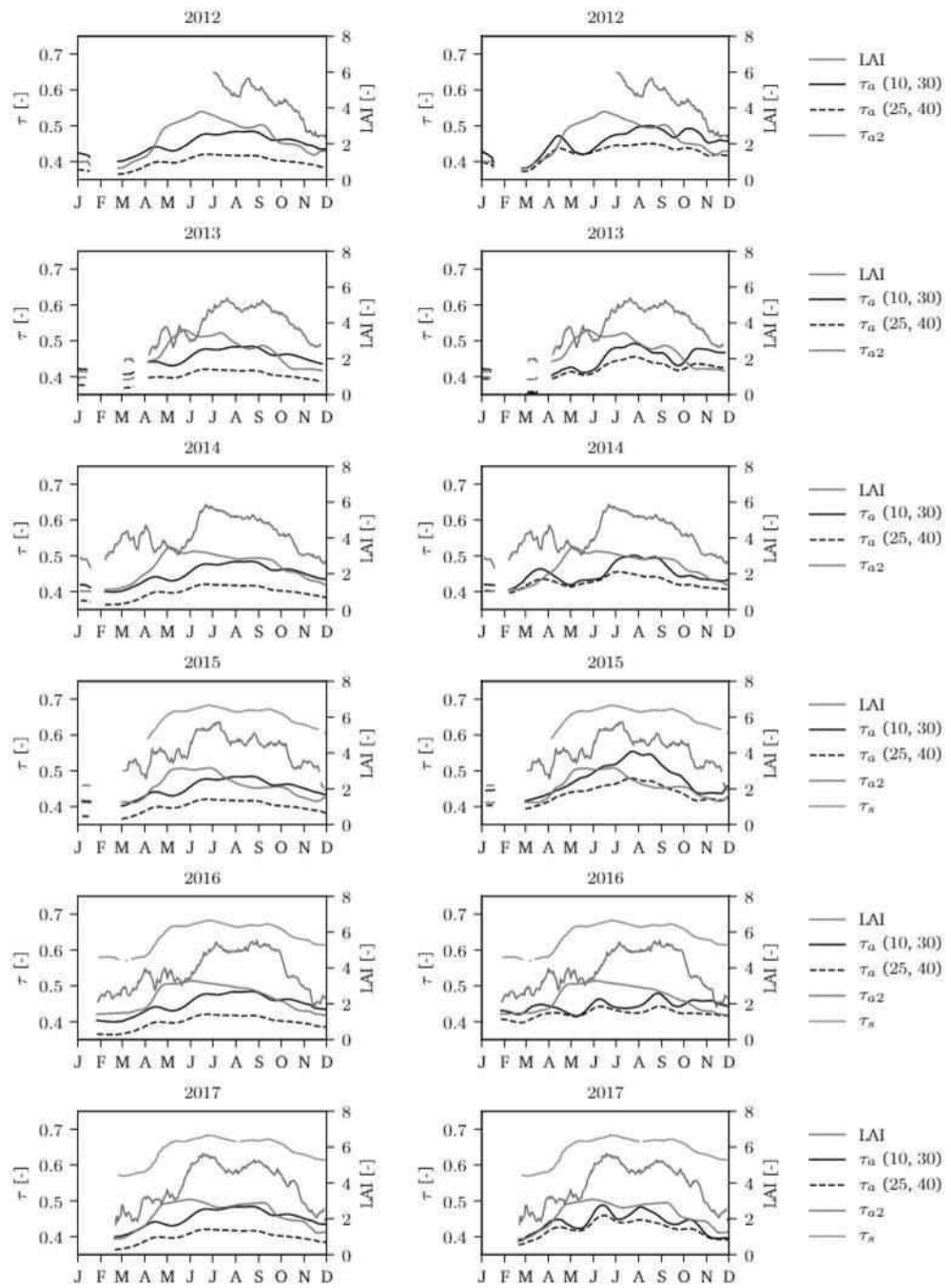
(a) Seasonal vegetation characterization. (b) Dynamic vegetation characterization.

Fig. 2.11: τ and LAI for the years 2012 to 2017; τ_a retrieved using: (a) VC_{seas}; and (b) VC_{dyn}.
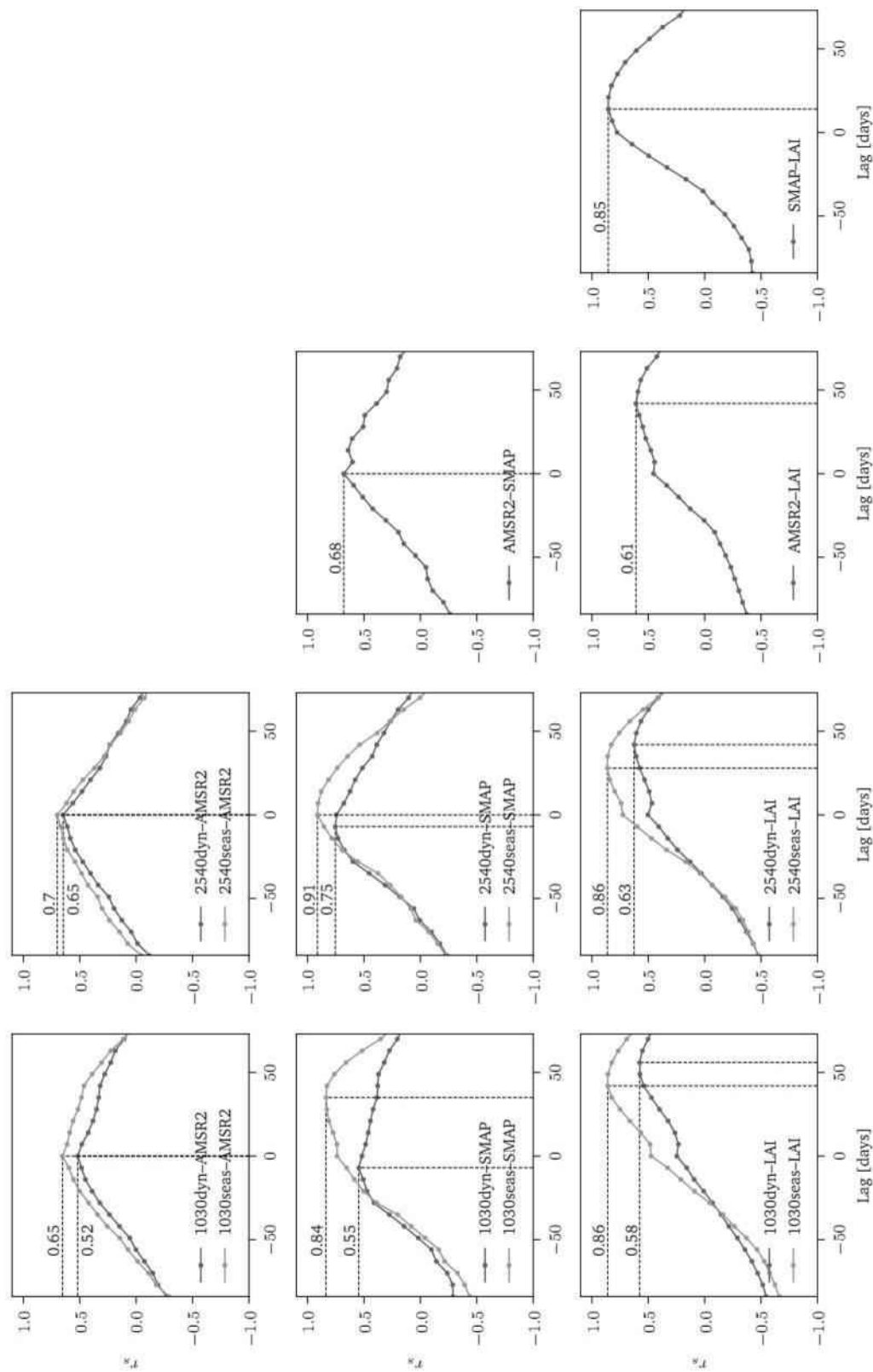
Fig. 2.12: r_s obtained between the indicated time series after applying negative/positive temporal shifts of up to twelve weeks to the latter one.

Chapter 2   Improving the Seasonal Representation of ASCAT Soil Moisture and Vegetation Dynamics in a Temperate Climate
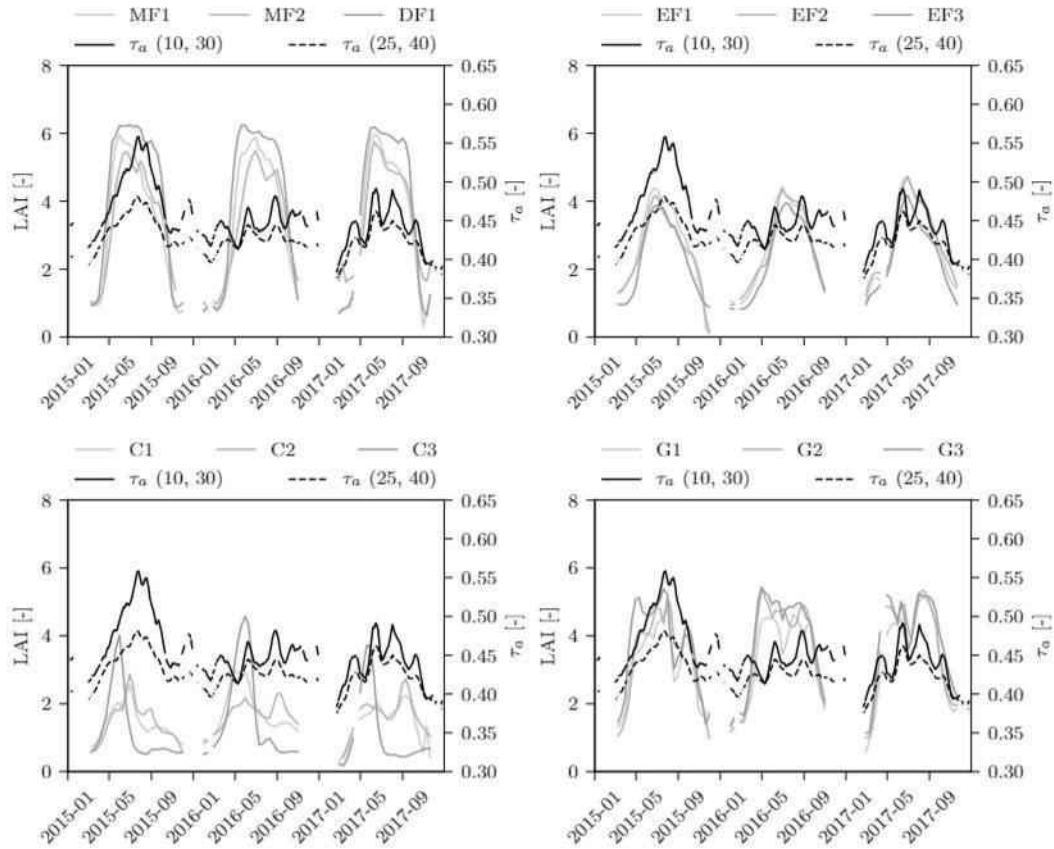
Fig. 2.13: LAI from: (**top left**) mixed and deciduous forest (MF, DF); (**top right**) evergreen coniferous forest (EF); (**bottom left**) croplands (C); and (**bottom right**) grasslands (G); and τ_a from the study region (all panels). Frozen periods are masked out.

Tab. 2.2: Metrics between different ASCAT SM versions and three in situ SM datasets.

Catchment	ASCAT Version	r_p	r_s	$ubRMSD$
LR	25/40, VC_{seas}	0.60	0.58	0.031
LR	10/30, VC_{seas}	0.68	0.68	0.025
LR	25/40, VC_{dyn}	0.61	0.59	0.030
LR	10/30, VC_{dyn}	0.64	0.63	0.026
SW France	25/40, VC_{seas}	0.62	0.64	0.035
SW France	10/30, VC_{seas}	0.67	0.69	0.033
SW France	25/40, VC_{dyn}	0.64	0.67	0.034
SW France	10/30, VC_{dyn}	0.70	0.72	0.032
HOBE	25/40, VC_{seas}	0.68	0.71	0.029
HOBE	10/30, VC_{seas}	0.77	0.79	0.026
HOBE	25/40, VC_{dyn}	0.70	0.72	0.028
HOBE	10/30, VC_{dyn}	0.79	0.78	0.025
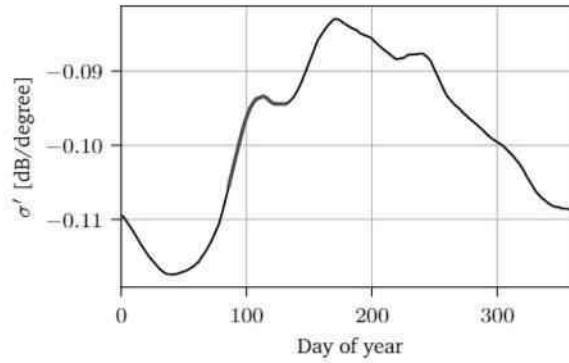
Fig. 2.14: Average annual behavior of the slope of the $\sigma°$–θ relationship. The peak in spring is highlighted in red.

being investigated. In the course of the SM retrieval, the dependency of $\sigma°$ on the incidence angle θ is modeled as a second-order Taylor polynomial (see Section 2.3.2). The first component, i.e., the slope of the $\sigma°$–θ curve (σ'), decreases (in absolute values) with vegetation growth, since volume scattering from the vegetation increases $\sigma°$ at larger incidence angles (Figure 2.4, bottom). Figure 2.14 shows the time series of σ'. In addition to the main seasonal cycle of vegetation growth, we also see a peak in spring (Day of Year 85–130). This means that, during that time, the backscattered component is less dependent on the incidence angle. Behavior such as this is commonly associated with vegetation growth, but can in this case also be due to changes in the structure of the vegetation (e.g., crops growth changes from grass-like to vertical), or due to SM-induced alteration of σ'. Structural differences would induce a change in the single scattering albedo (ω), i.e., in the scattering and absorption behavior of the vegetation layer. At the moment, ω is considered to be static over time in the TU Wien retrieval algorithm. The same assumption is made in the retrieval algorithm of τ_{a2}, where we also see peaks in April. Assuming that ω shows a seasonal cycle and the effect of considering this cycle in the ASCAT SM and τ_a retrieval should be explored in further research.

2.7 Conclusions

We analyzed the retrieval of surface soil moisture (SM) and vegetation optical depth (τ) from Metop-A ASCAT over a region in Lower Austria. Both SM and τ have been retrieved from ASCAT backscatter values using a seasonal and a dynamic vegetation characterization, which takes into account year-to-year changes. Furthermore, the effect of adjusting parameters related to the strength of the vegetation characteriza-

tion has been analyzed. We found that changing the empirically identified cross-over angles used for the global SM retrieval according to regional conditions improves the SM retrieval considerably (increase of r_s by 0.15 on average, and r_s and $ubRMSD$ comparable to SMAP and AMSR2). The vegetation product derived with a dynamic vegetation characterization compares well to τ observed by AMSR2 and SMAP, and LAI from SPOT-VGT/PROBA-V. Vegetation dynamics such as start and peak of season and harvest are reflected in the signal, however partially shifted in time, which reflects the different sensitivities of LAI and τ. The results highlight the benefits of a parameterization optimized to regional conditions for an area in the temperate climate zone.

Author contributions

I.P. conceived and designed the experiments together with M.V., S.H. and W.W.; I.P. analyzed the data and wrote the paper; and P.S. and G.B. contributed their expertise. All authors participated in the revision of the manuscript.

Acknowledgements

Conflict of interest

The authors declare no conflict of interest. The founding sponsors had no role in the design of the study; in the collection, analyses, or interpretation of data; in the writing of the manuscript, and in the decision to publish the results.

Does ASCAT observe the spring reactivation in temperate deciduous broadleaf forests?

3

> *One thing I've learned in the woods is that there is no such thing as random. Everything is steeped in meaning, colored by relationships, one thing with another.*

— **Robin Wall Kimmerer**
(Native American scientist and author)

Abstract Scatterometer observations over land are sensitive to the water content in soil and vegetation, but have been rarely used to study seasonal changes in the plant water status and seasonal development of deciduous trees. Here we use Advanced Scatterometer (ASCAT) observations to investigate the sensitivity of C-band backscatter to spring phenology of temperate deciduous broadleaf forests in Austria. ASCAT's multi-angle looking capability enables the observation of backscatter over a large range of incidence angles. The vegetation status affects the slope of the backscatter-incidence angle relationship. We discovered a maximum in the slope around the month April, hereafter referred to as spring peak, predominantly in regions covered by deciduous broadleaf forest. We hypothesized that the spring

peak indicates the average timing of leaf emergence in the deciduous trees in the sensor footprint. The hypothesis was tested by comparing the timing of the spring peak to leaf unfolding observations from the PEP725 phenology database, to the increase of leaf area index (LAI) during spring, and to temperature. Our results demonstrate a good agreement between the ASCAT spring peaks, phenology observations and temperature conditions. The steepest increase in LAI however lags behind the ASCAT peak by several days to a few weeks, suggesting that the spring peak in fact marks the timing of maximum woody water content, which occurs right before leaf emergence. Based on these observations, we conclude that the ASCAT signal has a high sensitivity to spring reactivation and in particular water uptake of bare deciduous broadleaf trees. Our findings might provide the basis for novel developments to estimate eco-physiological changes of forests during spring at large scales.

3.1 Introduction

The seasonal dynamics of vegetation play a vital role in the Earth system, as they affect the global carbon, energy and water fluxes and their interaction (Bonan, 2008; Richardson et al., 2013). Phenological changes reflect weather and climate variability and hence long-term trends in the forest phenology are a direct indicator of climate change (Menzel et al., 2006). Warming trends in northern temperate and boreal forests show an earlier onset of the growing season, which corresponds to an earlier water uptake in spring and might reduce plant productivity later in the season (Buermann et al., 2018; Wolf et al., 2016). In order to understand the effects of such structural changes in leaf area dynamics on ecosystem carbon and water cycling, large-scale estimates of physiological changes are required.

Remote sensing has been intensively used to monitor phenological changes in vegetation (Xiao et al., 2009; Beurs et al., 2010; Helman, 2018). Changes in land surface phenology have been mainly assessed using optical vegetation indices. Unfortunately, those are hampered by cloud cover or high sun-zenith angles, which makes the estimation of phenological changes difficult (Forkel et al., 2015). As an alternative, observations derived from microwave sensors have the advantage that they are usually free from temporal gaps, as microwaves are capable of penetrating clouds, and observations can also be taken at night (Jones et al., 2011). One disadvantage of real-aperture microwave sensors such as ASCAT is their coarse spatial resolution. This is compensated by the high temporal availability, making these observations especially useful for global-scale analyses.

Microwave remote sensing of vegetation is sensitive to two things in particular: first, to vegetation dynamics as a result of changes in the plant water content, and second, to the physical structure of the vegetation canopy (e.g., leaf size and orientation, diameter and orientation of stems and branches, canopy density) (Jones et al., 2010). Several studies have analyzed vegetation dynamics with observations from active C-band microwave sensors, starting in the 1990s with the scatterometers onboard the European Remote Sensing (ERS) satellites (Wagner et al., 1999a; Wagner et al., 1999c), and, since 2007, using observations from their successor ASCAT (Advanced Scatterometer), by either analyzing the relationship between incidence angle and backscatter (Hahn et al., 2017; Steele-Dunne et al., 2019) or by retrieving vegetation optical depth (Vreugdenhil et al., 2016; Vreugdenhil et al., 2017). Wagner et al., 1999c showed that the backscatter decreases with increasing incidence angle, and that the slope of this relationship is shallower over dense vegetation canopies and steeper over bare soil. This is because vegetation acts as a volume scatterer, and scatters energy diffusely in all directions. Over vegetation, the observed backscatter is thus less dependent on the incidence angle. Steele-Dunne et al. (2019) demonstrated that both slope and curvature of the backscatter-incidence angle relationship varied significantly between different grassland types, and that negative anomalies in slope and curvature can be detected in areas with prolonged conditions of low soil moisture.

A detailed study over a temperate-climate agricultural region in Austria showed that dynamics in the slope in early and late summer largely coincide with the growing cycle of winter and summer crops (Pfeil et al., 2018). However, a period of relatively shallow (negative) slope, hereafter referred to as ASCAT spring peak (SP_{ascat}), which frequently occurs in April, could not be related to the typical crop growing cycle. To see if spring peaks are found in other locations, we examined the slope time series of a large number of grid points in central and eastern Europe. This extension of the study region revealed a correspondence between the occurrence of a spring peak in ASCAT and deciduous broadleaf forest (DBF) cover (Fig. 3.1), a vegetation type which has so far not been investigated using ASCAT observations in specific.

In order to understand how structural changes in DBF in spring affect coarse-scale ASCAT backscatter measurements at multiple incidence angles, one must first take a look at the biological processes in trees. Deciduous broadleaf trees start to prepare for leaf-out in the preceding summer and autumn, when buds are created, which stay closed until the following spring (Rohde et al., 2011; Way, 2011). If trees break dormancy too early, e.g., during a period of warm days in winter, they risk to suffer from potentially fatal damages due to late frosts (Richardson
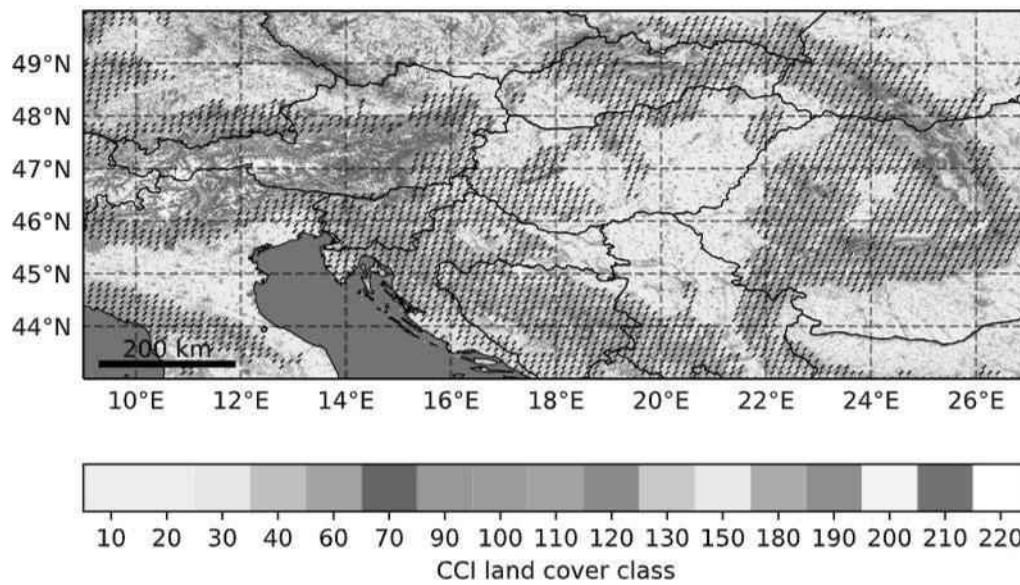
Fig. 3.1: CCI land cover and occurrence of spring peaks (tilted black lines) over central and eastern Europe. 10: cropland; 20: cropland, irrigated or post-flooding; 30: mosaic cropland (>50%)/natural vegetation (<50%); 40: mosaic natural vegetation (>50%)/cropland (<50%); 60: DBF; 70: ENF; 90: mixed forest; 100: mosaic tree and shrub (>50%)/herbaceous cover (<50%); 110: mosaic herbaceous cover (>50%)/tree and shrub (<50%); 120: shrubland; 130: grassland; 150: sparse vegetation; 180: shrub or herbaceous cover, flooded; 190: urban areas; 200: bare areas; 210: water bodies; 220: permanent snow and ice (Bontemps et al., 2012).

et al., 2018). This is prevented by a requirement for enough days below a certain temperature (chilling requirement, Perry, 1971). As soon as the chilling requirement is met and temperatures have risen above a species-dependent threshold (Perry, 1971; Chuine, 2000), the trees start to prepare for bud break. In addition to the temperature requirements, day length plays a role; this effect is however highly species-dependent and still not fully understood (Polgar et al., 2011; Basler et al., 2014). The further development of the buds requires the uptake of water and therein contained nutrients by the trees. The water content in the trees has been found to be highest before bud break and to decrease again with the onset of photosynthesis by the emerging leaves, and thus transpiration (Essiamah et al., 1986; Ewers et al., 2001; Hao et al., 2013; Young-Robertson et al., 2016). This chain of processes is referred to as spring reactivation (Essiamah et al., 1985; Essiamah et al., 1986; Fromm et al., 1986).

A number of studies have demonstrated the sensitivity of C-band sensors to structural changes in DBF (Sinha et al., 2015). The scattering characteristics of DBF and evergreen needleleaf forest (ENF) have for example been used for forest mapping and forest type classification from Sentinel-1 backscatter data by Dostálová et al. (2018). The authors describe in their study that whereas ENF backscatter is lowest in winter and gradually increases towards summer, backscatter from DBF is lowest in summer due to extinction from the leaves. The same was observed in a study over Switzerland by Rüetschi et al. (2018). In the study, the authors compared cross-polarized backscatter from Sentinel-1 over DBF to observations of leaf emergence and found a good correspondence, which was however subject to an uncertainty of ± 12 days due to the usage of 24-daily backscatter composites. Pitts et al. (1987) studied scattering processes in an aspen forest canopy and found that while backscatter as well as extinction increase with leaf emergence, extinction is 2 to 10 times larger than the scattering coefficient, indicating that considerable absorption is occurring within the canopies. Proisy et al. (2000) analyzed the backscatter response from a mixed deciduous forest stand and concluded that it is difficult to relate backscatter variations to seasonal changes of forest parameters such as leaf dimensions and leaf mass per area, partly due to the strong scattering response of branches, which probably mask the beginning and end of the leafy cycle.

These studies only analyzed the total backscatter response normalized to a reference incidence angle, and did not look at the variation of backscatter over different incidence angles, i.e., what is described by the slope parameter. In this study, we investigate the sensitivity of the ASCAT slope to physiological and structural changes in DBF. In particular, we focus on the question if the ASCAT spring peaks mark the date of leaf emergence.

3.2 Study area

We carry out our study over Austria. A large number of phenological observations is available all over the country, which is unfortunately not the case for the other countries shown in Fig. 3.1. Moreover, Austria provides an interesting study area as DBF occurs in a range of climate and elevation zones. The eastern flatlands in Austria are characterized by a temperate climate without dry season and with warm summers in the lowlands (Koeppen-Geiger climate class *Cfb*, Rubel et al., 2017). Here, the land cover is dominated by rainfed croplands and forests (Fig. 3.2, top), and terrain slopes range from 0° to 32° approximately (average slope: 2°). The west is dominated by mountains with alpine grasslands and evergreen needleleaf forests (ENF), and approximate slopes between 0° and 48° (average slope: 13°) (geoland.at, 2020). The climate is fully humid with warm and cool summers (climate classes *Dfb*, *Dfc*) depending on the exact location, and partly classified as polar tundra (*ET*). The country has a large dense DBF region south-west of the city of Vienna, and smaller fractions of DBF across the country (Fig. 3.2, bottom). The Alps make up approximately two thirds of the Austria's area; the other third are lowlands and transition zones. We carried out parts of the analysis for this region of moderately flat terrain, dominated by DBF, MF and croplands. The sub-region is covered by 163 ASCAT grid cells and will be referred to as "moderate flatlands".

3.3 Datasets

3.3.1 ASCAT

The Advanced Scatterometer (ASCAT) is a microwave sensor on-board the Metop satellites. It observes vertically polarized C-band backscatter (f=5.255 GHz) from the Earth surface, and is sensitive to the surface roughness, vegetation structure, soil moisture and vegetation water content. One of ASCAT's key features is its capability to observe a target from different azimuth and incidence angles. This is enabled by three fanbeam antennas on each side of the instrument, which cover an incidence angle range of 34°-65° (fore and aft beam) and 25°-55° (mid beam). The dependency of the backscatter on the incidence angle can be modelled as a second-order Taylor polynomial (Wagner et al., 1999c), and based on this relationship, soil moisture and vegetation optical depth (τ) can be derived (Wagner et al., 1999b; Naeimi et al., 2009b; Hahn et al., 2017; Vreugdenhil et al., 2016). The first and second derivatives of the relationship curve at the reference incidence angle of 40° are
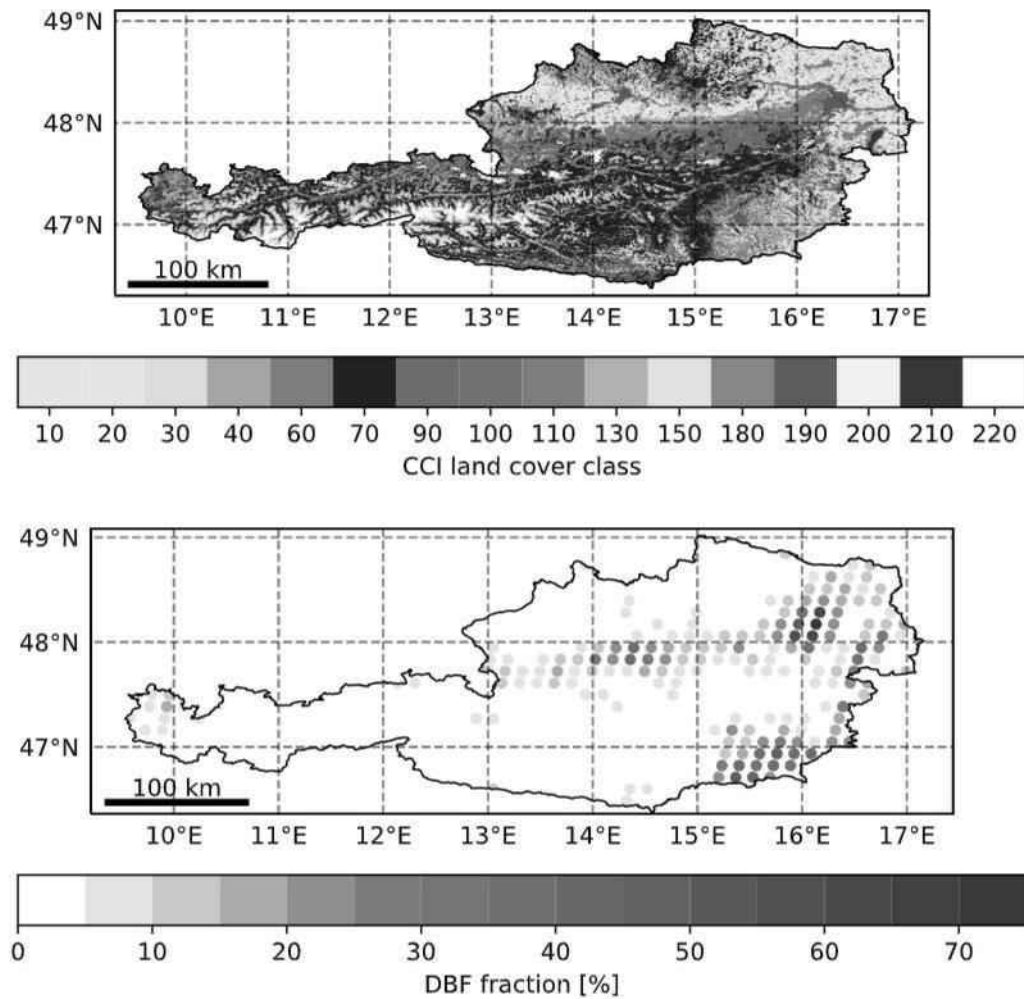
Fig. 3.2: Top: CCI land cover in Austria. 10: cropland; 20: cropland, irrigated or post-flooding; 30: mosaic cropland (>50%)/natural vegetation (<50%); 40: mosaic natural vegetation (>50%)/cropland (<50%); 60: DBF; 70: ENF; 90: mixed forest; 100: mosaic tree and shrub (>50%)/herbaceous cover (<50%); 110: mosaic herbaceous cover (>50%)/tree and shrub (<50%); 130: grassland; 150: sparse vegetation; 180: shrub or herbaceous cover, flooded; 190: urban areas; 200: bare areas; 210: water bodies; 220: permanent snow and ice (Bontemps et al., 2012). Bottom: DBF fraction (derived from CCI land cover) in the ASCAT grid cells.

referred to as slope and curvature. A shallower slope of the backscatter-incidence angle relationship is commonly associated with higher volume scattering caused by the vegetation structure and water content. Hahn et al. (2017) found in a global analysis that the fitting of the slope and curvature parameters is robust, except for sandy deserts. The ASCAT τ time series, which are calculated using the slope, have been shown to reflect vegetation dynamics over Australia (Vreugdenhil et al., 2016) and a heterogeneous agricultural region in Austria (Pfeil et al., 2018).

The ASCAT datasets used in this study are part of the EUMETSAT H SAF Metop ASCAT DR2018 SSM time series 12.5 km sampling (H113) data record (H SAF, 2018). There, the slope is calculated as a climatology (for every day of year (DOY), no interannual variations) from Metop-A ASCAT backscatter observations. A detailed description of the algorithm is provided in the H SAF ATBD, 2018. In addition, we use an experimental Metop ASCAT data record based on new model parameters (Exp-ASCAT-SSM). In Exp-ASCAT-SSM, the slope parameter is calculated over all observations within a 42-day window using a Kernel smoother (Melzer, 2013; Hahn et al., 2017). This way, the slope is available as a time series, i.e., including interannual variations. As the spatial resolution of the ASCAT sensor is in the order of 25 km x 25 km, the observed signal represents the combined backscatter of this coarse grid cell. All ASCAT datasets are available on a discrete global grid (WARP grid), and every grid cell has a unique grid point index (GPI) (see TUW GEO Grid Point Locator, https://www.geo.tuwien.ac.at/dgg/index.php).

An example of the observed backscatter values and the function described by the thereof derived slope and curvature parameters for September 2, 2010, is displayed in Fig. 3.3 (left), for a grid cell dominated by agriculture and a DBF coverage of 12%. Fig. 3.3 (right) shows yearly slope time series and the slope climatology for the same grid cell. The period DOY 80-140, where SP_{ascat} commonly occurs, is highlighted in blue.

3.3.2 PEP725 database

The Pan European Phenological database (PEP725) (Templ et al., 2018) provides open access plant phenology data for a number of European countries, including Austria, and currently contains information on 46 growing stages of 265 plant species. The phenological stage used in this study is BBCH-11, standing for the stage "First leaves unfold" of the Biologische Bundesanstalt, Bundessortenamt and Chemical Industry (BBCH) scale (Finn et al., 2007). We use data from the period 2007 to 2016, which are available for 188 Austrian sites and up to six deciduous
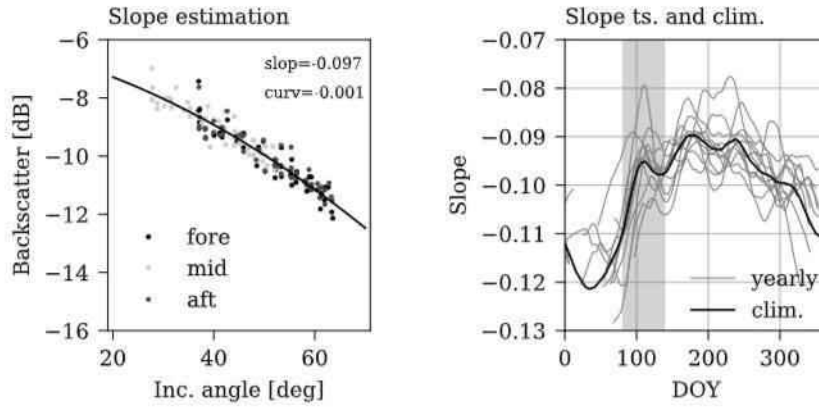
Fig. 3.3: Left: Example of the observed fore-, mid- and aft-beam backscatter within a ±21 day window (around September 2, 2010) and the thereof derived backscatter-incidence angle relationship curve (described by the slope and curvature parameters); right: yearly slope time series and climatology (DOY 80-140 highlighted in blue); both for GPI 2421559 (lon/lat: 15.26 E/48.06 N).

Tab. 3.1: Phenological observations of the listed tree species are used as a reference in this study. The number of available sites and observations for the years 2007 to 2016, in total and in the sub-region of moderate flatlands (MFL), is given.

| Species | | Sites | | Observ. | |
Botanical name	Common name	Total	MFL	Total	MFL
Aesculus hippocastanum	Horse chestnut	117	43	527	185
Betula pendula	Hanging birch	155	63	650	242
Fagus sylvatica	European beech	103	45	431	190
Quercus robur	Common oak	92	36	416	173
Acer pseudoplatanus	Sycamore maple	97	30	443	128
Tilia cordata	Small-leaved lime	92	36	471	181

broadleaf species per site. The tree species and numbers of available sites and observations are listed in Table 3.1.

3.3.3 Leaf area index

LAI data from SPOT/VGT and PROBA-V (Dierckx et al., 2014) are provided by the Copernicus Global Land Service (CGLS). In this study, version 1 of the dataset is used, which is available globally with a spatial resolution of 1 km since 1999. The LAI products are distributed in 30-days composites, and updated every 10 days using a moving window. As recommended in the Product User Manuals (VITO, 2017;

VITO, 2019) we use the "nominal" date for our analysis, i.e., the day where the sum of weights of the weighting function is the same on each side.

During leaf-out, the leaf area changes rapidly, leading to a steep increase in the LAI time series of DBF and a maximum in the first derivative of the time series. Those maxima (LAI'_{max}) serve as a reference for DBF leaf-out in this study. In order to obtain DBF LAI on a spatial resolution comparable to ASCAT, we averaged all 1 km LAI pixels within an ASCAT grid cell that are classified as DBF (CCI Land Cover), and thus resampled the dataset to the ASCAT grid.

3.3.4 SPARTACUS dataset

The SPARTACUS dataset, made available by ZAMG, the Austrian national weather service, provides daily minimum and maximum temperature for Austria on a 1 km grid (Hiebl et al., 2016). We resampled the dataset to the ASCAT grid before using it for the calculation of growing degree days (GDD). More details on the GDD calculation are provided in section 3.4.3.

3.4 Methods

3.4.1 Spring peak detection

We detect spring peaks in the slope time series by searching for relative maxima in the period between DOY 80 and DOY 140. The investigation of the slope time series showed that the spring peaks commonly occur during this period in Austria. The a priori limitation of the period is necessary in order to avoid capturing "false" peaks which can be caused by crops earlier or later in the season. Before the spring peak detection (SPD) is performed, the slope time series are smoothed using a window of 14 days to obtain clear maxima and to remove small short-term variations leading to multiple relative extrema within a period of only a few days. A slope value is defined as a relative maximum if it is greater than the three preceding and the three following values. We first apply the SPD method to the slope climatology to obtain a robust estimation of the spatial distribution of spring peaks. Then, we apply the SPD to the slope time series, resulting in the timing of SP_{ascat} in every year (given in DOY). Fig. 3.4 shows the backscatter-incidence angle relationship curve fitted to the observations over all grid cells in Austria that (top left) show no peak and (top right) show a peak in spring. The curves were spatially averaged over the respective grid

Tab. 3.2: Most frequent land cover types in Austria (resampled to ASCAT grid).

CCI LC class	Number of ASCAT grid cells
Rain fed cropland	154 (28.3% of Austria's area)
DBF	14 (2.6%)
ENF	255 (47.0%)
MF	61 (11.2%)
Grassland	37 (6.8%)
Urban areas	12 (2.2%)

cells and are displayed as 10-daily means. The spring period (DOY 80-140) is shown in green, the summer period (DOY 170-220) in black and all other dates in grey. It can be seen that in summer, i.e., the period of highest vegetation activity, the curve has the shallowest slope due to volume scattering. In spring, the observed slope is steeper in grid cells without SP_{ascat}, whereas it is similar to the summer slope in grid cells with SP_{ascat}. Fig. 3.4 (bottom) shows examples of the slope climatology and two years of the slope time series of GPI 2421559 (12% DBF, 45% cropland) and GPI 2442965 (2% DBF, 91% cropland), along with the detected spring peaks.

3.4.2 ASCAT's sensitivity to deciduous broadleaf forest

To determine the sensitivity of ASCAT to phenology dynamics in DBF, we carry out a land cover analysis. As Austria's land cover is heterogeneous and ASCAT's resolution is coarse, we test the effect of heterogeneity in two ways. First, to identify in which land cover classes peaks are detected, we determine the dominant land cover type per ASCAT grid cell. There are six major land cover types: rain fed cropland, DBF, ENF, mixed forest (MF), grassland, and urban areas. The areas covered by each land cover type are listed in Table 3.2. DBF dominates only 2.6% of all grid cells, but is present in smaller fractions almost everywhere in the country. Thus, secondly, we assess the effect of land cover heterogeneity by calculating the fraction of DBF per ASCAT grid cell. Both dominant land cover and DBF fraction are then used to test the SPD method and to determine if a minimum fraction of DBF is necessary to obtain a reliable peak detection.
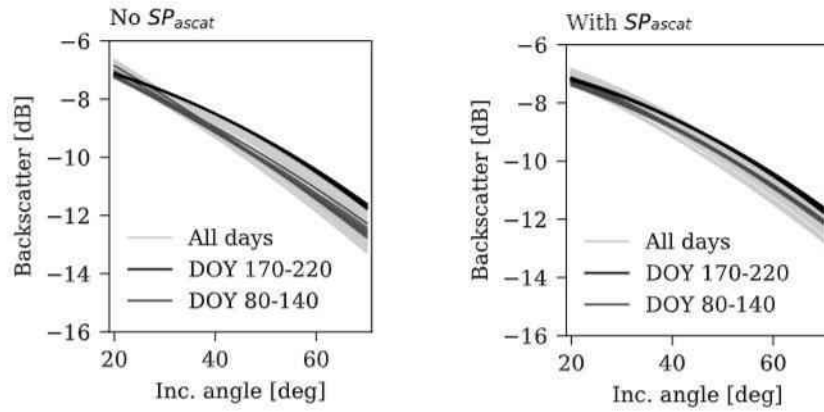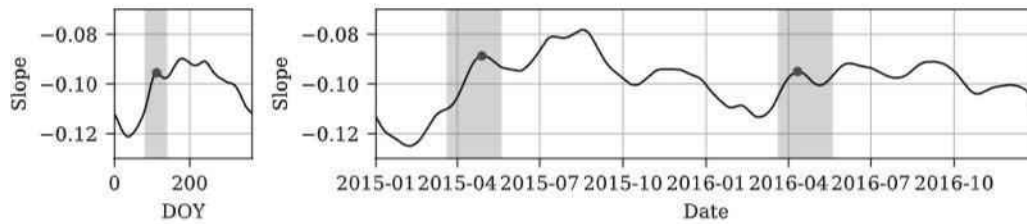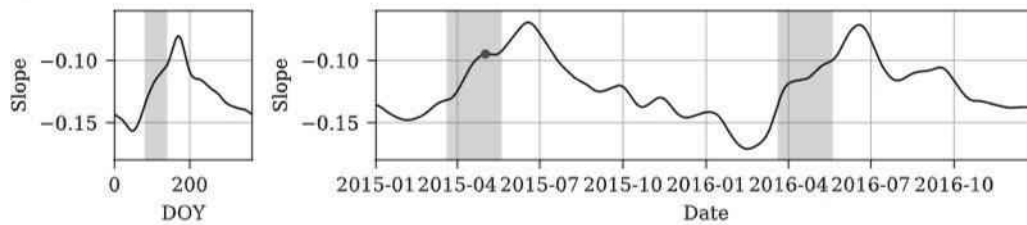
Fig. 3.4: Backscatter-incidence angle relationship curve over grid cells without a spring peak (top left) and with a spring peak (top right). The parameters were spatially averaged for the respective grid cells and are displayed as 10-daily means. Bottom: Slope climatology and time series for GPI 2421559 (12% DBF, 45% cropland) and GPI 2442965 (2% DBF, 91% cropland) along with detected SP_{ascat} (red). The period DOY 80-140 is highlighted in blue.

3.4.3 Evaluation of the timing of SP_{ascat}

As a reference for spring leaf-out, PEP725 observations of BBCH-11 are used. All PEP725 sites with BBCH-11 leaf-out observations (LO_{pep}) are compared to SP_{ascat} of the grid cell in which the PEP725 site is located. This inter-comparison is done (i) using the mean LO_{pep} per site (averaged for all available species), and (ii) for every tree species individually. In addition to the PEP725 observations, we use the period of steepest increase in DBF LAI (LAI'_{max}) as a reference. Finally, as the spring reactivation in deciduous trees is mostly controlled by temperature (Polgar et al., 2011), we compare the SP_{ascat} dates to values of growing degree days (GDD) (McMaster et al., 1997). This approach uses the daily minimum and maximum temperatures. If the average daily temperature (3.1) is higher than a previously defined base temperature, the difference between the average and base temperature is added to the GDD (3.2).

$$T_i = \frac{T_{max,i} + T_{min,i}}{2} \tag{3.1}$$

$$GDD_{DOY} = \sum_{i=1}^{DOY} (T_i - T_{base}), \text{ if } T_i > T_{base} \tag{3.2}$$

The timing of phenological processes can then be compared to the GDD value at the respective DOY, and thus be related to the temperature time series since the beginning of the respective year. Different base temperatures and GDD values representative for particular phenological stages are found in literature. Lechowicz (1984) related observations of bud burst in different deciduous broadleaf tree species to a GDD value between 100 and 170 (base temperature 5°C). Fu et al. (2019) used a threshold of 5°C to study the control of leaf-out by day length and temperature. Sanz-Pérez et al. (2009) calculated GDD values from four thresholds (0, 3, 5, and 7°C) to predict bud burst in oak trees. In this study, we use a GDD value of 160 ($GDD160$), which we found to be the mean GDD for all available observations of LO_{pep} in moderate flatlands when using a base temperature of 5°C.

We first carry out a qualitative analysis of the correspondence between ASCAT and the reference variables. Then, we quantify the results using Pearson's correlation coefficient (r), root mean squared deviation (RMSD), average and median absolute difference (AAD, MAD) and bias. The overlap period of ASCAT and the three reference datasets is 2007 to 2016, allowing for a study period of 10 years.
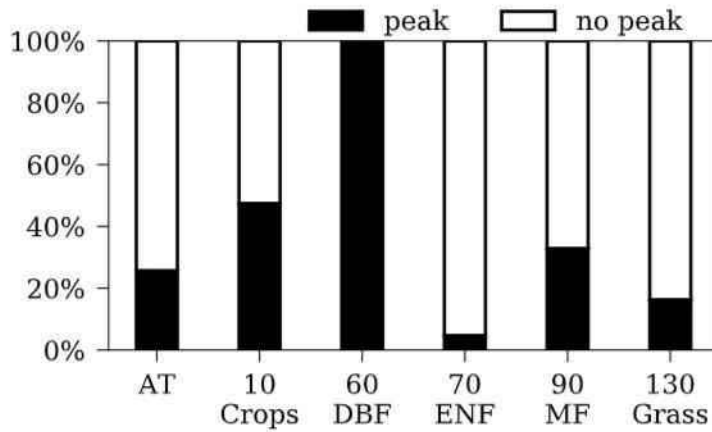
Fig. 3.5: Percentage of detected peaks for entire Austria (AT) and most frequent land cover types.

3.5 Results

3.5.1 Sensitivity to deciduous broadleaf forest

The visual inspection of the slope climatologies and time series and the detected SP_{ascat} showed that the SPD method succeeds in detecting all relative maxima that occur between DOY 80 and 140. We first conducted the SPD on the slope climatologies in order to obtain a robust SP_{ascat} distribution map. Spring peaks are found in 25% of all grid cells in Austria (Fig. 3.5). Of these, peaks occur in 100% of the grid cells dominated by DBF, in 47.4% of grid cells dominated by croplands, and in 32.8% of all grid cells dominated by mixed forest. In 95.3% of the grid cells dominated by ENF, no spring peak is found.

In a second step, we conducted the SPD on the slope time series. Fig. 3.6 shows the number of years in which a spring peak is detected for all of Austria. For each grid cell, the DBF fraction (x-axis) and the dominant land cover type (color coding) are indicated. For better visibility, the scale of the x-axis is adjusted for DBF fractions above 40%. Grid cells dominated by DBF show peaks in almost every year. The figure also shows that spring peaks do occur in grid cells with a low DBF fraction that are dominated by cropland. However, they are rare in grid cells dominated by ENF. This can likely be explained by the fact that ENF returns high backscatter over all incidence angles, whereas the cropland and DBF backscatter-incidence angle relationship is highly dynamic throughout the year. Thus, the DBF signal can dominate the signal over cropland in spring even if the DBF fraction is low, but cannot dominate the already relatively high backscatter over ENF.

Chapter 3 Does ASCAT observe the spring reactivation in temperate deciduous broadleaf forests?
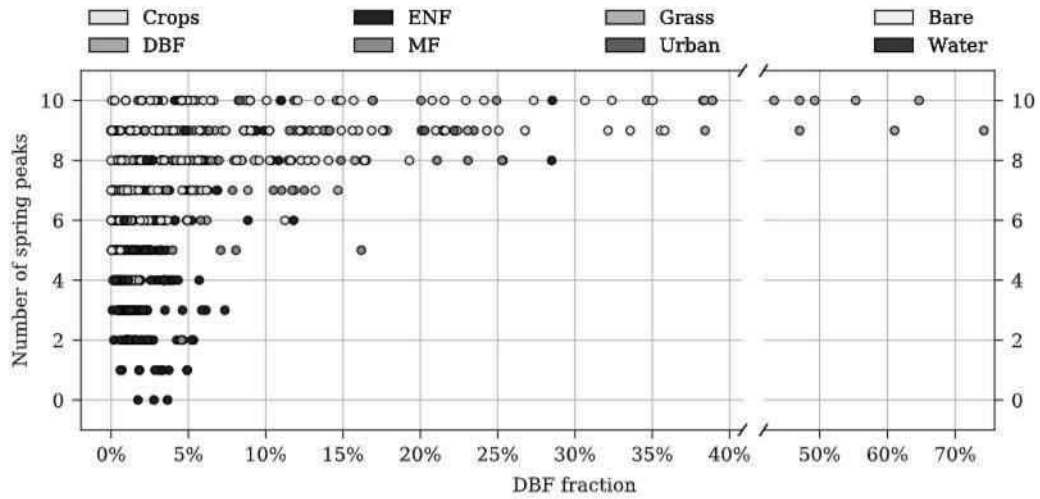
Fig. 3.6: Number of years with a spring peak (period 2007 to 2016). For each grid cell, the DBF fraction (x-axis) and the dominant land cover type (color coding) are indicated. For better readability, the scale of the x-axis is adjusted for DBF fractions > 40%.

3.5.2 Evaluation of the timing of SP_{ascat}

Qualitative analysis

Fig. 3.7 and 3.8 show examples of ASCAT slope time series for two selected grid cells, along with the LO_{pep} dates of different tree species (top), first derivative of the LAI time series (middle), and air temperature and thereof derived GDD (bottom). Dashed lines indicate the occurrence of SP_{ascat} (black), LAI'_{max} (green), and $GDD160$ (red). The grid cells are located in the transition zone between the northern edge of the Alps and the lowlands, and have a DBF coverage of 12% and 55%, respectively. The peaks are more pronounced in the 55% DBF grid cell, where SP_{ascat} marks the maximum, i.e., shallowest, annual slope. In the 12% DBF grid cell, the maximum slope usually occurs in summer and is related to the crop growing cycle. SP_{ascat} occurs closely to the LO_{pep} dates in most years. A similar agreement can be observed between SP_{ascat} and LAI'_{max}, as well as between SP_{ascat} and $GDD160$. Exact dates of SP_{ascat}, LO_{pep} of the individual species, LAI'_{max}, and $GDD160$ for the two grid cells are provided in Fig. S1 (Supplement).

Histograms of the timing of SP_{ascat} and the reference variables are shown in Fig. 3.9. For this analysis, only sites that are located in moderate flatlands were included. The top panel shows only grid cells that contain a PEP725 site. The histograms of SP_{ascat} in the top figure thus differ from the histograms in the middle and bottom panels.
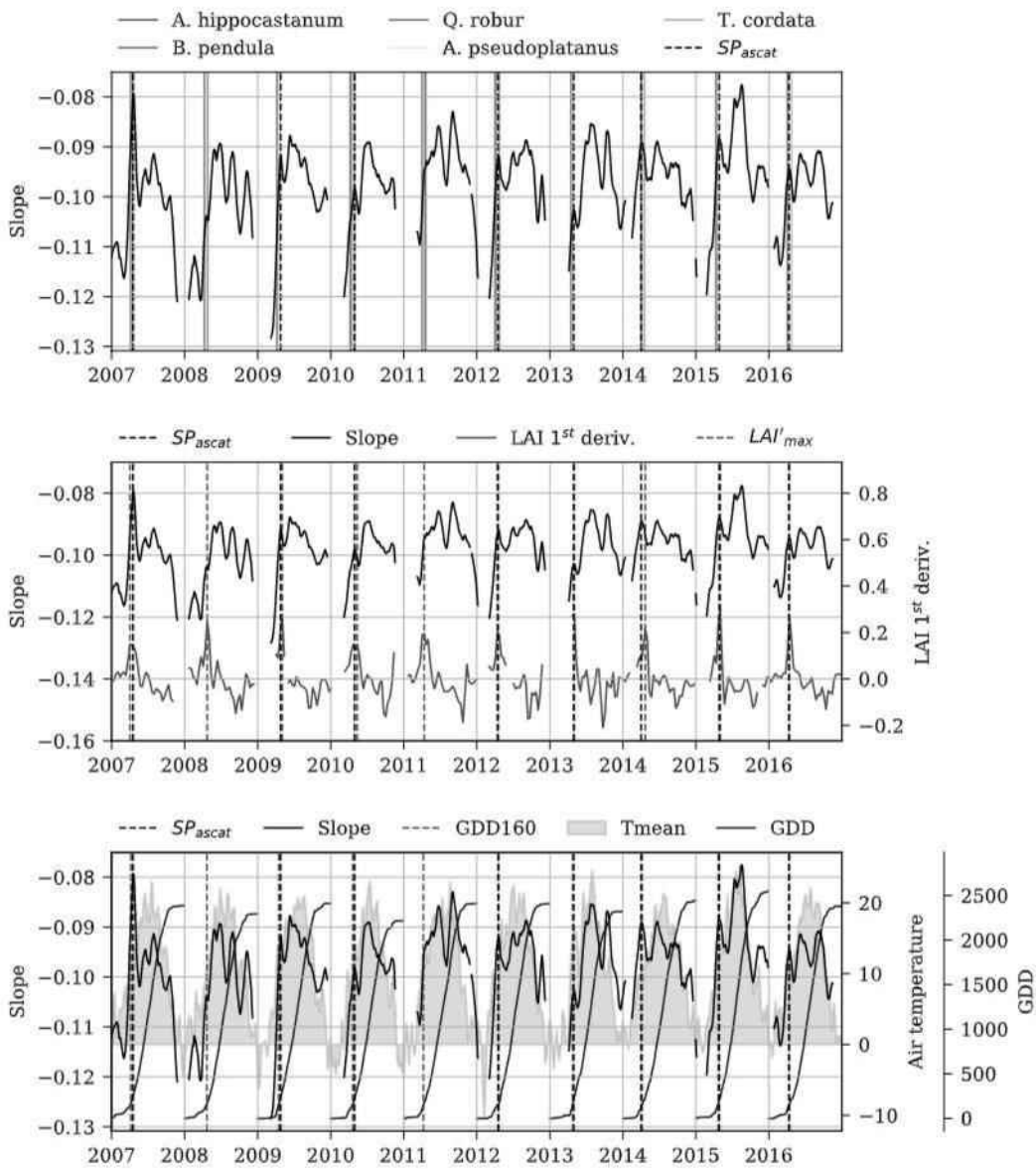
Fig. 3.7: ASCAT slope time series and (top) leaf-out dates of different tree types, (middle) first derivative of LAI time series (LAI'), and (bottom) 14-daily mean air temperature and GDD for a grid cell covered by 12% DBF (GPI: 2421559, lon/lat: 15.26 E/48.06 N). Values affected by frozen soil have been masked out in the slope and LAI' time series.
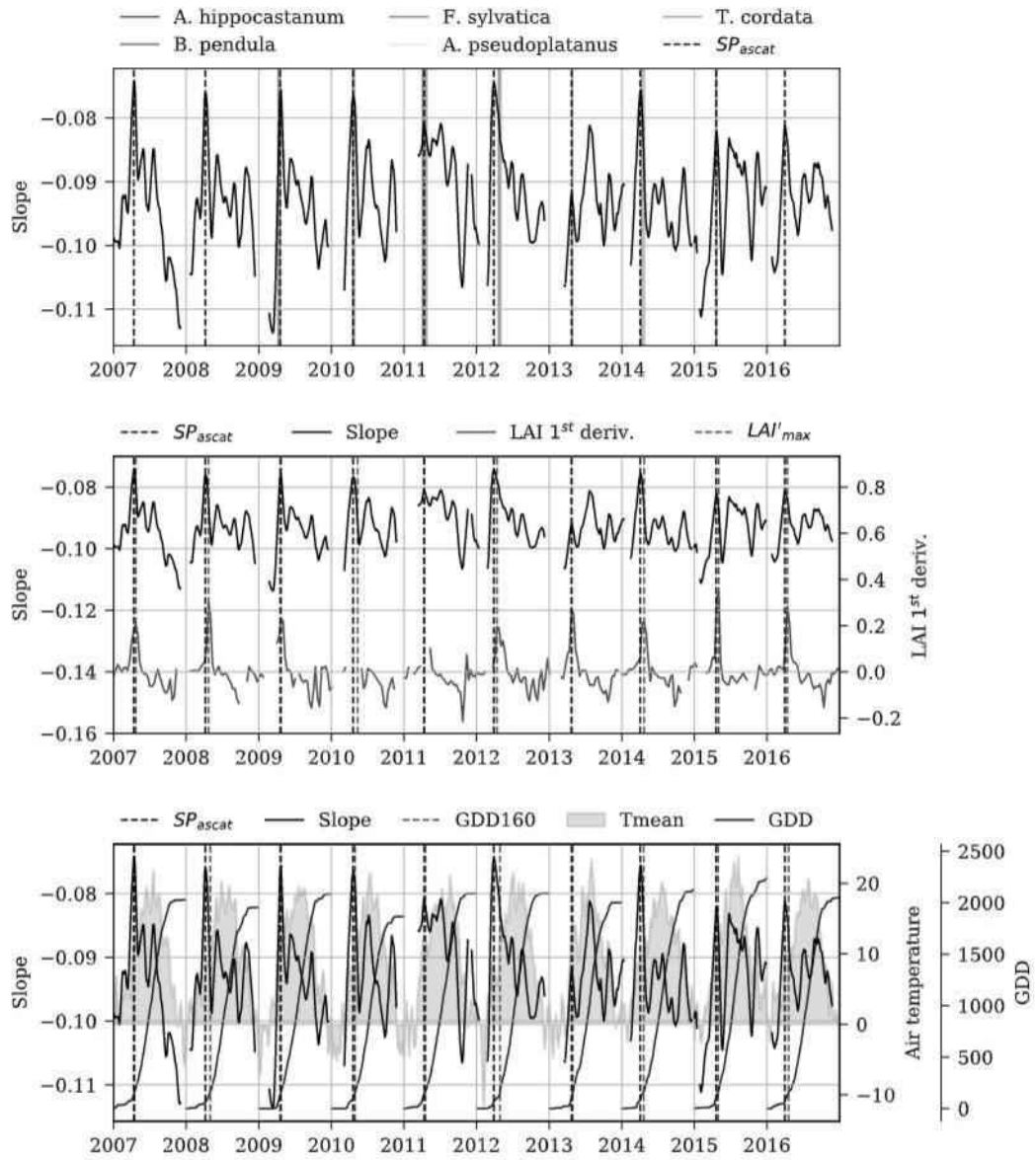
Fig. 3.8: Same as Fig. 3.7 for a grid cell covered by 55% DBF (GPI: 2421575, lon/lat: 15.93 E/48.06 N).

If more than one PEP725 site is located within a grid cell, all PEP725 observations within the cell are averaged.

LO_{pep} and SP_{ascat} show similar dynamics in most years, e.g., a relatively late occurrence in 2013 and a relatively early occurrence in 2012 and 2014. In the case of LAI'_{max}, due to the 10-daily time step, only certain DOY values are found. The timing of LAI'_{max} is in some years similar to SP_{ascat}, e.g. in 2011 and 2013, but in most years occurring later than SP_{ascat}, e.g. in the years 2008–2010 and 2014–2016, and thus also occurring later than LO_{pep}.

To see if the timing of SP_{ascat} is affected by temperature conditions, we carry out a comparison with $GDD160$. In most years, $GDD160$ and SP_{ascat} occur at a similar range of DOYs. In other years, e.g. 2011 and 2013, $GDD160$ is reached over a narrow range of DOYs. This indicates that the moderate flatlands region underlies similar temperature dynamics, and that the regional variation of $GDD160$ is smaller than that of SP_{ascat}. The observed year-to-year variations are very similar in both SP_{ascat} and GDD, indicating a strong dependency of SP_{ascat} on temperature conditions. In 2012, SP_{ascat} occurs earlier than in any other studied year, but in some grid cells also later than in any other year. The analysis of SP_{ascat} and $GDD160$ maps demonstrated that in 2012, the temperature differences between the (cooler) northern and (warmer) eastern and southeastern parts of Austria were particularly pronounced, which is reflected by the bimodal distributions found in SP_{ascat} and $GDD160$ in that year (see Supplement, Figs. S2 and S3).

Fig. 3.10 shows the mean difference between LO_{pep} and SP_{ascat} of individual species (top) and the number of included species per year (bottom) for all of Austria. A negative difference means that LO_{pep} occurs earlier than SP_{ascat}, and vice versa. Over all years, the mean difference between the leaf-out of a species and SP_{ascat} varies, but the order of the differences is relatively consistent per species: *Betula pendula* is followed by *Aesculus hippocastanum*, *Fagus sylvatica*, *Acer pseudoplatanus*, *Tilia cordata*, and *Quercus robur*; i.e., of the observed trees, the leaf-out of the white birch usually has the largest negative difference and the common oak the largest positive difference to SP_{ascat}. The number of samples per species is between 40 and 80 over most years. Apparent is the considerably larger positive bias in 2012, which is most likely related to the spatial differences in spring temperatures as described above.
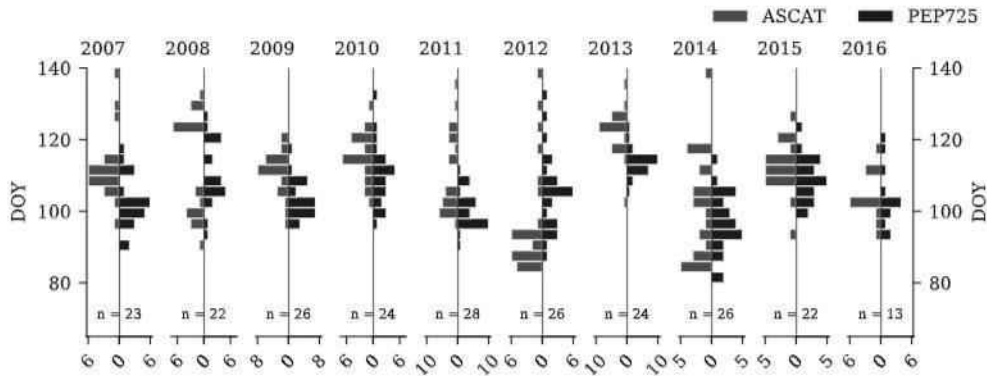
(a) SP_{ascat} vs. LO_{pep}
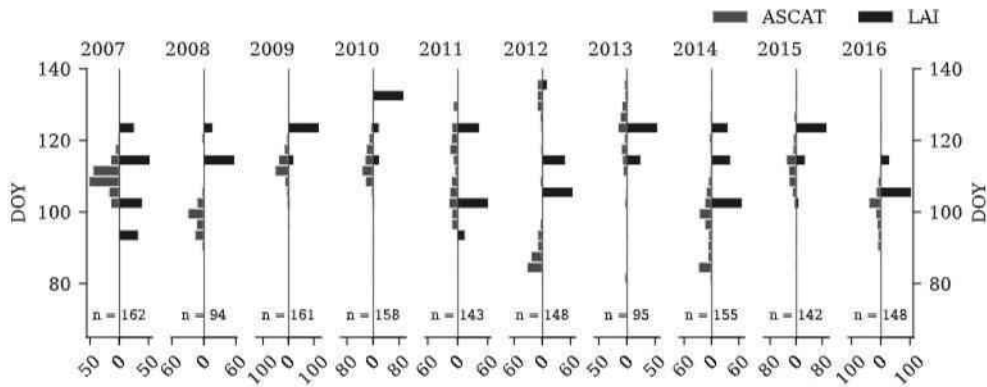
(b) SP_{ascat} vs. LAI'_{max}
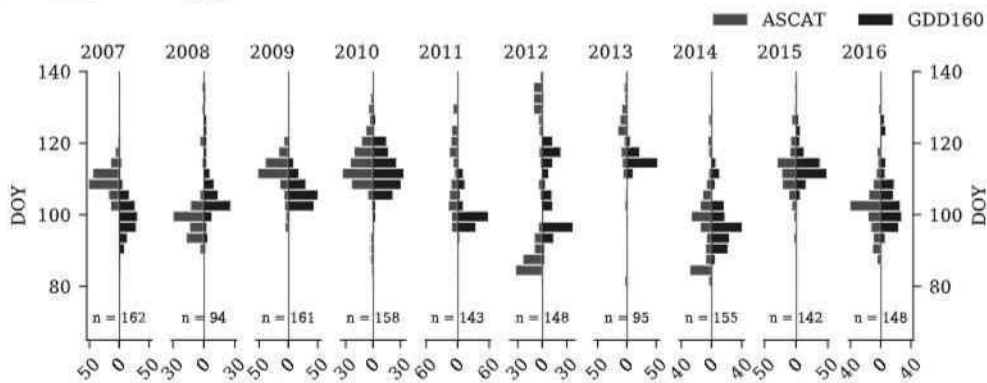
(c) SP_{ascat} vs. $GDD160$

Fig. 3.9: Yearly distributions of SP_{ascat}, LO_{pep}, LAI'_{max} and $GDD160$ (bin width: 3 days). The figures were created for all PEP725 sites (a) and ASCAT grid cells (b, c) located in moderate flatlands.
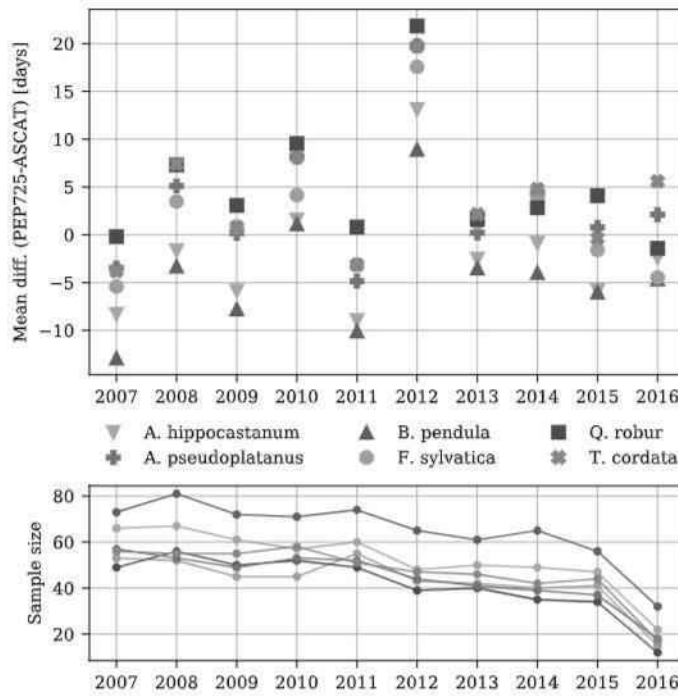
Fig. 3.10: Top: Mean difference between LO_{pep} and SP_{ascat} for each tree species. A negative difference means that LO_{pep} occurs earlier than SP_{ascat}, and vice versa. Bottom: Sample size. Turquoise/blue: diffuse-porous, orange/gold: diffuse- to semi-ring-porous, red: ring-porous species (Schoch et al., 2004).

Quantitative analysis

The metrics calculated between SP_{ascat} and the reference variables are provided in Table 3.3. For PEP725, the metrics were calculated between all PEP725 sites (average over all tree species) and the closest ASCAT grid cell for all available sites. For LAI and GDD, the metrics were calculated over all grid cells in Austria where a spring peak has been detected. In addition, the metrics were calculated for subsets of the sites depending on the DBF fraction in the respective grid cells. Significant Pearson r values ($p < 0.01$) are marked with an asterisk.

A relatively high correlation between SP_{ascat} and LO_{pep} of 0.49 is observed for grid cells with more than 10% DBF. For grid cells with a DBF fraction of more than 30%, no significant correlation could be derived between ASCAT and PEP725. The RMSD between SP_{ascat} and LO_{pep} is less than 15 days for all grid cells. MAD and AAD become smaller, the higher the DBF fraction, with a minimum MAD of 3.5 days and a minimum AAD of 6.6 days for cells with a DBF fraction greater than 40%.

RMSD, MAD, AAD values and biases below 9 days are observed for SP_{ascat} and $GDD160$, and correlations range from 0.46 to 0.58 for DBF fractions above 10%. In

Chapter 3   Does ASCAT observe the spring reactivation in temperate decid-
uous broadleaf forests?

Tab. 3.3: Metrics calculated between SP_{ascat} and LO_{pep}, LAI'_{max} and $GDD160$, for the years 2007 to 2016. Only grid cells with the given DBF fraction or higher have been included. n is the sample size. RMSD, MAD, AAD and bias are given in days. Significant Pearson r values ($p < 0.01$) are indicated by an asterisk.

	DBF fr.	n	r	p	RMSD	MAD	AAD	Bias
LO_{pep}	>0%	436	0.33*	0.0	14.0	9.0	11.0	-1.3
	>10%	140	0.49*	0.0	11.0	8.0	8.8	-1.0
	>20%	78	0.38*	0.001	10.6	7.8	8.6	-0.5
	>30%	18	0.31	0.217	9.9	5.0	6.9	0.9
	>40%	10	0.37	0.297	11.2	3.5	6.6	5.5
	>50%	8	0.04	0.929	12.4	3.5	7.6	6.3
LAI'_{max}	>0%	3398	0.07*	0.0	33.8	15.0	22.4	17.1
	>10%	932	0.17*	0.0	24.0	13.0	17.3	14.8
	>20%	448	0.11	0.017	27.4	13.0	19.1	17.8
	>30%	202	0.10	0.150	32.5	15.0	23.2	22.9
	>40%	77	0.26	0.023	24.0	13.0	16.8	16.5
	>50%	38	0.48*	0.002	14.5	13.0	12.0	11.4
GDD160	>0%	3540	0.14*	0.0	31.4	11.0	19.8	11.9
	>10%	925	0.54*	0.0	12.0	7.0	9.1	0.7
	>20%	448	0.58*	0.0	10.0	7.0	7.8	0.7
	>30%	202	0.50*	0.0	10.1	7.0	7.9	1.4
	>40%	77	0.50*	0.0	10.0	7.0	7.9	3.9
	>50%	38	0.46*	0.004	11.0	6.0	8.3	5.8

the case of LAI'_{max}, the RMSD, MAD, AAD values and biases are considerably larger, and only weak correlations are found. This can on the one hand be explained by the 10-daily time step of the LAI dataset, but could also indicate a systematic difference between SP_{ascat} and LAI'_{max}. As the bias shows, the differences between SP_{ascat} and LAI'_{max} are positive, meaning that LAI'_{max} usually occurs around two to three weeks later than SP_{ascat}.

Scatter plots of SP_{ascat} and the reference datasets are shown in Fig. 3.11. Included are observations from all years and grid cells with a DBF fraction above 10% (top) and above 40% (bottom). In the case of SP_{ascat} and LO_{pep}, the majority of points are found along the one-to-one line, indicating good agreement between the respective datasets. When only considering grid cells with a DBF fraction above 40%, the fit improves further. In the case of SP_{ascat} and LAI'_{max}, the positive bias towards later LAI'_{max} than SP_{ascat} is clearly evident for both DBF fractions above 10% and above
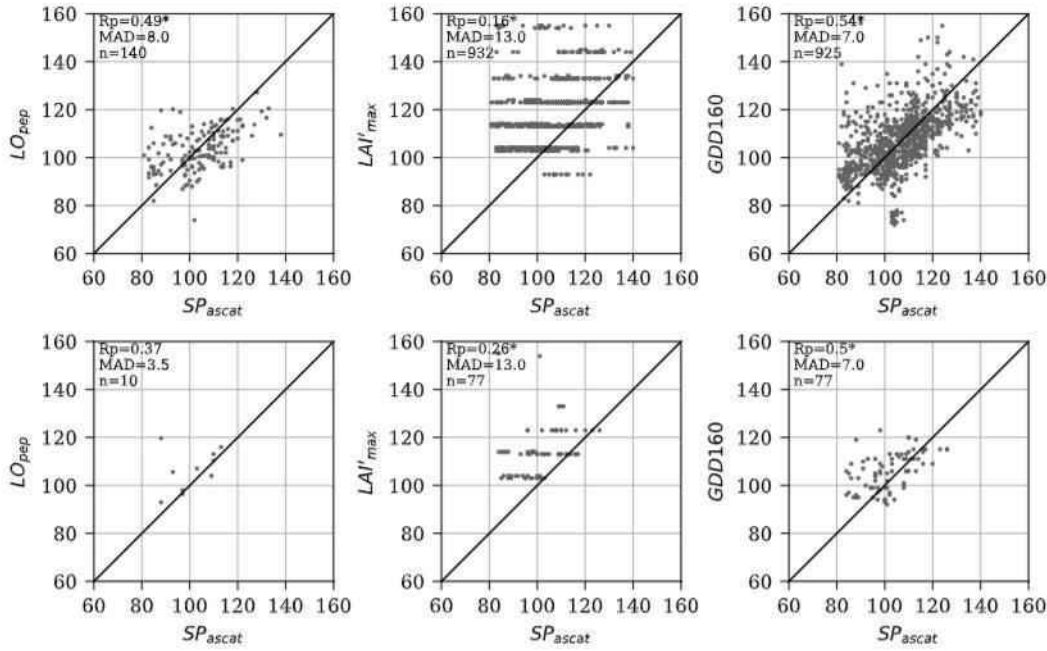
Fig. 3.11: Scatter plots of SP_{ascat}, LO_{pep}, LAI'_{max} and $GDD160$, including all sites with a DBF fraction of (top panels) 10% or higher, (bottom panels) 40% or higher. Significant Pearson r values ($p < 0.01$) are indicated by an asterisk.

40%. SP_{ascat} and $GDD160$ agree very well, and only a small bias towards later $GDD160$ than SP_{ascat} is found for grid cells with a DBF cover above 40%.

3.6 Discussion

Our first objective was to investigate if the observed ASCAT spring peak is caused by scattering within DBF. The challenge thereby is ASCAT's coarse resolution, which complicates the disentangling of effects from different land cover types in the observed signal. We investigated this by comparing the detected SP_{ascat} with land cover maps. Our analysis shows very good agreement with the occurrence of SP_{ascat} and DBF cover, and it also suggests that DBF can dominate the signal in spring even if a grid cell only has a small fraction of DBF. As can be seen in the slope time series (Figs. 3.4, 3.7 and 3.8), SP_{ascat} is however much more pronounced in a grid cell with high DBF fraction, and weaker in a cropland grid cell. Steele-Dunne et al. (2019) conducted a detailed study of ASCAT slope time series over extended grasslands in North America. They did not observe distinct spring peaks as described in our study, which also supports the hypothesis that SP_{ascat} comes from DBF and not from another land cover type. Further efforts to disentangle scattering

Chapter 3 Does ASCAT observe the spring reactivation in temperate deciduous broadleaf forests?

effects from different land cover types should be carried out in the future, using backscatter observations from the Sentinel-1 satellites. Sentinel-1 also observes in C-band and at a spatial resolution of 10 m, thus significantly finer than ASCAT. However, the Sentinel-1 satellites don't observe the surface at such a large range of incidence angles, and a slope parameter, as used in this study, cannot be derived in a robust, straightforward way. Many studies have shown that the ratio of C-band cross- and co-polarized backscatter is sensitive to vegetation water content and structure, as especially volume scattering and double-bounce effects are likely to cause polarization changes (Mattia et al., 2003; Satalino et al., 2013; Veloso et al., 2017; Vreugdenhil et al., 2018). Dostálová et al. (2018) compared the seasonality of Sentinel-1 cross-polarized (VH) backscatter from cropland, DBF, ENF and vineyards. Over DBF, they observed the highest backscatter values around the months of March and April, followed by a clear backscatter decrease, which they explain by higher absorption or more forward than backward scattering by the emerging leaves. At the same time of the year, they observed only a weak VH backscatter signal over cropland. It should however be mentioned that it is unlikely that the effects from different land cover types on the ASCAT grid cell can be completely separated. Every grid cell covers a number of vegetation types with different phenological stages, some of which affect the ASCAT signal more and some less. Thus, the slope time series (and all other time series derived from ASCAT) always represent the combined signal from the entire sensor footprint. We can try to find the causes of specific features in the time series, such as SP_{ascat}, but their timing and probably even more their shape not only depend on the underlying phenomenon but also on the vegetation types, soil moisture and surface roughness in the rest of the grid cell, as well as on the weather conditions before and during the period of interest and how they affect the different land cover types.

Our second objective was the evaluation of the timing of SP_{ascat}. We found good agreement between the timing of SP_{ascat} and phenological observations of leaf emergence. When interpreting those results, one must take into account that at some PEP725 sites, only one tree species is included in the database. The timing of leaf emergence of different tree species can vary in the order of several days to a few weeks. This complicates the comparison with ASCAT data, which observes the average signal of different species. Differences between SP_{ascat} and LO_{pep} can also be caused by the comparison of coarse scale satellite data with point scale phenology observations. Even if the average temperatures do not vary vastly over a grid cell, factors like elevation and exposition to sunlight due to the orientation of slopes, e.g., south- versus north-facing, can lead to differences in the timing of spring reactivation in particular trees. Such trees and thus phenological observations are

then not necessarily representative for the surrounding grid cell. However, according to the phenological observation guidelines followed by the PEP725 project (Koch et al., 2007), the observation of plants at sites which are not typical for the area should be avoided, and the majority of available data should thus be suited for our study.

The analysis of individual species revealed that the differences to SP_{ascat} usually occur in the same order. Lechowicz (1984) describes a correlation between the timing of leaf-out and diameter of the principal conducting elements, the xylem vessels. Trees with a narrow vessel diameter (diffuse-porous wood anatomy), including the species *Betula*, *Acer* and *Aesculus*, leaf out earlier than trees with a large vessel diameter (ring-porous wood anatomy) like *Quercus*, which corresponds with our findings. The fact that the observed differences are – in most years – centered around a difference of zero supports the hypothesis that SP_{ascat} is an indicator of the average spring dynamics of all deciduous trees in a grid cell. Average differences between SP_{ascat} and LO_{pep} are in the order of one to two weeks, which is comparable to findings by Lechowicz (1984), who stated that leaf emergence can vary over several weeks even within single forests. Kern et al. (2020) showed that the multiannual mean green-up duration (derived from MODIS NDVI pixels) is approximately 20 days in Austria. When comparing coarse ASCAT grid cells to point-scale phenology observations, differences of a few days to weeks are thus to be expected.

We found a strong dependence of SP_{ascat} on temperature conditions, here represented by $GDD160$. In 2013, temperatures below 0°C and snowfall occurred until the beginning of April in Austria, which is reflected by a late occurrence of $GDD160$ and SP_{ascat}. In addition, the DOY range over which SP_{ascat} and $GDD160$ occur is relatively short. In 2012 and 2014, SP_{ascat} occur early in the year in some grid cells and extend over a wide range of DOYs. As shown by $GDD160$, the spring months of 2012 and 2014 were relatively warm. Similar observations have been made by Kern et al. (2020), who found that if leaves start to emerge only late, the green-up duration of broadleaf forests tends to be shorter, and vice versa. In 2008 and 2012, $GDD160$ lags behind SP_{ascat} by approximately 10 days. A comparison with precipitation showed that the spring months in 2008 and 2012 were drier than in the other years, which perhaps led to earlier water uptake by the trees. How rainfall and soil moisture conditions affect the timing of SP_{ascat} needs to be investigated in detail in the future. Differences between SP_{ascat} and $GDD160$ might be due to the fact that GDD does not include any information on the length of the chilling period, which trees require as much as warming temperatures in spring. Moreover, the length of the period over which the GDD value was calculated is not taken into account: a low number of very warm days as well as a high number of

moderately warm days can both lead to the same GDD value but over a different amount of time.

The comparison of SP_{ascat} and LAI suggests that LAI'_{max} is in fact representative of a different phenomenon, as, despite the natural differences due to the 10-daily timestamp of the LAI dataset, the observed biases are all positive. To complement our analysis of LAI, we did a comparison with CGLS NDVI over DBF in our study region (Toté et al. (2017), Supplement Figs. S4-S6). The results do not differ much from the LAI-based analysis except that the NDVI time series showed a higher level of short-term variability which is likely caused by changes in atmospheric conditions and background reflection than by changes in DBF leaf cover.

Considering our results along with related literature, we explain the causes of the observed ASCAT spring peaks as follows. It is well known that the radar backscatter response depends on the dielectric properties and the roughness of the scattering medium (Ulaby et al., 1981; Ulaby et al., 1984; Fung et al., 1992; Wagner et al., 1999c). In the case of bare spring DBF, the "scattering medium" is characterized by the distribution of twigs and branches and their water content. The scattering from the twigs and branches increases the backscatter over all incidence angles, leading to a shallow slope of the backscatter-incidence angle relationship. At the same time, the backscatter contribution from bare soil is attenuated. This scattering mechanism differs from volume scattering, the term which is used for the scattering response from inhomogeneous media with randomly arranged scatterers with no dominant orientation. Volume scattering is for example found in fully developed crop canopies, dry snow packs and dry, sandy soils (Brunfeldt et al., 1984; Satalino et al., 2013; Ulaby et al., 1980; Jiang et al., 2007; Matzler, 1998). We suggest to use the term "twigs- and branches scattering" to describe the backscatter response from bare DBF, characterized by non-randomly oriented discontinuities (twigs and branches) in an otherwise homogeneous medium (air). The fact that in forests, scattering from discrete elements such as branches needs to be considered along with surface and volume scattering, has also been described in studies on radar backscatter modelling of forest stands (Richards et al., 1987; Sun et al., 1995). We thus conclude that SP_{ascat} represents the moment of maximum twigs- and branches scattering, i.e., the moment of highest water content in the woody parts of the deciduous broadleaf trees in the grid cell. As leaves start to emerge, the scattering and absorption properties of the DBF canopy change, leading to an attenuation of the incoming radiation and consequently a steeper slope. This behavior is illustrated in Fig. 3.12. LAI'_{max} on the other hand represents the average timing of leaf emergence for all trees in the grid cell. This discrepancy is not observed in the comparison with LO_{pep}, as these
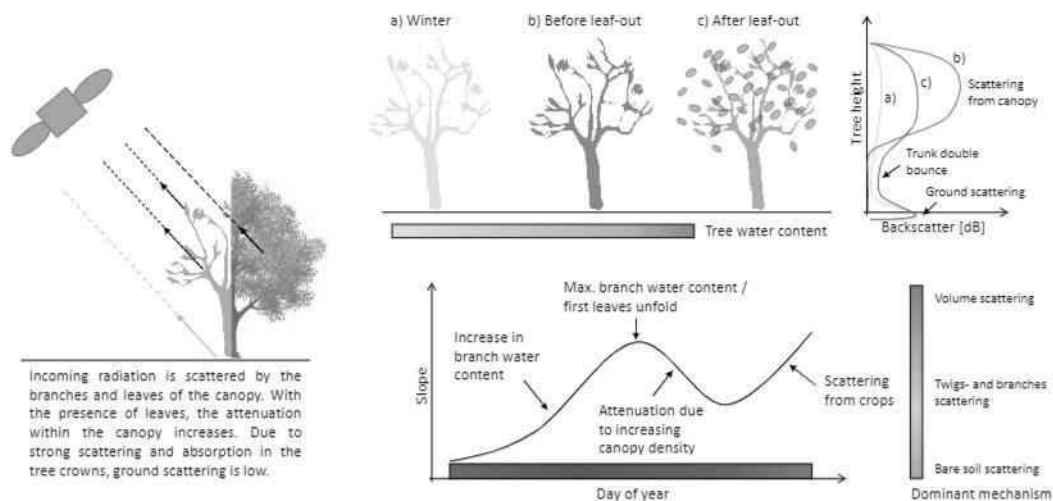
Fig. 3.12: Schematic illustration of the scattering processes causing a spring peak in the ASCAT slope. The change in tree water content in winter (a), before leaf-out (b), and after leaf-out (c) is illustrated in the top. The top right figure shows the idealized scattering response of the tree crown, tree trunk and ground. A characteristic slope time series over a mixed DBF-cropland grid cell is illustrated in the bottom, along with the underlying scattering mechanisms.

observations are point-scale, and the used phenological stage BBCH-11 explicitly indicates the timing of the first unfolding leaves.

More research is needed to extend the spatial applicability of the SPD method and to investigate also the shape of the spring peaks, in order to further relate the slope to an increase in woody water content. At best, this leads to a way of observing seasonal and interannual changes in DBF spring physiology over a large area and an increasing number of years which is independent of and complements satellite observations from optical sensors (Xiao et al., 2009; Yebra et al., 2013; Helman, 2018). As stated by Richardson et al. (2013), independent observations of physiological phenology are of high importance to models of current and future climate change and associated vegetation feedbacks.

Whereas DBF spring phenology has been extensively studied, autumn senescence has received less attention (Richardson et al., 2006; Vitasse et al., 2009; Gallinat et al., 2015; Gill et al., 2015). Due to the strong reaction of the ASCAT slope to spring phenology, a sensitivity to physiological processes in DBF in autumn is likely. Further investigation of ASCAT slope peaks at other times of the year is thus required to evaluate the sensor's suitability for the monitoring of phenological parameters in general.

Chapter 3   Does ASCAT observe the spring reactivation in temperate deciduous broadleaf forests?

3.7 Conclusions

We conclude that it is highly likely that ASCAT observes the spring reactivation in temperate deciduous broadleaf forests. We found a correspondence between the occurrence of DBF and a peak in the ASCAT slope time series between DOY 80 and 140. The timing of the observed peaks is correlated with phenological observations of leaf-out and temperature conditions. We also found a correspondence between the timing of the peaks and a steep increase in LAI, however, LAI'_{max} generally occurs two to three weeks after SP_{ascat}.

The observed flattening of the slope, which reaches its maximum before the average leaf emergence in the grid cells, appears to be linked to the increase in water content and the consequently stronger scattering from bare twigs and branches. This new hypothesis should be tested in the future, e.g., by extending the study area and by taking into account C-band backscatter measurements with a higher spatial resolution, as obtained for example from the Sentinel-1 satellites. Moreover, a comparison with in situ measurements of tree water content should be carried out.

More research on what the shapes of the peaks reveal and which other parameters related to DBF phenology can be derived from ASCAT observations will further increase our understanding of the sensitivity of C-band radars to large-scale eco-physiological changes in deciduous forests. In the short term, the results of this study represent a contribution to current research on how the ASCAT sensor reacts to temporary changes in the vegetation water content and structure in subsets of the sensor footprint.

Funding

Declarations of interest

The authors declare that they have no known competing financial interests or personal relationships that could have appeared to influence the work reported in this paper.

Acknowledgements

Supplementary data

See following pages.

GPI 2421559

Year	SP_{ascat}	A. hippocastanum	F. sylvatica	B. pendula	T. cordata	A. pseudoplatanus	Q. robur	LAI'_{max}	GDD160
2007	108	100		97	100	115	106	93	97
2008		101		100	102	110	116	114	112
2009	115	97		98	99	108	108	123	106
2010	120	99		100	107	115	119	133	111
2011		94		98	98	100	110	103	99
2012	108	96		93	101	120	117	104	110
2013	120	108		109	109	114	116	123	115
2014	92	91		91	93	113	108	113	97
2015	118	101		105	104	114	112	123	113
2016	102	96		96	96	113	113	104	104

GPI 2421575

Year	SP_{ascat}	A. hippocastanum	F. sylvatica	B. pendula	T. cordata	A. pseudoplatanus	Q. robur	LAI'_{max}	GDD160
2007	103							113	106
2008	98							114	123
2009	109	106	106	100	104			113	113
2010	110		109		117			133	120
2011	103		110	96	115			103	109
2012	88		118	114	120	127		104	119
2013	113		116	116	116			113	119
2014	93		112	101	102	107		113	111
2015	110							123	120
2016	91		110	111	110			104	110

Figure S1: Exact dates of SP_{ascat}, LO_{pep} (individual species), LAI'_{max} and GDD160, as shown in Fig. 7 and 8 (given in days of year).
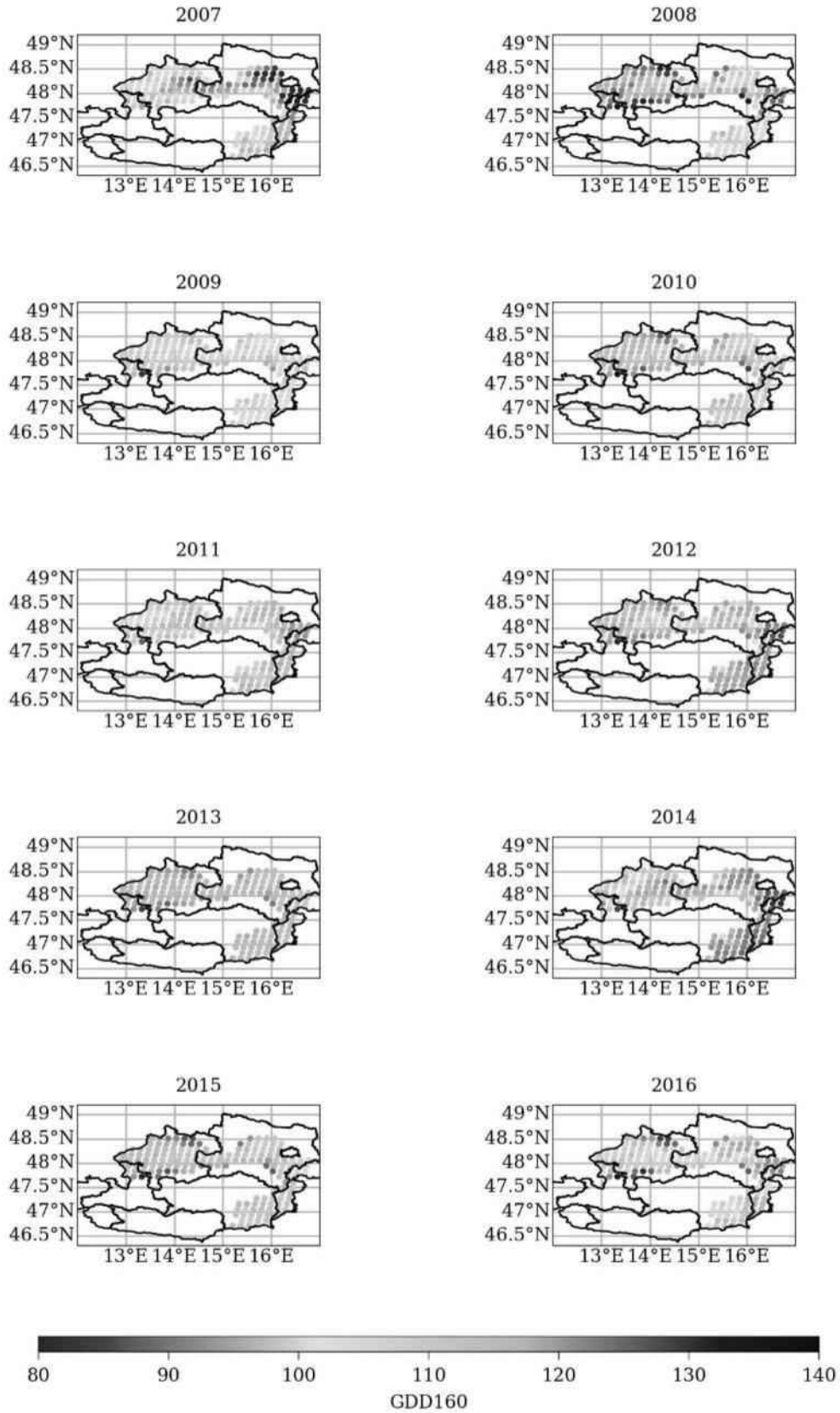
Figure S2: GDD160 for all ASCAT grid cells in moderate flatlands. In 2012, the temperature differences between the northern and the eastern and southeastern parts of Austria are stronger than in other years.
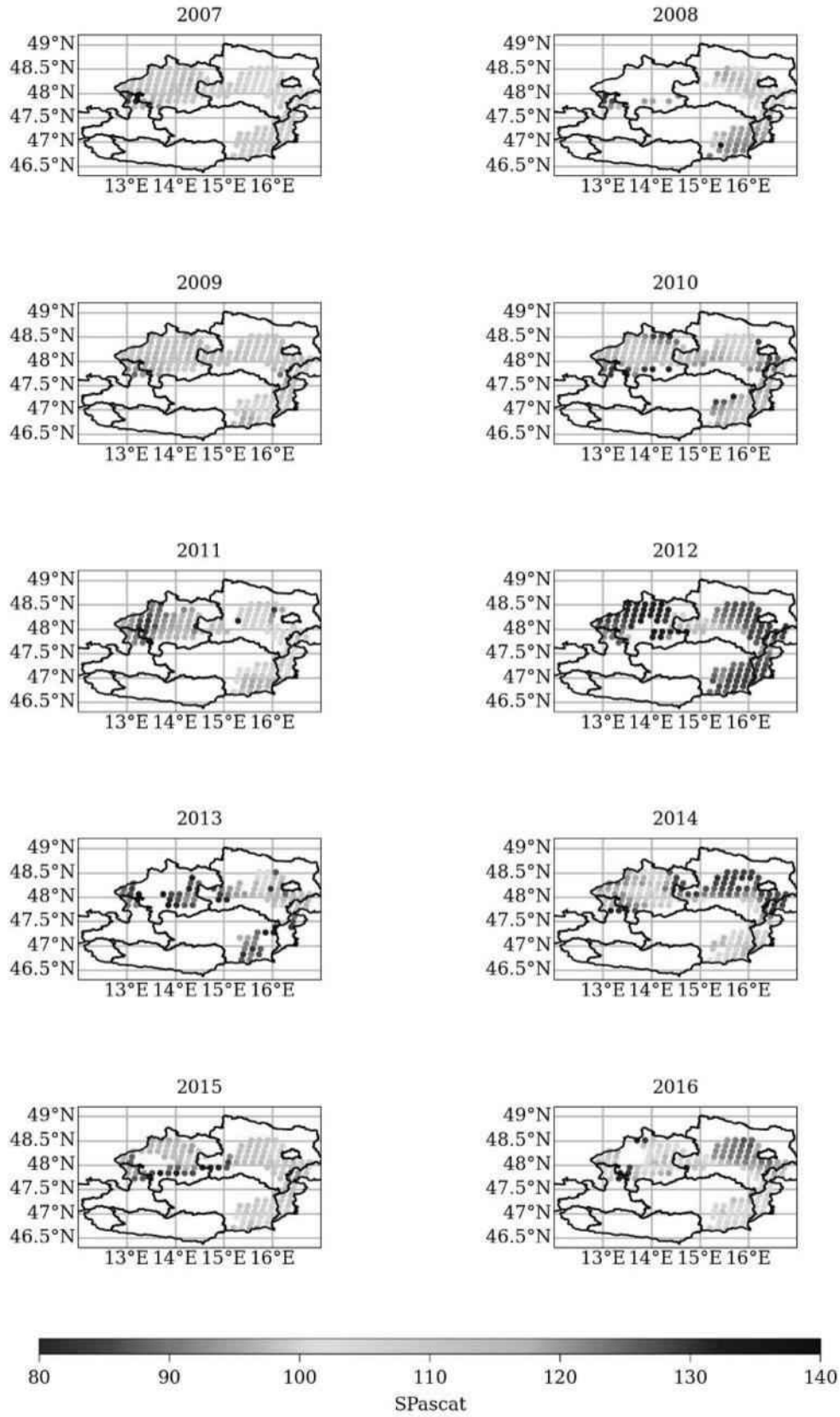
Figure S3: SP$_{ascat}$ for all ASCAT grid cells in moderate flatlands. In 2012, large differences between the northern and the eastern and southeastern parts of Austria lead to a bimodal distribution in the SP$_{ascat}$ histogram (Fig. 9).
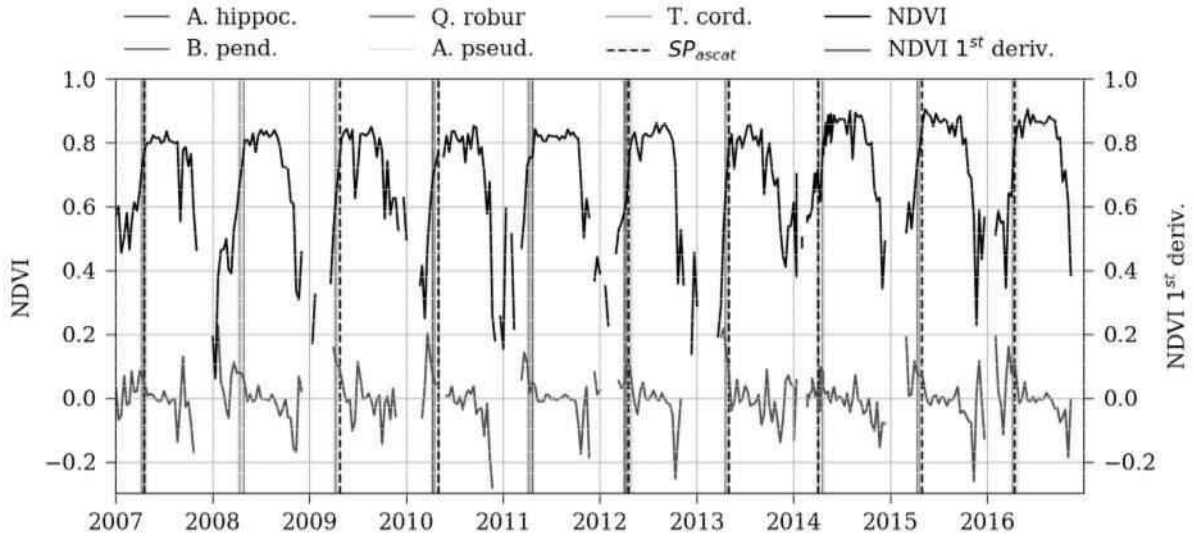
Figure S4: NDVI, first derivative of NDVI, LOpep and SPascat (GPI 2421559, 12% DBF cover).
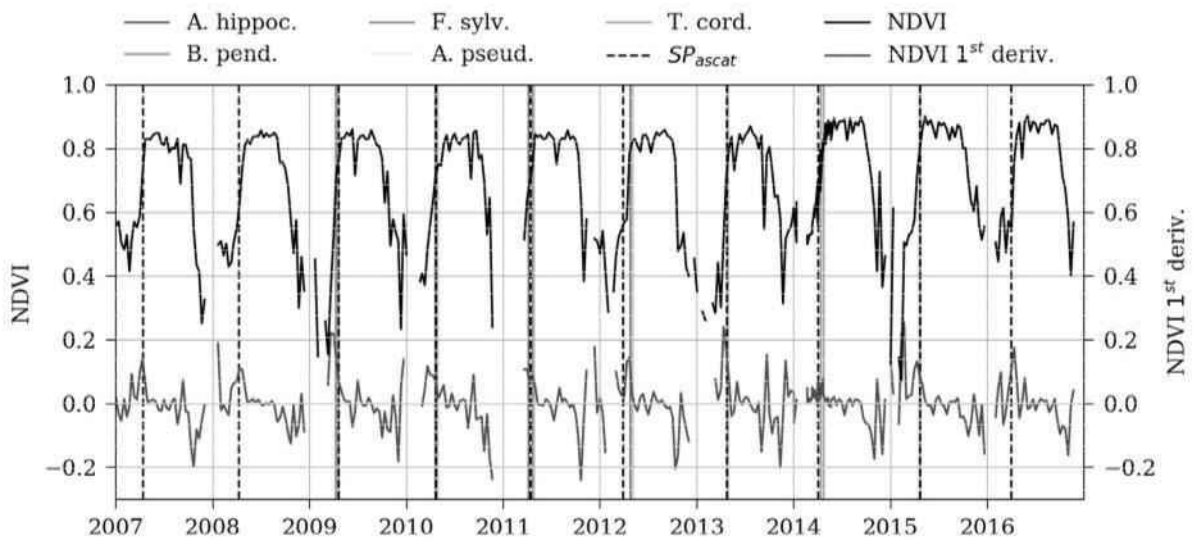
Figure S5: Same as Fig. S4 for GPI 2421575 (55% DBF cover).
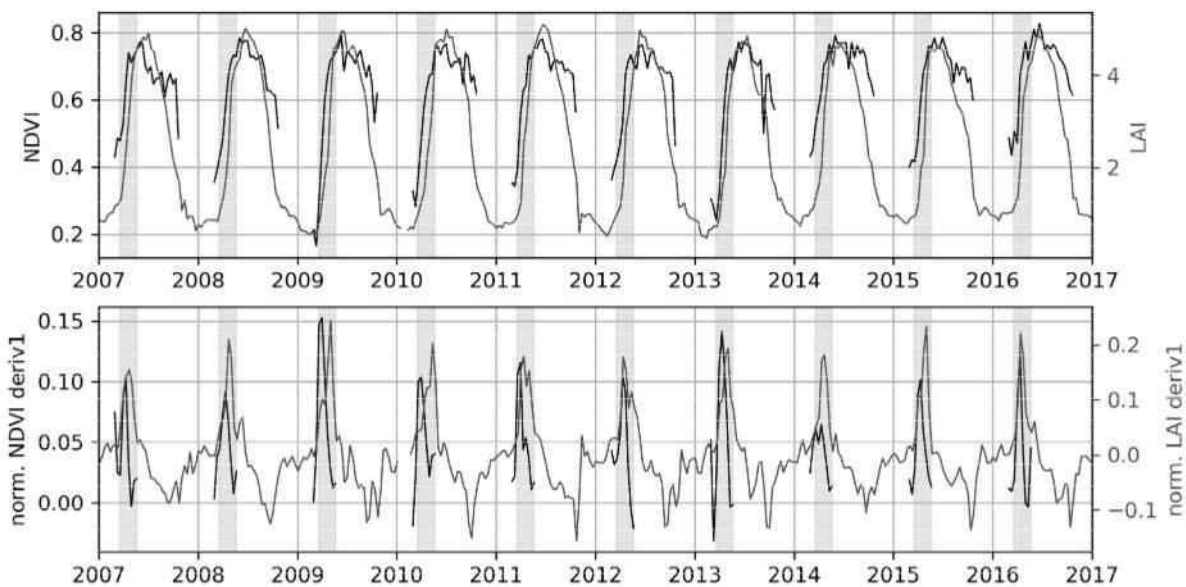
Figure S6: Average NDVI and LAI and their first derivatives over the moderate flatlands study area (only DBF pixels). Highlighted in grey: DOY 80-140.

Analysis of short-term soil moisture effects on the ASCAT backscatter-incidence angle dependence

> *Zweifel sind Ehrensache. (So viel Meer)*
>
> — **Nina FIVA Sonnenberg**
> (German musician)

Abstract The incidence angle dependence of C-band backscatter is strongly affected by the presence of vegetation in the sensor footprint. Many studies have shown the suitability of this dependence for studying and monitoring vegetation dynamics. However, short-term dynamics in the backscatter-incidence angle dependence remain unexplained and indicate that secondary effects might be superimposed on the vegetation component. In this study, we hypothesize that the observed short-term dynamics are caused by soil moisture. We investigate the effect by exploring relationships between the slope of the backscatter-incidence angle dependence (σ') from the Advanced Scatterometer (ASCAT) and soil moisture, rainfall, temperature, and leaf area index. We carry out the analysis over six study regions in Portugal, Austria, and Russia with different climate, land cover, and vegetation cycles. Our results indicate that soil moisture has an effect on σ'. Spearman correlations of σ' anomalies with soil moisture anomalies are stronger than with any other variable in most study

regions and range from -0.38 to -0.70. Even when accounting for effects of water on canopy, correlations between σ' and soil moisture remain relatively strong, ranging from -0.14 to -0.46. These results confirm the presence of secondary effects in the dynamic σ', which need to be corrected for when applying σ' in studies of vegetation dynamics. A correction may be achieved by the application of a suitable smoothing on σ' (i.e., removing high frequency signal components), by masking observations taken under wet conditions, or by the use of models that explicitly account for the effect of soil moisture on σ'.

4.1 Introduction

Earth observation using active and passive microwave sensors has a long tradition in the context of environmental research. Over land, these sensors show high sensitivity to changes in the soil and vegetation water content, surface roughness, vegetation structure, and, in the case of passive sensors, temperature. As opposed to optical radiation, microwaves can penetrate cloud cover and are independent of daylight. The first microwave missions were launched in the 1970s and 80s. Since then, they have provided global, continuous estimates of a variety of biogeophysical variables such as soil moisture (Wagner et al., 2013; Dorigo et al., 2017; Al Bitar et al., 2017; Chan et al., 2018; Bauer-Marschallinger et al., 2018), rainfall (Brocca et al., 2017), above-ground biomass (Santoro et al., 2015; Saatchi et al., 2007; Bousquet et al., 2021), plant water content (Konings et al., 2019), and gross primary production (Teubner et al., 2018). Microwave observations have further been successfully applied for the estimation of vegetation optical depth (VOD) (Owe et al., 2008b; Liu et al., 2011; Konings et al., 2016; Vreugdenhil et al., 2016) and the monitoring of vegetation dynamics (Frappart et al., 2020), the study of interactions between soil moisture and climate (Seneviratne et al., 2010), and in the context of food security (Karthikeyan et al., 2020). These studies have proven the suitability and multiple benefits provided by microwave observation systems. In light of climate change, the availability of high quality, reliable, and easily accessible data will be even more critical in order to study and understand its various impacts on the environment. This entails the constant development and assessment of algorithms and underlying assumptions, particularly with the availability of new missions with improved spatial, temporal, and radiometric resolutions.

In active microwave remote sensing, the characteristic interactions between the radar beam and the land surface lead to different scattering mechanisms. Over bare soil, surface roughness and soil water content cause diffuse scattering of the radar beam

at the boundary between the atmosphere and the land surface. Over vegetation, volume scattering in the canopy is the dominant scattering mechanism and controlled by canopy structure and water content. In addition, sudden changes in the canopy structure, e.g., over cropland and deciduous forest, may trigger specific scattering mechanisms and affect the observed radar signal. In the context of remote sensing of vegetation using scatterometers, the scattering characteristics of a vegetation canopy are exploited. In particular, the dependence of the observed backscatter values (σ^0) on the incidence angle (θ) has been found to carry valuable information (Wagner et al., 1999a). This dependence can be retrieved if (almost) simultaneous backscatter observations from different incidence angles are available for a target area, such as provided by the scatterometers onboard of the European Remote Sensing satellites (ERS-1, ERS-2) and their successor, the Advanced Scatterometer (ASCAT) onboard the series of Metop satellites. Wagner et al. (1999c) used the observation geometry of ERS to model the vegetation component (vc) in the backscatter signal based on the slope (σ') and curvature (σ'') of the backscatter-incidence angle dependence. Several studies confirmed a connection between σ' and vegetation dynamics and advanced the understanding of the underlying processes. Vreugdenhil et al. (2016) used a water cloud model to convert the long-term average σ' to VOD, a measure of the optical thickness of a canopy related to vegetation water content and structure, leaf area index (LAI), and biomass. Steele-Dunne et al. (2019) analyzed dynamic σ' time series over the North American prairie and showed the negative impact of a long dryspell on grasslands. Pfeil et al. (2020b) carried out a detailed study of the effect of spring reactivation in deciduous broadleaf forest on σ'.

Furthermore, Wagner et al. (1999c) used vc for disentangling the vegetation and soil moisture (SM) components in the ERS backscatter signal. They applied vc in order to correct for vegetation dynamics and retrieve SM using a semi-empirical change detection method (Wagner et al., 1999b; Wagner et al., 1999a). Since then, the approach has been developed further for ASCAT onboard the series of Metop satellites launched in 2006, 2012 and 2018 (Naeimi et al., 2009a). From their exploratory analysis of the ERS-1/-2 scatterometers, Wagner et al. (1999c) concluded that a SM effect on σ' and σ'' is weak or nonexistent. Therefore, they assumed that SM effects on σ' and σ'' can, in a first approximation, be neglected. This assumption has become part of the core postulates of the TU Wien SM retrieval algorithm (Wagner et al., 1999b; Vreugdenhil et al., 2016; Hahn et al., 2020).

Traditionally, vc has been modelled as a climatology (vc_{clim}), i.e., σ' and σ'' are modelled for every day of year. However, vegetation dynamics can vary significantly in different years due to meteorological conditions, and vc_{clim} is thus expected to be outperformed by a dynamic vegetation correction (vc_{dyn}) when used for the retrieval

of SM (Vreugdenhil et al., 2016). Melzer (2013) showed how σ'_{dyn} and σ''_{dyn} can be modelled in a robust way. The use of this vc_{dyn} for SM retrieval from ASCAT has been evaluated in different studies with mixed outcomes: Pfeil et al. (2018) analyzed the differences in ASCAT SM time series when using vc_{dyn} as opposed to vc_{clim} in an agricultural catchment in Austria. They found that the correspondence with in-situ SM does not improve significantly, contradicting the expectation. Steele-Dunne et al. (2021) analyzed ASCAT SM retrieved with vc_{clim} and vc_{dyn} over the United States. They concluded that the application of vc_{dyn} leads to improvements in the resulting SM dataset over regions with a temporal trend or changes in the amplitude or timing of phenological processes, but not in general, due to short-term variability in σ'_{dyn}.

Short-term dynamics in the order of several days to a few weeks in σ'_{dyn} have not been studied in detail. As vegetation growth processes usually take place on temporal scales of several weeks, it is likely that the observed short-term effects are in fact secondary effects superimposed on the vegetation signal at the coarse spatial resolution of ASCAT. A possible explanation was put forward by Quast et al. (2016), who used radiative transfer theory to model backscatter from the land surface. They found that, in contrast to the assumption made in (Wagner et al., 1999c), σ' and σ'' might in fact be significantly affected by SM. A recent study by Vermunt et al. (2021) found that interception and dew, i.e., water present on the canopy (WOC), impact L-band backscatter. In a follow-on study (Khabbazan et al., 2022), the authors demonstrated that interception and dew influenced retrievals of vegetation parameters. It is likely that this effect also plays a role, or is even stronger, in C-band microwave remote sensing as the wavelength is shorter and closer to the size of plant constituents.

The aim of this study is to advance the understanding of short-term variability in σ'_{dyn} and in particular the investigation of a potential SM effect on σ'. Whereas reference data for SM can be readily obtained from multiple sources, e.g., based on remote sensing data, land surface models, or data assimilation products, the availability of WOC reference data is currently limited to dedicated field experiments. Thus, we account for WOC only indirectly by masking potentially affected observations. As the effects are expected to be more pronounced on σ' than on its derivative, σ'', and the estimate of σ'' is less robust than the estimate of σ', we will not look at σ'' in this study. The main challenge of this investigation is that SM, WOC, and vegetation dynamics are closely related through the water, energy and carbon cycles, and disentangling the effects needs a careful analysis. Thus, we base the study on different types of analyses and aim at answering the following questions:

1. How do σ'_{clim} and σ'_{dyn} differ, and can we relate the differences to SM or LAI dynamics?

2. What are the correlations between anomalies of σ'_{dyn}, SM, rainfall, temperature, and LAI?

3. Is there a direct relationship between SM and the daily slope values, the so-called local slopes σ'_{local}?

4. Do SM variations explain short-term dynamics in σ'_{dyn} even when excluding observations potentially affected by WOC?

5. What is the magnitude of a potential SM effect on σ'_{dyn}?

The calculation of σ'_{local}, σ'_{dyn}, and σ'_{clim} will be described in section 4.3.1. Section 4.5 provides details on each analysis step, including the chosen WOC masking approach. We carry out the analysis for six regions in Austria, Portugal and Russia, which differ in climate, land cover, and the factors that limit vegetation growth.

4.2 Vegetation, soil moisture and roughness effects on σ'

An observed backscatter value (σ^0) is affected by the characteristics of the land surface in the sensor footprint, and by the different scattering mechanisms that are activated. This, in turn, is primarily controlled by the sensor's frequency and polarization, and the incidence angle of the observation (Ulaby, 1981). Figure 4.1 shows a generalized overview of different effects that contribute to σ^0. In the case of bare soil, the radiation is reflected on the surface, and with increasing surface roughness, a larger part of the radiation is scattered back to the sensor. If a surface appears rough or smooth to a scatterometer is defined by the size of the surface height variations, the wavelength of the radar beam, and the incidence angle. In general, σ^0 is higher over rough surfaces and decreases with increasing incidence angle. This decrease with increasing incidence angle is stronger for smooth surfaces. In addition, the soil water content plays a fundamental role in microwave remote sensing, as wet soil increases σ^0 due to its high dielectric constant and consequently higher scattering strength. As opposed to bare soil, a vegetation canopy appears as an inhomogeneous medium with a higher penetration depth, and thus acts like a volume scatterer, which scatters the incident radiation diffusely in all directions. In this case, the backscattered radiation fraction depends less on the incidence

angle. In addition to surface and volume scattering, double-bounce backscattering between vegetation constituents and the (soil or water) surface might occur. Double-bounce scattering is typical for flooded vegetation, e.g., paddy fields, but may also play an important role over croplands with predominantly vertically oriented plant constituents when observed with sensors that operate in vertical polarization mode. With increasing incidence angle, i.e., a longer pathway through the vegetation and thus decreasing canopy transmissivity, double-bounce effects are expected to become weaker (Xu et al., 2019). In most regions, except for, e.g., tropical rainforests or desert areas, the sensor footprint often covers a mixture of different land cover types, which also develop differently throughout the growing season. Thus, σ^0, as well as the sensitivity of σ^0 to the incidence angle of the observation (σ'), are usually affected by both surface and volume (and in some cases, double-bounce) scattering, and change over the year based on SM and vegetation conditions. Thereby, the presence of vegetation in the sensor footprint and the increase of vegetation water content and biomass during the growing season reduce the sensitivity to SM.

As stated in the introduction, recent studies suggest that the SM-induced increase of absolute backscatter might not be consistent across all incidence angles. As the attenuation of the radar beam by a vegetation canopy is higher at large incidence angles due to longer paths through the canopy, an increase in SM might increase σ^0 (expressed in dB) observed at low incidence angles more than at high incidence angles, leading to a steeper, i.e., more negative, σ'. This hypothesized process is shown in red in Figure 4.1. This would mean that σ' changes due to vegetation dynamics (rather long-term changes) as well as due to SM dynamics (rather short-term changes of a few days to weeks).

4.3 Datasets

Since SM and vegetation growth are closely connected through the water, carbon and energy cycles, we compare σ' not only to SM but also to LAI, rainfall, and surface temperature. LAI, representing vegetation growth and dynamics, is obtained from the Copernicus Global Land Service (CGLS). Surface temperature, as a proxy for photosynthesis and land-atmosphere exchanges in radiation- or temperature-limited areas, and rainfall data are obtained from the ECMWF Re-Analysis (ERA5-Land). An overview of the datasets is given in Table 4.1. We collected data from all datasets for the period 2007-2019. Timestamps with a surface temperature below 3°C or snow cover above 10% have been masked. Unless stated otherwise, we use time series that have been smoothed with a 42-day rolling Epanechnikov kernel in order
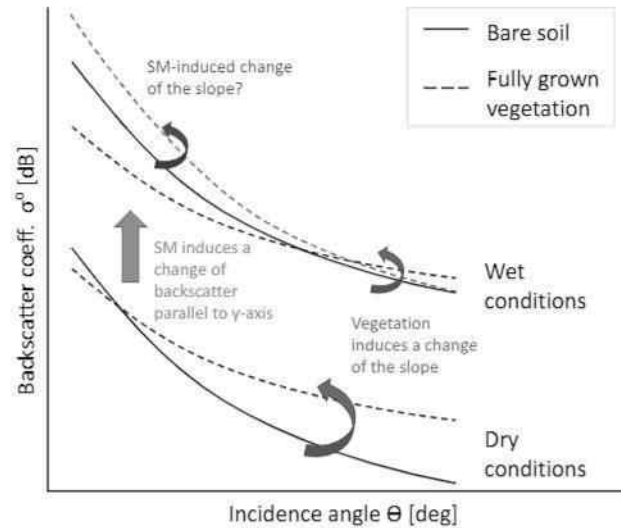
Fig. 4.1: Dependence of the backscatter coefficient on the incidence angle under dry and wet conditions, for bare soil and fully grown vegetation (after (Wagner et al., 1999c)). The hypothesized change of σ' due to SM variations is shown in red.

to match the TU Wien change detection σ' calculation (see section 4.3.1). This smoothing preserves the seasonal cycle as well as short-term events of several days to weeks, but removes events of shorter time scales, i.e., a few days or below. In the case of ASCAT, the Epanechnikov kernel is applied in order to obtain a robust estimation of σ'. Therefore, the observations are weighted based on their relative distance (d) to a given day using the following equation:

$$weight = 0.75 * (1 - d^2) \tag{4.1}$$

Both absolute and anomaly time series are used in this study. Anomalies are calculated by subtracting the long-term average (2007-2019) from the absolute values. The long-term average is obtained by applying a 5-day smoothing window on the time series (gap filling and short-term event correction), calculating the mean value for each day of year based on data from all available years, and applying a 30-day smoothing window on the resulting time series (long-term event correction). The long-term average thus represents the average annual seasonal cycle, without variations in the order of several days to weeks. The anomaly time series on the other hand contain only these short-term deviations from the long-term average, i.e., without a seasonal cycle.

Tab. 4.1: Overview of datasets.

Variable	Unit	Dataset	Spatial sampling
σ^0	dB	ASCAT	12.5 km
$\sigma'_{\text{clim}}, \sigma'_{\text{dyn}}, \sigma'_{\text{local}}$	dB/deg	ASCAT	12.5 km
Rainfall	m/h	ERA5-Land	9 km
Soil moisture (0-7 cm depth)	$m^3 m^{-3}$	ERA5-Land	9 km
Surface temperature	$°C$	ERA5-Land	9 km
Leaf area index	$[-]$	SPOT-VGT, PROBA-V	resamp. to ASCAT grid

4.3.1 Advanced Scatterometer (ASCAT)

We test our hypothesis using σ^0 observations and thereof derived σ' from the Advanced Scatterometer (ASCAT). ASCAT is a side-looking C-band radar onboard the Metop-A, -B, and -C satellites, which were launched in 2006, 2012, and 2018, respectively. Recently, Metop-A has reached its end, and was deorbited in November 2021. ASCAT observes the surface with a frequency of $f=5.255$ GHz across an incidence angle range of 25° to 53° (mid-beam) and 34° to 64° (fore- and aft-beams), and provides vertically co-polarized (VV) σ^0.

The description of the backscatter-incidence angle dependence, i.e. σ' and σ'', has been investigated in many studies. Please note that as stated in the introduction, we focus only on σ' in this study. Wagner et al. (1999c) estimated σ' based on all backscatter observations from a certain period of the year (slope climatology, σ'_{clim}). Later, Melzer (2013) showed that σ' can be derived for sliding time windows of a few weeks (dynamic slope, σ'_{dyn}). Hahn et al. (2017) compared σ'_{clim} and σ'_{dyn} and showed the robustness of the σ'_{dyn} calculation on a global scale. All these studies used backscatter observations from ASCAT or its predecessors, the scatterometers onboard the ERS-1 and -2 satellites (ESCAT). The calculation of both σ'_{clim} and σ'_{dyn} is based on the so-called local slopes, which can be derived from the (almost) simultaneous observations of the fore- (f), mid- (m) and aft-beams (a) provided by ESCAT and ASCAT:

$$\sigma'_{\text{mf}} = \frac{\sigma^0_m - \sigma^0_f}{\theta_m - \theta_f}, \quad \sigma'_{\text{ma}} = \frac{\sigma^0_m - \sigma^0_a}{\theta_m - \theta_a} \tag{4.2}$$

$$\theta_{\text{mf}} = \frac{\theta_m - \theta_f}{2}, \quad \theta_{\text{ma}} = \frac{\theta_m - \theta_a}{2} \tag{4.3}$$

Chapter 4   Analysis of short-term soil moisture effects on the ASCAT backscatter-incidence angle dependence

where σ^0 denotes the backscatter, θ is the incidence angle, and σ'_{mf} and σ'_{ma} are the local slopes (σ'_{local}). The dynamic slope, σ'_{dyn}, is estimated for every day by calculating a linear regression based on all σ'_{local} values within a window of ± 21 days, weighted by their temporal distance from the respective date using a rolling Epanechnikov kernel. The result of this linear regression are σ'_{dyn} and σ''_{dyn} of the respective date. The estimation of σ'_{clim} (and σ''_{clim}) is done in the same way, but using all observations from a certain period of all available years. In this study, we applied the same methods for the estimation of σ'_{local}, σ'_{clim}, and σ'_{dyn}, i.e., descriptions of the linear part of the backscatter-incidence angle dependence on different temporal scales.

σ' is generally exploited in three ways: First, it is used to normalize backscatter observations to any desired incidence angle. Second, σ' is used to correct for vegetation effects and the subsequently reduced sensitivity to SM in the TU Wien SM retrieval algorithm. Third, it is used to calculate VOD from ASCAT (Vreugdenhil et al., 2016) and for the study of vegetation dynamics (Steele-Dunne et al., 2019; Pfeil et al., 2020b). The main assumption underlying the latter two uses is that σ' is only affected by vegetation water content and structure, not by SM conditions (or other secondary effects). The assumption is based on early studies by Wagner et al. (1999c) who calculated differences between measured σ'_{local} and their first-order approximation and compared the variability of these differences for grassland, boreal forest, and perialpine forest regions. High variability in these differences would indicate the presence of natural short-term changes in σ'. They found the variability to be similar among the vegetation regions, although backscatter from forested areas is much more stable than the backscatter from grassland, and concluded that σ' is generally not affected by short-term changes of environmental conditions. Thus, they also expected correlations between σ' and SM to be weak. This study was based on ESCAT data from two years (1993 and 1994). Nowadays, backscatter samples are available for much longer periods and at higher spatial, temporal, and radiometric resolutions. It is thus possible to revisit and potentially update the interpretation by Wagner et al. (1999c).

4.3.2 CGLS Leaf Area Index

The Copernicus Global Land Service (CGLS) provides LAI from the SPOT-VGT and PROBA-V sensors (Camacho et al., 2013; Dierckx et al., 2014). In this study, version 2 of the dataset was used, which is available from 1999-June 2020 and has a spatial resolution of 1 km. The LAI data was spatially resampled to the scale of ASCAT

by averaging over all 1 km pixels within a 0.09° radius around the center of the respective ASCAT grid point.

4.3.3 ERA5-Land

Hourly SM, rainfall, and surface temperature were obtained from the ERA5-Land dataset (Muñoz Sabater, 2019) and resampled to daily averages. Surface temperature was included in the study to account for the fact that land-atmosphere exchanges are radiation- and/or temperature-limited in some regions. All time series used in this study were masked for cold and frozen conditions using daily surface temperatures (masked if temperature is below 3°C), and for snow cover (masked if snow content is greater than 10%).

4.3.4 CCI land cover

The dominant, i.e., most frequent land cover class for each ASCAT grid point has been derived from the CCI land cover dataset version v2.0.7, year 2015 (ESA, 2017).

4.4 Study area

We selected six regions of interest (ROIs) in Austria, Portugal and Russia in order to study SM and vegetation effects on σ' under different environmental conditions. These six regions have different dominant climate regimes, land cover types, and vegetation cycles. Table 4.2 provides an overview of the study regions, and the factors mainly limiting vegetation growth (estimated from Nemani et al., 2003, Fig. 1a). Long-term average annual temperature, SM, and LAI are shown in Figure 4.2 in order to illustrate differences of climate and vegetation growth between the ROIs. Note that short-term variations in the order of days to weeks are filtered out during the calculation of the long-term average. Average temperatures in Austria range from slightly below 0°C in winter to around 20°C in the summer months. SM is relatively constant throughout the year, with lowest values during the warm summer months. As shown by LAI, the growing season in cropland starts in March, peaks in June and ends around late September. In grassland, the peak of the growing season also happens around June, with a less sharp decline afterwards until autumn. In evergreen needleleaf forest, LAI increases constantly from around March to July and then decreases again until the end of autumn. The development is similar in

Tab. 4.2: Abbreviation, Koeppen-Geiger climate class, factors limiting vegetation growth (LVG), number of grid points (n), and center coordinates for the six regions of interest.

Region	Abbreviation	Climate	LVG	n	Center
Austria (cropland)	AT_cr	Dfb	radiation	79	16.14°E, 48.33°N
Austria (grassland)	AT_gr	Cfb, Dfb	radiation	23	13.84°E, 48.12°N
Austria (evergreen needleleaf forest)	AT_nf	Dfb,c, ET	radiation, temperature	86	14.90°E, 47.11°N
Portugal (tree, shrub mosaic)	PT_ts	Csb	radiation, water	93	7.46°W, 41.00°N
Portugal (cropland)	PT_cr	Csa	water	80	7.82°W, 38.37°N
Russia (sparse vegetation)	RU_sv	Dfc	temperature, radiation	102	108.20°E, 72.00°N

Russia. However, LAI is lower there due to the sparse vegetation cover. Average temperatures range from around -30°C to 10°C. In these four ROIs, vegetation growth is mainly limited by radiation and temperature. In Portugal on the other hand, vegetation growth is mainly water-limited. Average annual temperatures range from around 10°C to above 20°C. In summer, SM levels become very low. The peak of the growing season occurs around May/June, before the SM level reaches its minimum (around 0.15 m^3/m^3).

Figure 4.3 shows the average σ'_{dyn} time series for each ROI. Characteristic seasonal vegetation cycles, similar to LAI in Figure 4.2, can be identified. In addition, interannual variability due to different weather conditions is clearly visible in all ROIs. σ'_{dyn} is most dynamic over cropland, varying from below -0.15 dB/deg to -0.05 dB/deg. Lowest slope dynamics are observed over evergreen needleleaf forest, with slope values from around -0.10 dB/deg to -0.075 dB/deg. The steepest slopes are observed over sparse vegetation in Russia, where the average slope in the short growing season is around -0.15 dB/deg.

4.5 Methods

4.5.1 Correlation analysis - seasonal dynamics

In a first step, we analyze the seasonal dynamics of the climatology slope (σ'_{clim}) and the dynamic slope (σ'_{dyn}) by correlating the time series with LAI and SM (smoothed with a 42-day rolling window). If the short-term variations in σ'_{dyn} represent vegetation dynamics, we expect to see similar dynamics in LAI, and thus a strong correlation between LAI and σ'_{dyn}. On the other hand, if the short-term dynamics are caused by SM, the correlation between SM and σ'_{dyn} will be stronger than between SM and σ'_{clim}, and the correlation between LAI and σ'_{dyn} will be weaker
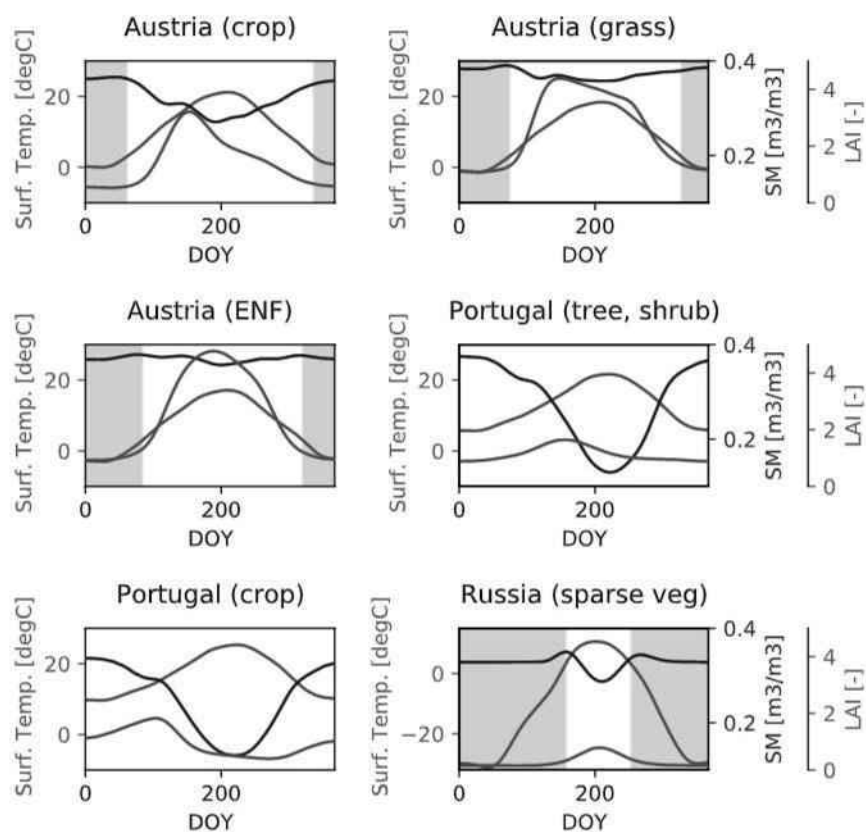
Fig. 4.2: Long-term average annual temperature, SM and LAI for every day of year (DOY). Periods where the average temperature is less than or equal to 3°C are shown in light blue. Please note the different temperature axis for Russia.

Chapter 4 Analysis of short-term soil moisture effects on the ASCAT backscatter-incidence angle dependence
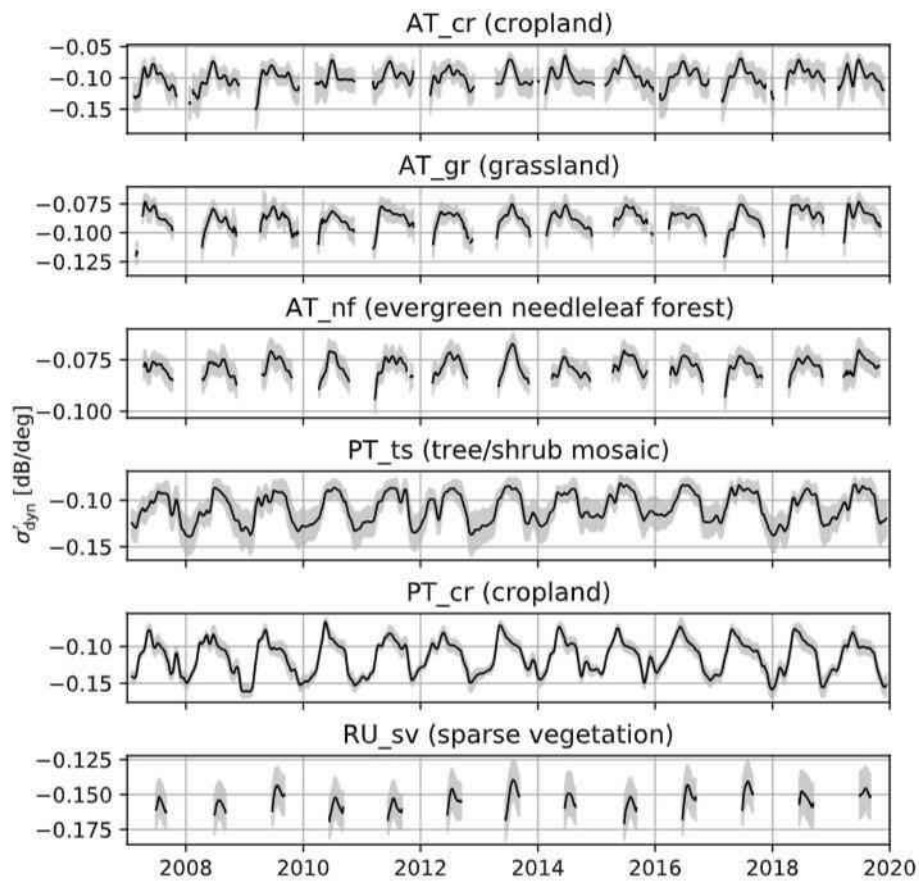
Fig. 4.3: Average σ'_{dyn} time series for each ROI (black). The grey shaded area shows the ± 1 standard deviation range within each ROI.

than between LAI and σ'_{clim}. Please note that we are not primarily interested in absolute correlations here, as the seasonal cycle in all variables will lead to high correlation values without necessarily bearing causality (Papagiannopoulou et al., 2017). Instead, we only look at the relative differences in the correlations of LAI and SM with σ'_{clim} and σ'_{dyn}. We use Spearman's rank correlation coefficient, as the variables might be non-linearly related.

4.5.2 Correlation analysis - anomalies

Next, we carry out a correlation analysis on anomaly time series, i.e., time series where the long-term seasonal cycle has been subtracted. As mentioned above, this is critical in the case of variables with a strong seasonal cycle, as potential (non-)correlations in the short-term dynamics of the variables will always be outweighed by long-term similarities. In this step, we also include rainfall and temperature anomalies in addition to SM and LAI, as short-term vegetation dynamics might rather be reflected (indirectly) in these variables than in LAI. In addition, we carry out a multiple linear regression (MLR) in order to test the explanatory power of anomalies of the individual variables, as well as combinations thereof, on dynamics in σ'_{dyn}. The explanatory power is given by the coefficient of determination, R^2, and is calculated using the ordinary least squares (OLS) function of the *statsmodels* Python package.

4.5.3 Local slopes analysis

As described in section 4.3.1, σ'_{dyn} is based on the weighted σ'_{local} values of all observations within a ± 21-day window. Thus, potential short-term effects of SM are reduced in σ'_{dyn} (as well as in σ'_{clim}), but much more pronounced in σ'_{local}. In the presented analysis, the uncertainty in the local slopes is reduced by averaging the local slope pairs:

$$\sigma'_{\text{local}} = \frac{\sigma'_{\text{mf}} + \sigma'_{\text{ma}}}{2}, \quad \theta_{\text{local}} = \frac{\theta_{\text{mf}} + \theta_{\text{ma}}}{2} \tag{4.4}$$

We look at changes of the observed σ'_{local} and compare them to the corresponding changes in SM. For this purpose, we use the SM value from the timestamp closest to the ASCAT observation, as opposed to the 42-day smoothed values that were used before. In case of a SM effect on the slope, we expect the slope to become steeper as SM increases. As σ'_{local} is calculated for each observation, the values are

not yet normalized for incidence angle effects. Thus, this analysis is carried out per incidence angle (rounded to full integers). We do a visual analysis of the σ'_{local} dynamics during and after rainfall events in order to support the discrimination of SM and vegetation effects in σ'_{local} and, subsequently, σ'_{dyn}.

4.5.4 Indirect assessment of WOC effects on the ASCAT slope

A recent study by Vermunt et al. (2021) using L-band backscatter suggested that water on canopy (WOC), due to, e.g., interception and dew, may affect the backscatter significantly. It is assumed that C-band σ^0 and σ' are also strongly affected by WOC. However, these effects are poorly understood, and it is not known how ASCAT's sensitivity to SM changes when WOC is present. In order to investigate correlations between σ' and SM and at the same time reduce the uncertainty with respect to WOC, we apply an indirect WOC masking: First, we identify all σ'_{local} observed on days with rainfall (maximum rainfall value greater than 1 mm/h) and remove these observations. Moreover, we exclude all observations from morning overpasses (before 10:00 am), as dew is expected to occur mainly in the morning hours. Just like in the previous sections, we then derive the σ'_{dyn} time series based on all remaining σ'_{local} values within a ± 21-day window. This modified σ'_{dyn} is referred to as $\sigma'_{\text{dyn,nWOC}}$ ("dynamic slope, no water on canopy"). The assumption that we take here is that a potential WOC effect on the slope lasts shorter than a SM effect, as the drying of the leaves happens more quickly than the decrease in SM. The proposed approach is not expected to provide a perfect masking of WOC. For example, WOC may persist for a longer duration depending on weather conditions and leaf structure. Nonetheless, in the absence of reference data for WOC, the proposed masking is adopted as a meaningful indirect indicator of WOC. It also has to be noted that the estimation of $\sigma'_{\text{dyn,nWOC}}$ is less robust than the original σ'_{dyn} due to the reduced number of σ'_{local}.

Similar as in section 4.5.3, SM, σ'_{local}, σ'_{dyn} and $\sigma'_{\text{dyn,nWOC}}$ are visually compared to each other and analyzed for selected grid points. Then, we redo the correlation analysis from section 4.5.2 with $\sigma'_{\text{dyn,nWOC}}$ and compare the results with the correlations obtained with σ'_{dyn}.

4.5.5 Quantification of SM effects on the ASCAT slope

Finally, we provide an estimate of the magnitude of SM effects on σ'_{dyn} by calculating linear regressions between anomalies of 42-day smoothed SM and σ'_{dyn}. The

regression line is used to obtain the change in σ'_{dyn} at the largest positive (wet) SM anomaly that occurred in each ROI. Then, the order of magnitude of the change in σ'_{dyn} is related to the characteristic σ'_{dyn} dynamics in each ROI.

4.6 Results

4.6.1 Correlation analysis - seasonal dynamics

Figure 4.4 shows example time series of σ'_{clim}, σ'_{dyn}, SM, and LAI for a grid point in Marchfeld, an agricultural region in eastern Austria. All four variables show a characteristic seasonal cycle and inter-annual variations, e.g., lower maximum values in σ'_{dyn} and LAI in 2017, 2018, and 2019, and short-term variations in σ'_{dyn} and SM. As can be seen in the figure, some of the short-term variations in σ'_{dyn} correspond to variations in SM, but not to LAI, which shows relatively smooth temporal dynamics apart from inter-annual variations in the absolute values. For this grid point, the Spearman correlations between σ'_{clim} and SM, and σ'_{clim} and LAI are -0.53 and 0.86, respectively. The correlations of SM and LAI with σ'_{dyn} are -0.72 and 0.70, i.e., the correlation between SM and σ'_{dyn} is -0.19 lower (stronger) than with σ'_{clim}, whereas it is 0.16 lower (weaker) for LAI and σ'_{dyn} than LAI and σ'_{clim}. We calculated these correlations for all grid points in the six ROIs and found a consistent behavior (Figure 4.5): for all ROIs, the median correlation between SM and σ'_{dyn} is stronger than between SM and σ'_{clim}, whereas the opposite is true for LAI, except for the PT_cr ROI, where the correlation between σ'_{clim} and LAI is slightly lower. The weak correlations in PT_cr can be explained by a relatively quick drop in LAI in early summer, which in most years corresponds to the timing of the shallowest slope, but after the peak, the slope values decrease more gradually. An example of this behavior is shown in Figure 4.6 for a grid point in Portugal dominated by non-irrigated arable land. Figures 4.4 and 4.6 also show that there is a small time lag between σ' and LAI, which is due to a sensitivity to different biophysical parameters: whereas LAI is a representation of the photosynthetically active leaf area per surface area, σ' is sensitive to the vegetation density, water content, and vegetation structure. These time lags are typically of a few weeks and have been observed for σ' (Pfeil et al., 2018) and the closely related VOD (Jones et al., 2011).
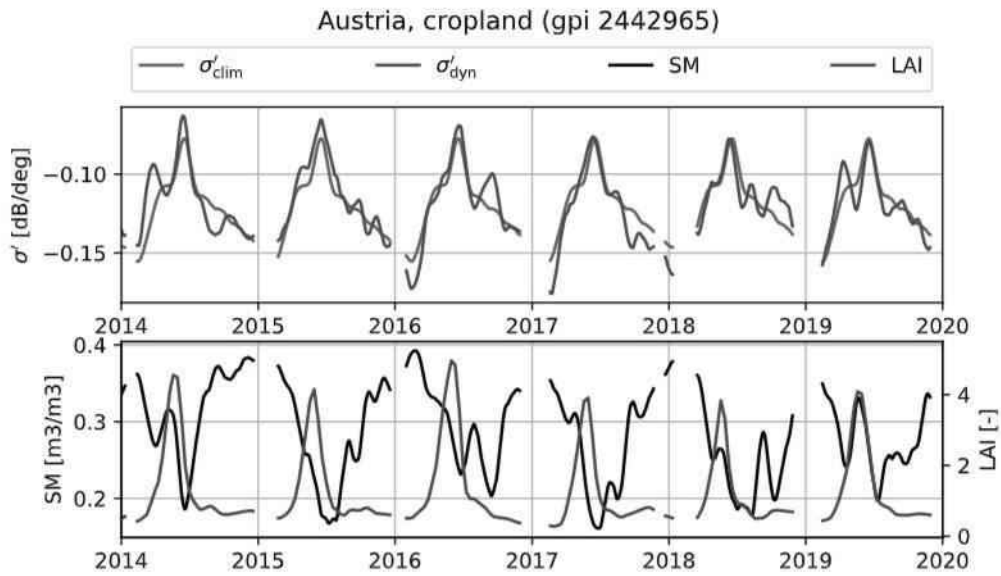
Fig. 4.4: σ'_{clim}, σ'_{dyn}, SM and LAI for a grid point in AT_cr (lon: 16.79°, lat: 48.62°).
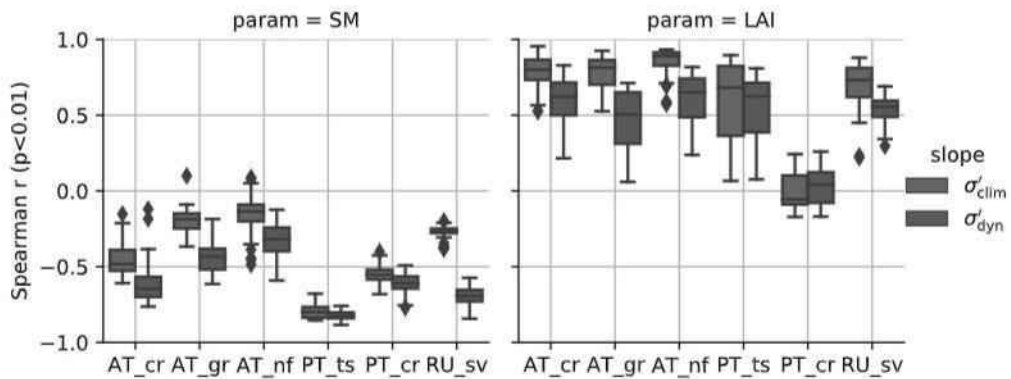
Fig. 4.5: Spearman correlation coefficient (r) of σ'_{clim} and σ'_{dyn} with SM and LAI, for each ROI. Only grid points with a significant correlation ($p < 0.01$) are included. The boxes show the quartiles, and the whiskers show the rest of the distribution. The horizontal line inside the boxes shows the median value. Outliers are shown by diamonds.

Portugal, cropland (gpi 1993782)
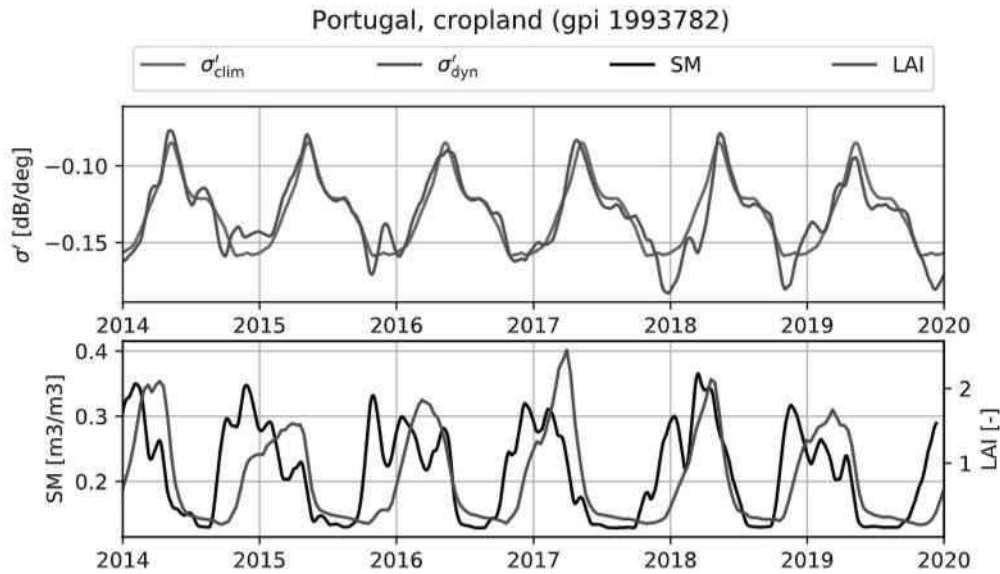
Fig. 4.6: σ'_{clim}, σ'_{dyn}, SM and LAI for a grid point in PT_cr (lon: -8.09°, lat: 37.82°).

4.6.2 Correlation analysis - anomalies

In a next step, we calculated Spearman correlations between anomaly time series, i.e., time series where the long-term seasonal cycle has been removed. Table 4.3 shows the median correlation for each ROI. For all ROIs except PT_cr, the correlation is strongest between σ'_{dyn} and SM, ranging from -0.37 to -0.70. For PT_cr, the correlation is strongest between σ'_{dyn} and rainfall (-0.51), but also relatively high between σ'_{dyn} and SM (-0.45). The correlations with LAI range from -0.14 to 0.26 and are thus much weaker than with SM and rainfall. As shown in section 4.6.1, LAI does not show large short-term dynamics, and inter-annual variations mainly show in the absolute values and the long-term development of LAI throughout the growing season. The correlations with temperature anomalies range from 0.23 to 0.43, which most likely reflects the close relationship between temperature and SM, i.e., drying of the soil with higher temperatures and evaporation rates. The fact that the σ'_{dyn} correlations with rainfall and SM are higher than with temperature suggests that the short-term dynamics in σ'_{dyn} do not represent temperature-induced vegetation dynamics, e.g., by an increased water demand from the atmosphere leading to water uptake by the leaves, but more likely a direct SM effect.

The OLS analysis has the advantage that also multivariate relationships can be tested. The R^2 coefficient represents the percentage of variation in the σ'_{dyn} anomalies that can be explained by another variable or combinations thereof (Figure 4.7). LAI has been excluded here because of the weak correlations with slope anomalies as shown

Chapter 4 Analysis of short-term soil moisture effects on the ASCAT backscatter-incidence angle dependence

Tab. 4.3: Median Spearman correlation (significant at p<0.01) between anomalies of σ'_{dyn} and the given variable. The maximum absolute correlation is given in bold.

Region	Rainfall	Soil moisture	Temperature	LAI
AT_cr	-0.49	**-0.52**	0.43	-0.07
AT_gr	-0.34	**-0.51**	0.41	-0.14
AT_nf	-0.24	**-0.37**	0.35	0.10
PT_ts	-0.44	**-0.52**	0.32	0.10
PT_cr	**-0.51**	-0.45	0.23	0.13
RU_sv	-0.32	**-0.70**	0.27	0.26

in Table 4.3. In general, similar results are obtained as presented above. SM is in all regions the most important variable for explaining short-term dynamics in σ'_{dyn}. Over cropland and sparse vegetation, rainfall has a higher R^2 coefficient than temperature, whereas the opposite is true in grassland, needleleaf forest and shrubland. In all ROIs, the highest R^2 coefficients are obtained when combining temperature, SM and rainfall anomalies. In all regions except AT_cr, where the combined R^2 values are very similar, a clear drop in R^2 is observed when including only temperature and rainfall in the analysis. Overall, the highest R^2 values are obtained in RU_sv, with median values above 0.50 and maximum values around 0.70. Vegetation growth in this ROI is generally limited by temperature and radiation, not by SM availability. The fact that much higher correlations between σ'_{dyn} and SM than temperature are observed supports again the hypothesis that the short-term dynamics in σ'_{dyn} can be explained by SM dynamics to a very large extent. R^2 is lowest over needleleaf forest, indicating that there, the bare soil scattering component is largely attenuated by the canopy, and subsequently, the SM effect is lower.

4.6.3 Local slopes analysis

The local slopes σ'_{local} allow for the analysis of a potential SM effect at a much finer temporal scale. We selected two grid points as examples for the detailed study of a relationship between SM and short-term dynamics in σ'_{local} and σ'_{dyn}. Figure 4.8 shows σ'_{local} observed over a range of incidence angles, the 42-day smoothed σ'_{dyn} time series, and ERA5-Land SM, temporally matched to σ'_{local}, for a grid point in AT_cr (left) and PT_cr (right). Displayed are only σ'_{local} values from the incidence angle with most observations in the bins 25°-35°, 35°-45°, 45°-55° and 55°-65°, whereas the resulting 42-day smoothed σ'_{dyn} (shown in black) includes all observations from the entire incidence angle range. The shown time series are
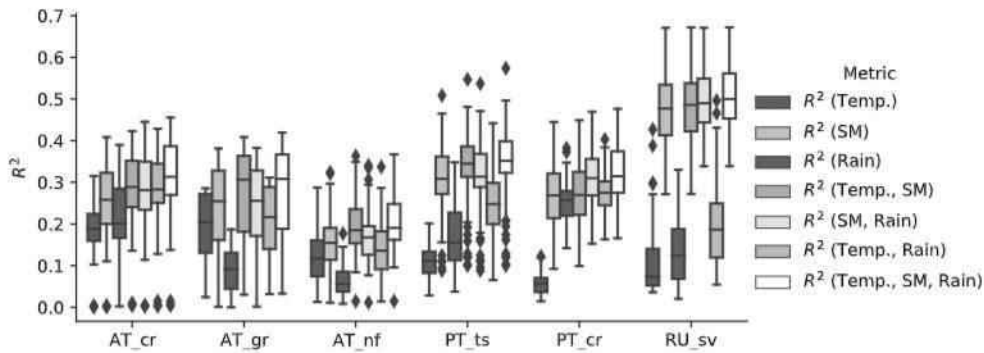
Fig. 4.7: Coefficient of determination (R^2) obtained for regressions of temperature, soil moisture, rainfall, and combinations thereof against σ'_{dyn}, for each ROI. The boxes show the quartiles, and the whiskers show the rest of the distribution. The horizontal line inside the boxes shows the median value. Outliers are shown by diamonds.

from 2014, as interesting SM and σ'_{dyn} dynamics occurred in this year in AT_cr and PT_cr.

In the first example (AT_cr), SM was relatively high in April and May 2014, and decreased relatively smoothly in June. In the beginning of July, SM increased again. As opposed to SM, σ'_{local} and the resulting σ'_{dyn} started to increase (become more shallow) in March, then decreased during the period of higher SM in April and May, increased in June, and quickly decreased at the beginning of July. From August onwards, SM stayed constantly high. σ'_{local} and σ'_{dyn} decreased, mainly reflecting the end of the growing season and senescence of the vegetation, but also including some short-term effects such as in October and the beginning of November, where again, the σ'_{local} and also σ'_{dyn} dynamics are clearly opposed to SM dynamics. In the second example (PT_cr), SM was high in the winter months in 2014, decreased from March onwards and increased again in September, interrupted by a number of SM increases and rapid decreases due to rainfall events. The distinct SM dynamics are also found in σ'_{local}: whenever SM increased, σ'_{local} decreased. The effect seems particularly pronounced at lower incidence angles, for example when comparing the $\sigma'_{\mathrm{local}}(\theta=35°)$ time series with $\sigma'_{\mathrm{local}}(\theta=58°)$. The time series also show the dependence on the overpass timing: the large rainfall event in mid-May is reflected in $\sigma'_{\mathrm{local}}(\theta=58°)$, but missed by $\sigma'_{\mathrm{local}}(\theta=35°)$. In σ'_{dyn}, the short-term effects that are so clearly visible in σ'_{local} appear smoothed, but can still be linked to large rainfall events for example in the beginning of April, the end of June and the beginning of September. Again, the seasonal dynamics are dominated by the vegetation cycle. These observations indicate that rainfall events and thus SM increases steepen σ'_{dyn}

Chapter 4 Analysis of short-term soil moisture effects on the ASCAT backscatter-incidence angle dependence
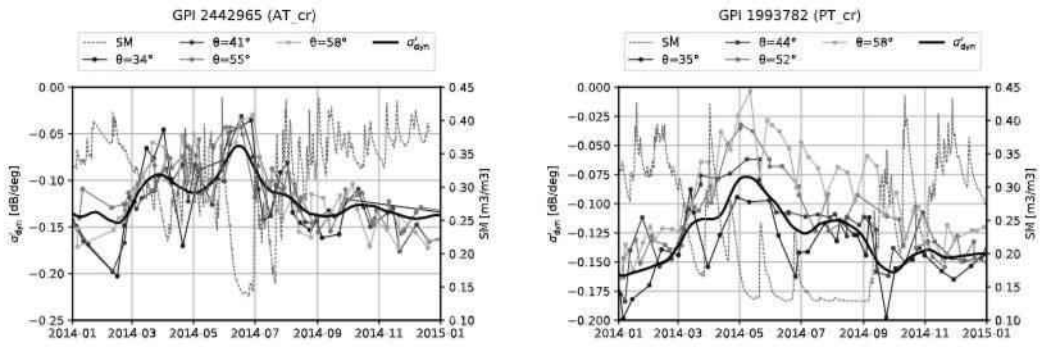
Fig. 4.8: Soil moisture (SM), σ'_{local} from the five most frequent incidence angles and σ'_{dyn} for a grid point in (left) AT_cr and (right) PT_cr.
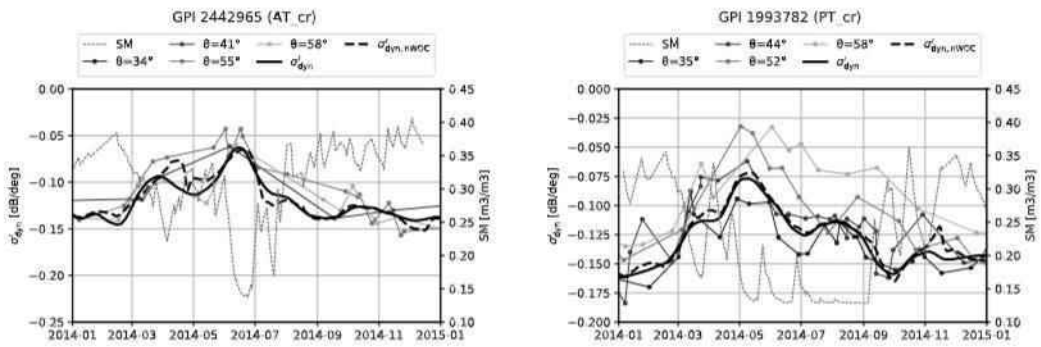
Fig. 4.9: Same as Figure 4.8, but without σ'_{local} from rainy days and morning overpasses, and the resulting $\sigma'_{\text{dyn,nWOC}}$ in addition (dashed black line) to the original σ'_{dyn}.

where a flattening is expected as a result of growing vegetation. Similarly, at the end of the growing season, the steepening of σ'_{dyn} is exacerbated by SM increases.

4.6.4 Indirect assessment of WOC effects on the ASCAT slope

In section 4.6.2, we showed that short-term σ'_{dyn} anomalies are highly correlated with SM and rainfall. However, rainfall has no direct effect on backscatter. Rather, it is SM and WOC after rainfall events (and, in the morning hours, WOC in the form of dew) that affect backscatter. Similar to SM, WOC might have an impact on σ'. However, due to a lack of reference data for WOC, we can currently assess contributions of WOC only indirectly. As described in section 4.5.4, we do this by removing measurements potentially affected by WOC before the σ'_{dyn} calculation. Figure 4.9 shows the remaining σ'_{local}, the original σ'_{dyn}, the new $\sigma'_{\text{dyn,nWOC}}$ with measurements from rainy days and morning overpasses removed, and SM, temporally matched to the dates of the remaining σ'_{local} values. Compared to Figure 4.8, the AT_cr example (left panel) shows a longer slope increase in spring, but again a decrease around the

beginning of May, when SM is high. In autumn, σ'_{dyn} and $\sigma'_{dyn,nWOC}$ are very similar. In the PT_cr example (right panel), the number of quick drops in the $\sigma'_{local}(\theta=58°)$ time series is reduced. Remaining short-term effects are mainly visible during the large SM increase around the beginning of April and at the beginning of July, when the vegetation is already beginning senescence. The resulting $\sigma'_{dyn,nWOC}$ dynamics are very similar to the original σ'_{dyn}. The reduced robustness of the calculation of $\sigma'_{dyn,nWOC}$ shows for example in November 2014.

This analysis shows that when excluding measurements from rainy days and morning overpasses, some short-term dynamics in σ'_{local} are indeed removed, which may be related to WOC. However, the main dynamics in σ' are still present, as the 42-day smoothed $\sigma'_{dyn,nWOC}$ does not differ much from σ'_{dyn}. This suggests that WOC might play a (significant) role, however, it represents only another influence on σ'_{dyn}, in addition to the SM effect.

To quantify the relative importance of the SM effect on σ'_{dyn} with respect to the WOC effect, we repeat the correlation analysis from section 4.6.2, now using $\sigma'_{dyn,nWOC}$ instead of σ'_{dyn}. Because of the only indirect effect on rainfall and the fact that we used rainfall to correct for WOC in $\sigma'_{dyn,nWOC}$, we omit this variable here. Table 4.4 shows the median Spearman correlations between anomalies of SM, temperature, and LAI and $\sigma'_{dyn,nWOC}$ (r). In addition, the differences between the absolute correlations calculated between the explanatory variables and $\sigma'_{dyn,nWOC}$ and the absolute correlations calculated between the explanatory variables and σ'_{dyn} (section 4.6.2, Table 4.3) are given ($\Delta abs(r)$). A boxplot of the correlations between anomalies of SM, σ'_{dyn}, and $\sigma'_{dyn,nWOC}$ is shown in Fig. 4.10. Both Table 4.4 and Fig. 4.10 show that for all ROIs, the correlations between $\sigma'_{dyn,nWOC}$ and SM are lower, but still significant, and higher than with temperature or LAI. The correlations are mainly reduced in ROIs with higher rainfalls, i.e., Austria and Russia, showing that masking observations from rainy days and morning overpasses effectively reduces the impact of WOC (and SM, to a certain extent). These results suggest that we need to find a way to also fully reduce the SM effect in $\sigma'_{dyn,nWOC}$ in order to obtain a σ'_{dyn} that mainly includes vegetation water content and structure effects.

4.6.5 Quantification of SM effects on the ASCAT slope

As the previous sections indicate that SM causes secondary, short-term dynamics in σ'_{dyn}, we will give an estimate of the magnitude of the effect. Please note that in this estimation, we assume that SM causes all short-term effects in σ'_{dyn}, neglecting other effects which are, e.g., related to the vegetation structure. We do not correct

Tab. 4.4: Median Spearman correlation (significant at p<0.01) between anomalies of $\sigma'_{\mathrm{dyn,nWOC}}$ and the given variable (r), and the difference to the correlations with σ'_{dyn} shown in Table 4.3 ($\Delta abs(r)$; calculated between absolute r values). The maximum absolute correlation is given in bold.

Region	Soil moisture		Temperature		LAI	
	r	$\Delta abs(r)$	r	$\Delta abs(r)$	r	$\Delta abs(r)$
AT_cr	**-0.36**	-0.16	0.28	-0.15	0.05	-0.02
AT_gr	**-0.24**	-0.27	0.19	-0.22	-0.08	-0.06
AT_nf	**-0.12**	-0.25	0.12	-0.23	0.10	0.00
PT_ts	**-0.45**	-0.07	0.27	-0.05	0.07	-0.03
PT_cr	**-0.42**	-0.03	0.18	-0.05	0.10	-0.03
RU_sv	**-0.46**	-0.24	0.21	-0.06	0.17	-0.09
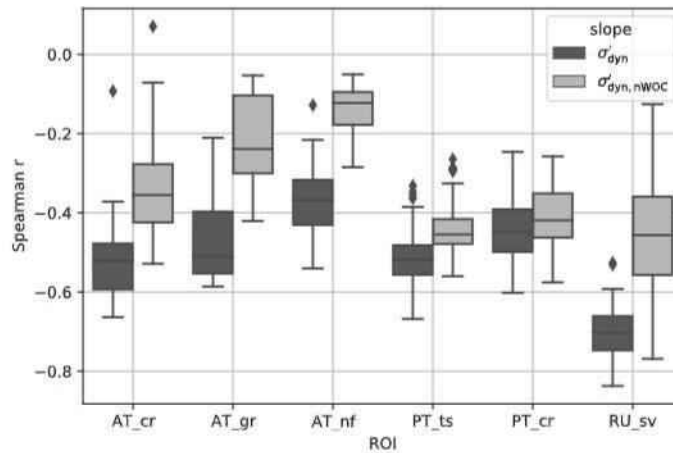
Fig. 4.10: Median Spearman correlation (significant at p<0.01) between anomalies of SM and σ'_{dyn} (red) and between anomalies of SM and $\sigma'_{\mathrm{dyn,nWOC}}$ (yellow). The boxes show the quartiles, and the whiskers show the rest of the distribution. The horizontal line inside the boxes shows the median value. Outliers are shown by diamonds.

for WOC here, as $\sigma'_{\mathrm{dyn,nWOC}}$ is less robust than σ'_{dyn}, and we do not have reference data for the actual presence and amount of WOC. The calculations are done for the maximum observed wet anomaly (i.e., 42-day smoothed SM anomalies) during the study period. The results should thus be interpreted as maximum values, and smaller SM effects are expected for most of the time. In order to quantify the SM effect, we calculate linear regressions between anomalies of 42-day smoothed SM and σ'_{dyn}. Figure 4.11 shows the median regression lines for each ROI along with values from a randomly selected subset of grid points. Boxplots of the linear regression slope (k) and R^2 values for the ROIs are shown in Figure 4.12. The k values are similar in most ROIs, and range from around -0.20 to -0.05 dB/deg per $\mathrm{m^3/m^3}$. AT_nf sticks out as the k values are slightly higher there, i.e., the regression line is flatter (median k=-0.08). The lowest median k are found in AT_gr and RU_sv (-0.14). Using k, the magnitude of the SM effect with respect to the seasonal cycle of σ'_{dyn} can be quantified: For example, in AT_cr, the largest positive (wet), 42-day smoothed SM anomaly from 2007-2019 was 0.10 $\mathrm{m^3/m^3}$ ($\mathrm{SM_{wet}}$). With a median k in AT_cr of -0.13 dB/deg per $\mathrm{m^3/m^3}$, $\mathrm{SM_{wet}}$ corresponds to an effect on σ'_{dyn} of -0.013 dB/deg. Typically, σ'_{dyn} ranges from -0.15 dB/deg to -0.06 dB/deg in cropland, i.e., over the year, the change in σ'_{dyn} is 0.09 dB/deg. The value of -0.013 dB/deg thus corresponds to $0.013/0.09 = 14.4\%$ of the average, total seasonal variation of σ'_{dyn}. Table 4.5 gives an overview of the median values for k and the 95% confidence interval (k_{min} and k_{max}), the maximum SM anomaly during 2007-2019, minimum and maximum σ'_{dyn}, the difference between maximum and minimum σ'_{dyn} ($\Delta\sigma'_{\mathrm{dyn}}$), and the thereof derived effect of the maximum wet anomaly on the slope, for each ROI. The SM effect is lowest, but still considerable, in AT_nf (6%). This is followed by grassland (AT_gr) with an effect of 11.2%. Over cropland (AT_cr and PT_cr), the effect is of 14.4% and 13.0%, respectively. The largest effects are observed over tree and shrub mosaic (PT_ts) and sparse vegetation (RU_sv), with 17.3% and 23.3%. The SM effect thus increases with decreasing vegetation density, as with sparser vegetation, the signal is more and more coming from the soil. As stated above, these numbers are expected to be lower during most of the time. Still, they indicate that σ'_{dyn} is not just related to vegetation dynamics but also notably affected by SM. The secondary short-term dynamics caused by SM may be as large as a fifth of the seasonal, vegetation-induced variation in σ'_{dyn}.
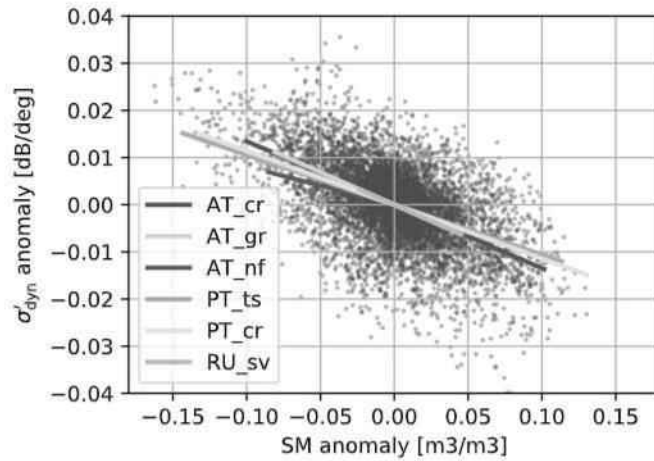
Fig. 4.11: Scatter plot of SM and σ'_{dyn} anomalies from randomly selected grid points for each ROI, along with the linear regression lines (calculated from all grid points of each ROI).
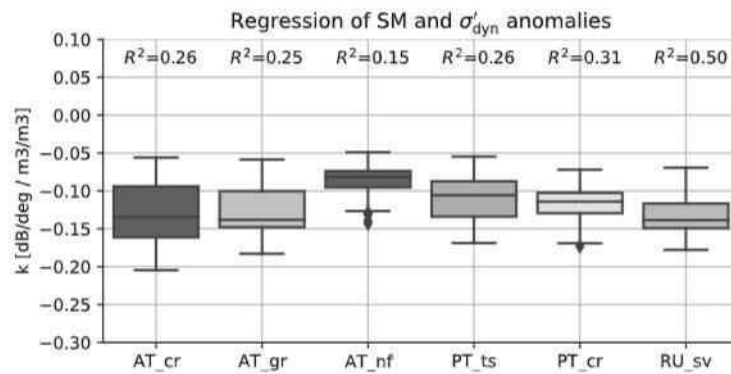
Fig. 4.12: Linear regression slope k of SM and σ'_{dyn} anomalies for each ROI. The boxes show the quartiles, and the whiskers show the rest of the distribution. The horizontal line inside the boxes shows the median value. Outliers are shown by diamonds. R^2 values of the linear regressions are shown above each box.

Tab. 4.5: Quantification of the SM effect on σ'_{dyn}. k is the median slope of the linear regression between anomalies in SM and σ'_{dyn}. 95% of k are within k_{min} and k_{max}. The largest positive SM anomaly, $\mathrm{SM_{wet}}$, is given in $\mathrm{m^3/m^3}$; $\sigma'_{\mathrm{dyn,min}}$, $\sigma'_{\mathrm{dyn,max}}$ and $\Delta\sigma'_{\mathrm{dyn}}$ are given in $\mathrm{dB/deg}$. The SM effect has been calculated based on the ROI-specific median values of all parameters.

ROI	k_{min}	k	k_{max}	$\mathrm{SM_{wet}}$	$\sigma'_{\mathrm{dyn,min}}$	$\sigma'_{\mathrm{dyn,max}}$	$\Delta\sigma'_{\mathrm{dyn}}$	Effect
AT_cr	-0.14	-0.13	-0.13	0.10	-0.15	-0.06	0.09	14.4%
AT_gr	-0.14	-0.14	-0.13	0.04	-0.12	-0.07	0.05	11.2%
AT_nf	-0.09	-0.08	-0.07	0.03	-0.10	-0.06	0.04	6.0%
PT_ts	-0.11	-0.11	-0.10	0.11	-0.15	-0.08	0.07	17.3%
PT_cr	-0.12	-0.11	-0.11	0.13	-0.17	-0.06	0.11	13.0%
RU_sv	-0.15	-0.14	-0.13	0.05	-0.17	-0.14	0.03	23.3%

4.7 Discussion

Backscatter measured by active microwave sensors is affected by multiple factors. Due to the coarse spatial resolution, each measurement usually contains signals from multiple land cover types. Moreover, rainfall, SM, temperature, and vegetation dynamics are closely related, which makes it especially difficult to separate the effects in the observed backscatter values. We tried to overcome these challenges by including different types of analyses, which all point to the same result: SM causes high-frequency variability in σ', which appears as a secondary effect on top of the dominant vegetation signal. The effect can be explained by an SM-induced increase of the backscatter coefficient over vegetation canopies that still allow a fraction of the radiation to penetrate through and reach the surface. As vegetation canopies are less transparent at high incidence angles due to longer paths through the canopy, observations from lower incidence angles are more affected than observations from higher incidence angles. Consequently, the slope of the backscatter-incidence angle dependence becomes steeper, even though the vegetation canopy did not change. The assumption that SM causes an equal increase of σ^0 (when expressed in dB) across all incidence angles is thus not strictly fulfilled. Rather, SM might increase σ^0 especially at low incidence angles and thus lead to a steeper σ', as displayed in red in Figure 4.1. We gave a rough magnitude estimate of the SM effect, showing that it can be as high as one fifth of the total seasonal variation in σ'_{dyn}. The separation of vegetation, SM, and WOC effects on σ'_{dyn} as well as their respective contributions should be investigated further using more complex approaches, e.g., empirical orthogonal function analysis.

Despite the clear results, we would like to discuss potential shortcomings of our analysis in the following.

We carried out all our analyses on full time series, i.e., covering all months from January to December, apart from a masking of days with temperatures below 3°C and snow cover. We did not do any seasonal split of the data because we were interested in the general presence of an SM effect. Single seasons might however show slightly different results. For example, we know of phenological processes such as spring reactivation in deciduous broadleaf forest that can impact σ' during a certain time of the year. These are neglected here, and it is assumed that all short-term effects have the same causes and appear throughout the year.

As a reference for vegetation dynamics, we use LAI in this study. However, LAI is a suitable, but not perfect reference for VOD, which σ' is most closely related to (Grant et al., 2016). For example, time lags have been observed between LAI and VOD

(Jones et al., 2011; El Hajj et al., 2019). These time lags are frequency-dependent and expected to be smaller for C-band (Grant et al., 2016; El Hajj et al., 2019). In the presented study, we tested the use of lagged correlations, but, as the time lags were small for all ROIs except for PT_cr and did not affect the results and conclusions of the study, they were omitted. Another way to overcome this problem might be to compare σ' to VOD derived from passive microwave sensors, which are expected to be less susceptible to SM effects because passive retrievals of SM and VOD make less strong pre-assumptions. However, also passive retrievals of VOD are associated with uncertainties, for example, due to radio frequency interference and pixel heterogeneity (Li et al., 2021; Bousquet et al., 2021).

The impact of WOC on total backscatter and the relative contributions of the various scattering mechanisms are still poorly understood. Without reference data on how the presence of WOC alters the sensitivity to surface SM, it is difficult to disentangle the respective impacts on the backscatter return. It is however expected that WOC leads to increased backscatter, while at the same time reducing the sensitivity to surface SM. The WOC filtering applied in this study can thus not be used to identify WOC directly, but should be interpreted as a method to mask events where both WOC as well as an increase in SM lead to secondary effects on σ'_{dyn} that do not originate from vegetation dynamics. Note that the examples discussed in sections 4.6.3 and 4.6.4 had a rather low number of rainfall events in 2014. In regions and years with more frequent rainfall events, removing WOC-affected measurements drastically reduces the number of σ'_{local}, leading to highly unstable σ'_{dyn} estimates in some cases. The effective removal of WOC and SM effects for the estimation of σ'_{dyn} will thus require very thorough investigation.

In the operational TU Wien SM retrieval algorithm, the estimation of the seasonal vegetation cycle is based on observations from several years and thus, short-term effects of SM become irrelevant. This explains the good performance of the operational ASCAT SM product as shown in many studies (Al-Yaari et al., 2014; Pierdicca et al., 2015; Miyaoka et al., 2017; Chen et al., 2018; Mousa et al., 2020; Hahn et al., 2020). Our findings provide an explanation for studies (Pfeil et al., 2018; Steele-Dunne et al., 2021) that did not find an improvement in the accuracy of SM datasets when retrieving them with vc_{dyn} instead of vc_{clim}. In order to benefit from an ASCAT-derived vc_{dyn} in the SM retrieval and in studies of vegetation dynamics, all SM effects must first be corrected in the signal. A solution might be the application of a suitable temporal smoothing on σ' in order to reduce SM effects in the signal while still keeping interannual vegetation dynamics. Other approaches could be the masking of observations taken under wet conditions, such as applied for WOC in this

study, or by the use of models that explicitly account for the effect of soil moisture on σ'.

4.8 Conclusions

In this study, we revisited the assumption that soil moisture has a negligible effect on the slope σ' of the backscatter-incidence angle dependence. Based on this assumption, σ' has been used in studies of vegetation dynamics, for the retrieval of VOD, and to model the vegetation component in the backscatter signal. However, recent studies indicated that a soil moisture contribution may be present in the slope of the backscatter-incidence angle dependence. We analyzed this potential soil moisture effect on σ' by comparing σ', rainfall, soil moisture, temperature, and leaf area index time series over six study regions with different climate, land cover, and vegetation cycles. The obtained results lead us to the following conclusions:

- The slope of the backscatter-incidence angle dependence is dominated by the vegetation cycle, but is affected by soil moisture at short temporal scales. This SM effect can be larger than 20% of the seasonal, vegetation-induced variation over sparse vegetation. Over dense vegetation, the observed effect is lower (6% in evergreen needleleaf forest).

- Short-term secondary effects are mitigated when using a climatology slope (σ'_{clim}) due to long-term averaging. The use of σ'_{clim} is however only suitable for applications that do not look at interannual vegetation dynamics.

- As the slope has been found to be a useful complement to optical datasets for vegetation studies (Petchiappan et al., 2021), short-term secondary effects should be further investigated and a robust method for their mitigation should be developed.

The findings from this study advance the understanding of vegetation and soil moisture effects on active microwave observations. The study also showed that there is a need to better understand interactions between C-band microwaves and water on canopy, i.e., how water on canopy alters σ^0 and σ', and how it affects the sensitivity to soil moisture.

Author contributions

Conceptualization, I.P. and W.W.; methodology, I.P., W.W., M.V., S.H., S.S.-D., R.Q.; investigation, I.P.; visualization, I.P.; writing—original draft preparation, I.P.; writing—review and editing, all authors. All authors have read and agreed to the published version of the manuscript.

Funding

Declarations of interest

None.

Acknowledgements

Conclusions 5

> *Dragonfly out in the sun you know what I mean, don't you know? (Feeling good)*
>
> — **Nina Simone**
> (American singer, songwriter, pianist, and civil rights activist)

5.1 Conclusions and scientific impact

Active microwave remote sensing observations, and in particular ASCAT with its unique viewing geometry, contain highly valuable information for a wide range of applications. However, interpreting the observations is complex due to a sensitivity to a number of interrelated variables, including SM and vegetation dynamics. Over land, the focus of the research field has long been mainly on SM retrievals. In the last few years, ASCAT observations have been increasingly used for the study of vegetation dynamics. Subsequently, the understanding of the influence of vegetation water content and structure on ASCAT observations has improved considerably (Vreugdenhil et al., 2016; Vreugdenhil et al., 2017; Steele-Dunne et al., 2019; Petchiappan et al., 2021). The studies conducted in the framework of this thesis contribute to these developments.

The overall aim of the thesis was to advance the understanding of how SM and vegetation dynamics affect ASCAT $\sigma^°$ and σ', i.e., the dependence of $\sigma^°$ on the incidence angle of an observation. The conducted research highlighted the great potential of the coarse-scale ASCAT sensor for the retrieval of biogeophysical variables such as SM and vegetation dynamics. It also revealed new aspects that need to be taken into account when interpreting ASCAT observations.

The first study showed that the TU Wien SM retrieval algorithm benefits from a stronger vegetation correction over a temperate climate agricultural region, as seasonal biases of ASCAT SM compared to in situ SM are thus reduced. The results

of this study led to a global analysis of the optimal vegetation parameterization in the TUW SM retrieval algorithm (Hahn et al., 2020).

The second study investigated a period of a relatively weak incidence angle dependence, i.e., shallow σ', in spring. The effect could be linked to water uptake and leaf emergence in deciduous forests, showing that changes in a canopy structure can have discernable effects on ASCAT observations, even if the responsible vegetation type makes up only a small fraction of the entire footprint. This study confirmed the peculiar backscatter signal of deciduous forests that has been described and exploited previously, e.g. in the context of forest type classification (Dostálová et al., 2018). Moreover, it showed that backscatter observations provide valuable information about coarse-scale canopy status and development, complementing information provided by optical sensors, with the advantage of a high temporal resolution.

Finally, the third study showed that despite the clear and dominant control of σ' by vegetation dynamics, there are short-term secondary effects in σ' which need to be taken into account when interpreting σ' time series. As shown in the study, SM can lead to dynamics in the order of 20% of the total seasonal σ' variation over sparse vegetation. Over forests, where the signal is strongly attenuated by the canopy, SM does not have such a large effect on σ'. These findings are valuable when using the backscatter-incidence angle dependence for vegetation studies, as well as for the TU Wien SM retrieval algorithm, which currently uses long-term average σ' instead of σ' time series to model the seasonal vegetation cycle. Short-term SM effects are thus averaged out to a large extent.

The findings of the three studies are of high interest each by themselves, and, depending on the perspective of a reader, provide new insights for the retrieval and study of both SM and vegetation dynamics. Taken together, the studies fulfill the aim of advancing the general understanding of ASCAT $\sigma°$, its dependence on the incidence angle, and the numerous variables and processes that play a role in this relationship. The thesis also showed how unexpected findings, such as the "spring peaks" that could not be explained in the first study (Chapter 2), can open up new opportunities – in this case, the observation of spring reactivation in deciduous broadleaf forest across large regions. In addition to their respective hypotheses and own findings, the second and third study allowed for a reassessment and reinterpretation of the results of the preceding studies. Seasonal biases in ASCAT SM time series (Chapter 2) are most certainly also caused by the fact that the applied vegetation correction is not purely representative of vegetation dynamics, but still contains a non-negligible SM signal. In addition, it is likely that structural effects, such as the scattering from twigs and branches with high water content

shortly before leaf emergence (Chapter 3), temporarily reduce the sensitivity to SM considerably, perhaps leading to over- or underestimations in the TU Wien SM retrieval algorithm. These effects are partly, but probably not fully, corrected by the applied vegetation correction. Structural effects are not limited to deciduous broadleaf forests: For example, changes in the structure of certain crop types, e.g., the bending of barley heads (Vreugdenhil et al., 2018; Pfeil et al., 2020a), may affect ASCAT observations. The transition period from winter to spring is especially complex, as a number of natural processes occur at the same time, all of which affect ASCAT observations. These processes include snow melt, increasing vegetation water content, drying of soils due to both rising temperatures, i.e., increased evapotranspiration, and vegetation water uptake, and vegetation growth, i.e., biomass accumulation. Moreover, non-natural processes such as the ploughing of fields in early spring across large areas may have quantifiable effects on the signal. Future studies of ASCAT $\sigma°$ and its dependence on the incidence angle should be set up as broad as possible in order to take into account such combined effects that might cancel each other out or reinforce each other. Nonetheless, there will always be a need to study selected processes in detail in order to understand each component that contributes to the signal.

5.2 Outlook and future research

In addition to several findings, the conducted research studies led to new, unanswered questions and highlighted areas that still require a deeper look.

The detailed study of deciduous broadleaf forest $\sigma°$ and σ' showed the complexity of this ecosystem type. Several different scattering mechanisms are activated depending on the structure of the trees, e.g., if leaves are present or not, and depending on their water content. The shape of the "spring peaks" in σ' should be investigated in more detail, especially with respect to the combined effects of deciduous forest scattering and secondary short-term SM effects on σ'. Deciduous trees take up considerable amounts of water in spring time (Young-Robertson et al., 2016), and thus, the spring peaks might as well be the result of a combined effect of lower SM and strong scattering by twigs and branches. Here, different manifestations are expected depending on the climate, i.e., whether the deciduous forests are located in arid, temperate or boreal regions, where even deep soil layers and trees freeze during winter.

In the third study, we masked observations potentially affected by water on the canopy (WOC; morning dew or intercepted rainfall), as the effect that WOC has on $\sigma°$ and σ' is poorly understood. Especially in regions with frequent rainfalls, the effect might be substantial. However, by masking all affected observations, many observations for calculating a robust σ' are lost. Thus, quantifying the magnitude of the WOC effect, similarly as done for SM in the third study, would be highly valuable.

The presence of secondary SM effects in σ' needs to be taken into account in future studies that use σ' time series. This is especially critical in studies that investigate water-vegetation interaction processes and disturbances thereof (e.g., droughts), over land cover types which allow a certain soil (moisture) contribution on the signal.

The findings of this thesis explain influences of SM and vegetation on ASCAT $\sigma°$ and σ'. Influences on the second-order term of the backscatter-incidence angle relationship, the curvature σ'', were not studied. However, recent studies showed that also σ'' contains valuable information, for example related to photosynthetic activity in evergreen forests and savannah ecosystems (Petchiappan et al., 2021) and drought impacts on grasslands (Steele-Dunne et al., 2019). Despite the reduced robustness of σ'' estimations compared to σ', σ'' should be considered in future studies.

The launch of the first Metop-SG ("second generation") satellite is planned for mid-2020. It will provide an extension to the observations obtained by the scatterometers on board the ERS-1 and -2 satellites as well as by the ASCAT sensors on board Metop-A, -B and -C, and thus ensure the availability of long backscatter time series of more than 40 years. In addition, Metop-SG will carry a scatterometer with not only VV but also VH and HH polarization modes, opening up new opportunities for the study of (C-band) scattering effects over land.

Along with many other studies, this thesis confirmed the great value of coarse-scale radar observations. However, a great potential certainly lies in the combination of coarse-scale with fine-scale observations, for example provided by the Sentinel-1 satellites, in order to obtain information about ecosystem processes occurring on local to regional spatial scales and on short to long temporal scales.

Bibliography

Al Bitar, A., A. Mialon, Y. H. Kerr, F. Cabot, P. Richaume, E. Jacquette, A. Quesney, A. Mahmoodi, S. Tarot, M. Parrens, A. Al-Yaari, T. Pellarin, N. Rodriguez-Fernandez, and J.-P. Wigneron (2017). "The global SMOS Level 3 daily soil moisture and brightness temperature maps". In: *Earth System Science Data* 9.1, pp. 293–315 (cit. on p. 76).

Albergel, C, C Rüdiger, D Carrer, J-C Calvet, N Fritz, V Naeimi, Z Bartalis, and S Hasenauer (2009). "An evaluation of ASCAT surface soil moisture products with in-situ observations in Southwestern France". In: *Hydrology and Earth System Sciences* 13.2, pp. 115–124 (cit. on p. 15).

Albergel, Clément, Christoph Rüdiger, Thierry Pellarin, Jean-Christophe Calvet, Noureddine Fritz, Francis Froissard, David Suquia, Alain Petitpa, Bruno Piguet, and Eric Martin (2008). "From near-surface to root-zone soil moisture using an exponential filter: an assessment of the method based on in-situ observations and model simulations". In: *Hydrology and Earth System Sciences Discussions* 12, pp. 1323–1337 (cit. on p. 23).

Anoop, Sampelli, Devesh Kumar Maurya, PVN Rao, and M Sekhar (2017). "Validation and Comparison of LPRM Retrieved Soil Moisture Using AMSR2 Brightness Temperature at Two Spatial Resolutions in the Indian Region". In: *IEEE Geoscience and Remote Sensing Letters* 14.9, pp. 1561–1564 (cit. on p. 21).

Barbu, AL, J-C Calvet, J-F Mahfouf, and S Lafont (2014). "Integrating ASCAT surface soil moisture and GEOV1 leaf area index into the SURFEX modelling platform: a land data assimilation application over France". In: *Hydrology and Earth System Sciences* 18.1, pp. 173–192 (cit. on pp. 15, 34).

Bartalis, Zoltan, Wolfgang Wagner, Vahid Naeimi, Stefan Hasenauer, Klaus Scipal, Hans Bonekamp, Julia Figa, and Craig Anderson (2007). "Initial soil moisture retrievals from the METOP-A Advanced Scatterometer (ASCAT)". In: *Geophysical Research Letters* 34.20 (cit. on p. 23).

Basler, David and Christian Körner (2014). "Photoperiod and temperature responses of bud swelling and bud burst in four temperate forest tree species". In: *Tree physiology* 34.4, pp. 377–388 (cit. on p. 45).

Bauer-Marschallinger, Bernhard, Vahid Freeman, Senmao Cao, Christoph Paulik, Stefan Schaufler, Tobias Stachl, Sara Modanesi, Christian Massari, Luca Ciabatta, Luca Brocca, et al. (2018). "Toward global soil moisture monitoring with Sentinel-1: Harnessing assets and overcoming obstacles". In: *IEEE Transactions on Geoscience and Remote Sensing* 57.1, pp. 520–539 (cit. on p. 76).

Beurs, Kirsten M de and Geoffrey M Henebry (2010). "Spatio-temporal statistical methods for modelling land surface phenology". In: *Phenological research*. Springer, pp. 177–208 (cit. on p. 42).

Bircher, Simone, Niels Skou, Karsten Høgh Jensen, Jeffrey P Walker, and Lars Rasmussen (2012). "A soil moisture and temperature network for SMOS validation in Western Denmark". In: *Hydrology and Earth System Sciences* 16.5, pp. 1445–1463 (cit. on p. 34).

Blöschl, Günter, AP Blaschke, M Broer, C Bucher, G Carr, X Chen, A Eder, M Exner-Kittridge, A Farnleitner, A Flores-Orozco, et al. (2016). "The Hydrological Open Air laboratory (HOAL) in Petzenkirchen: a hypothesis-driven observatory". In: *Hydrology and Earth System Sciences* 20.1, p. 227 (cit. on p. 16).

Bonan, Gordon B (2008). "Forests and climate change: forcings, feedbacks, and the climate benefits of forests". In: *science* 320.5882, pp. 1444–1449 (cit. on p. 42).

Bontemps, S, M Herold, L Kooistra, A Van Groenestijn, A Hartley, O Arino, I Moreau, and P Defourny (2012). "Revisiting land cover observation to address the needs of the climate modeling community". In: *Biogeosciences* 9, pp. 2145–2157 (cit. on pp. 44, 47).

Bontemps, S, P Defourny, J Radoux, E Van Bogaert, C Lamarche, F Achard, P Mayaux, M Boettcher, C Brockmann, G Kirches, et al. (2013). "Consistent global land cover maps for climate modelling communities: current achievements of the ESA's land cover CCI". In: *Proceedings of the ESA Living Planet Symposium, Edimburgh*, pp. 9–13 (cit. on pp. 16, 22).

Bousquet, Emma, Arnaud Mialon, Nemesio Rodriguez-Fernandez, Catherine Prigent, Fabien H. Wagner, and Yann H. Kerr (2021). "Influence of surface water variations on VOD and biomass estimates from passive microwave sensors". In: *Remote Sensing of Environment* 257, p. 112345 (cit. on pp. 76, 101).

Brocca, L, F Melone, T Moramarco, W Wagner, V Naeimi, Z Bartalis, and S Hasenauer (2010). "Improving runoff prediction through the assimilation of the ASCAT soil moisture product". In: *Hydrology and Earth System Sciences* 14.10, pp. 1881–1893 (cit. on p. 14).

Brocca, L, S Hasenauer, T Lacava, F Melone, T Moramarco, W Wagner, W Dorigo, P Matgen, J Martínez-Fernández, P Llorens, et al. (2011). "Soil moisture estimation through ASCAT and AMSR-E sensors: An intercomparison and validation study across Europe". In: *Remote Sensing of Environment* 115.12, pp. 3390–3408 (cit. on p. 15).

Brocca, Luca, Christian Massari, Luca Ciabatta, Tommaso Moramarco, Daniele Penna, Giulia Zuecco, Luisa Pianezzola, Marco Borga, Patrick Matgen, and José Martínez-Fernández (2015). "Rainfall estimation from in situ soil moisture observations at several sites in Europe: an evaluation of the SM2RAIN algorithm". In: *Journal of Hydrology and Hydromechanics* 63.3, pp. 201–209 (cit. on p. 14).

Brocca, Luca, Wade T Crow, Luca Ciabatta, Christian Massari, Patricia De Rosnay, Markus Enenkel, Sebastian Hahn, Giriraj Amarnath, Stefania Camici, Angelica Tarpanelli, et al. (2017). "A review of the applications of ASCAT soil moisture products". In: *IEEE Journal of Selected Topics in Applied Earth Observations and Remote Sensing* 10.5, pp. 2285–2306 (cit. on p. 76).

Brunfeldt, David R and Fawwaz T Ulaby (1984). "Measured microwave emission and scattering in vegetation canopies". In: *IEEE Transactions on Geoscience and Remote Sensing* 6, pp. 520–524 (cit. on p. 65).

Buermann, Wolfgang, Matthias Forkel, Michael O'Sullivan, Stephen Sitch, Pierre Friedling-stein, Vanessa Haverd, Atul K Jain, Etsushi Kato, Markus Kautz, Sebastian Lienert, et al. (2018). "Widespread seasonal compensation effects of spring warming on northern plant productivity". In: *Nature* 562.7725, pp. 110–114 (cit. on p. 42).

Camacho, Fernando, Jesús Cernicharo, Roselyne Lacaze, Frédéric Baret, and Marie Weiss (2013). "GEOV1: LAI, FAPAR essential climate variables and FCOVER global time series capitalizing over existing products. Part 2: Validation and intercomparison with reference products". In: *Remote Sensing of Environment* 137, pp. 310–329 (cit. on p. 83).

Chan, S, R Hunt, R Bindlish, E Njoku, J Kimball, and T Jackson (2013). "Ancillary Data Report for Vegetation Water Content". In: *SMAP Project Document* (cit. on p. 22).

Chan, Steven K, Rajat Bindlish, Peggy E O'Neill, Eni Njoku, Tom Jackson, Andreas Colliander, Fan Chen, Mariko Burgin, Scott Dunbar, Jeffrey Piepmeier, et al. (2016). "Assessment of the SMAP passive soil moisture product". In: *IEEE Transactions on Geoscience and Remote Sensing* 54.8, pp. 4994–5007 (cit. on p. 22).

Chan, Steven K, Rajat Bindlish, Peggy O'Neill, Thomas Jackson, Eni Njoku, Scott Dunbar, Julian Chaubell, Jeffrey Piepmeier, Simon Yueh, Dara Entekhabi, et al. (2018). "Development and assessment of the SMAP enhanced passive soil moisture product". In: *Remote Sensing of Environment* 204, pp. 931–941 (cit. on p. 76).

Chen, Fan, Wade T Crow, Rajat Bindlish, Andreas Colliander, Mariko S Burgin, Jun Asanuma, and Kentaro Aida (2018). "Global-scale evaluation of SMAP, SMOS and ASCAT soil moisture products using triple collocation". In: *Remote Sensing of Environment* 214, pp. 1–13 (cit. on p. 101).

Cho, Eunsang, Chun-Hsu Su, Dongryeol Ryu, Hyunglok Kim, and Minha Choi (2017). "Does AMSR2 produce better soil moisture retrievals than AMSR-E over Australia?" In: *Remote sensing of environment* 188, pp. 95–105 (cit. on p. 21).

Chuine, Isabelle (2000). "A unified model for budburst of trees". In: *Journal of theoretical biology* 207.3, pp. 337–347 (cit. on p. 45).

Colliander, Andreas, TJ Jackson, Rajat Bindlish, S Chan, N Das, SB Kim, MH Cosh, RS Dunbar, L Dang, L Pashaian, et al. (2017). "Validation of SMAP surface soil moisture products with core validation sites". In: *Remote Sensing of Environment* 191, pp. 215–231 (cit. on p. 22).

Cui, Chenyang, Jia Xu, Jiangyuan Zeng, Kun-Shan Chen, Xiaojing Bai, Hui Lu, Quan Chen, and Tianjie Zhao (2017). "Soil moisture mapping from satellites: An intercomparison of SMAP, SMOS, FY3B, AMSR2, and ESA CCI over two dense network regions at different spatial scales". In: *Remote Sensing* 10.1, p. 33 (cit. on pp. 21, 22).

Dierckx, Wouter, Sindy Sterckx, Iskander Benhadj, Stefan Livens, Geert Duhoux, Tanja Van Achteren, Michael Francois, Karim Mellab, and Gilbert Saint (2014). "PROBA-V mission for global vegetation monitoring: standard products and image quality". In: *International Journal of Remote Sensing* 35.7, pp. 2589–2614 (cit. on pp. 22, 49, 83).

Dorigo, Wouter, Wolfgang Wagner, Clement Albergel, Franziska Albrecht, Gianpaolo Bal-samo, Luca Brocca, Daniel Chung, Martin Ertl, Matthias Forkel, Alexander Gruber, et al. (2017). "ESA CCI Soil Moisture for improved Earth system understanding: State-of-the art and future directions". In: *Remote Sensing of Environment* 203, pp. 185–215 (cit. on p. 76).

Dostálová, Alena, Wolfgang Wagner, Milutin Milenković, and Markus Hollaus (2018). "Annual seasonality in Sentinel-1 signal for forest mapping and forest type classification". In: *International journal of remote sensing* 39.21, pp. 7738–7760 (cit. on pp. 45, 63, 106).

El Hajj, Mohammad, Nicolas Baghdadi, Jean-Pierre Wigneron, Mehrez Zribi, Clément Albergel, Jean-Christophe Calvet, and Ibrahim Fayad (2019). "First vegetation optical depth mapping from Sentinel-1 C-band SAR data over crop fields". In: *Remote Sensing* 11.23, p. 2769 (cit. on p. 101).

Entekhabi, Dara, Eni G Njoku, Peggy E O'Neill, Kent H Kellogg, Wade T Crow, Wendy N Edelstein, Jared K Entin, Shawn D Goodman, Thomas J Jackson, Joel Johnson, et al. (2010). "The soil moisture active passive (SMAP) mission". In: *Proceedings of the IEEE* 98.5, pp. 704–716 (cit. on pp. 14, 21, 23).

ESA (2017). "Land Cover CCI Product User Guide Version 2. Tech. Rep. (2017)". In: Available at: `maps.elie.ucl.ac.be/CCI/viewer/download/ESACCI-LC-Ph2-PUGv2_2.0.pdf` (cit. on p. 84).

Essiamah, Sam and Walter Eschrich (1985). "Changes of starch content in the storage tissues of deciduous trees during winter and spring". In: *IAWA Journal* 6.2, pp. 97–106 (cit. on p. 45).

– (1986). "Water uptake in deciduous trees during winter and the role of conducting tissues in spring reactivation". In: *IAWA Journal* 7.1, pp. 31–38 (cit. on p. 45).

Ewers, Frank W, Thierry Améglio, Hervé Cochard, François Beaujard, Michel Martignac, Marc Vandame, Christian Bodet, and Pierre Cruiziat (2001). "Seasonal variation in xylem pressure of walnut trees: root and stem pressures". In: *Tree physiology* 21.15, pp. 1123–1132 (cit. on p. 45).

Finn, G.A., A.E. Straszewski, and V. Peterson (2007). "A general growth stage key for describing trees and woody plants". In: *Annals of Applied Biology* 151.1, pp. 127–131 (cit. on p. 48).

Forkel, Matthias, Mirco Migliavacca, Kirsten Thonicke, Markus Reichstein, Sibyll Schaphoff, Ulrich Weber, and Nuno Carvalhais (2015). "Codominant water control on global interannual variability and trends in land surface phenology and greenness". In: *Global change biology* 21.9, pp. 3414–3435 (cit. on p. 42).

Frappart, Frédéric, Jean-Pierre Wigneron, Xiaojun Li, Xiangzhuo Liu, Amen Al-Yaari, Lei Fan, Mengjia Wang, Christophe Moisy, Erwan Le Masson, Zacharie Aoulad Lafkih, et al. (2020). "Global monitoring of the vegetation dynamics from the Vegetation Optical Depth (VOD): A review". In: *Remote Sensing* 12.18, p. 2915 (cit. on p. 76).

Fromm, Jörg and Walter Eschrich (1986). "Changes of adenine nucleotide and orthophosphate concentrations in buds of deciduous trees during spring reactivation". In: *Trees* 1.1, pp. 42–46 (cit. on p. 45).

Fu, Yongshuo H, Xuan Zhang, Shilong Piao, Fanghua Hao, Xiaojun Geng, Yann Vitasse, Constantin Zohner, Josep Peñuelas, and Ivan A Janssens (2019). "Daylength helps temperate deciduous trees to leaf-out at the optimal time". In: *Global change biology* (cit. on p. 53).

Fung, Adrian K, Zongqian Li, and Kun-Shan Chen (1992). "Backscattering from a randomly rough dielectric surface". In: *IEEE Transactions on Geoscience and remote sensing* 30.2, pp. 356–369 (cit. on p. 65).

Gallinat, Amanda S, Richard B Primack, and David L Wagner (2015). "Autumn, the neglected season in climate change research". In: *Trends in ecology & evolution* 30.3, pp. 169–176 (cit. on p. 66).

geoland.at (2020). *Digitales Geländemodell (DGM) Österreich*. https://www.data.gv.at/katalog/dataset/d88a1246-9684-480b-a480-ff63286b35b7 (cit. on p. 46).

Gill, Allison L, Amanda S Gallinat, Rebecca Sanders-DeMott, Angela J Rigden, Daniel J Short Gianotti, Joshua A Mantooth, and Pamela H Templer (2015). "Changes in autumn senescence in northern hemisphere deciduous trees: a meta-analysis of autumn phenology studies". In: *Annals of Botany* 116.6, pp. 875–888 (cit. on p. 66).

Grant, JP, J-P Wigneron, RAM De Jeu, Heather Lawrence, Arnaud Mialon, Philippe Richaume, Ahmad Al Bitar, Matthias Drusch, MJE Van Marle, and Yann Kerr (2016). "Comparison of SMOS and AMSR-E vegetation optical depth to four MODIS-based vegetation indices". In: *Remote Sensing of Environment* 172, pp. 87–100 (cit. on pp. 100, 101).

Gruhier, Claire, Patricia De Rosnay, Stefan Hasenauer, Thomas Holmes, Richard De Jeu, Yann Kerr, Eric Mougin, Eni Njoku, Frank Timouk, Wolfgang Wagner, et al. (2010). "Soil moisture active and passive microwave products: intercomparison and evaluation over a Sahelian site". In: *Hydrology and Earth System Sciences* 14.1, pp. 141–156 (cit. on p. 15).

H SAF (2018). *Metop ASCAT Surface Soil Moisture Climate Data Record CDR2017 time series 12.5 km sampling (H113)*. http://dx.doi.org/10.15770/EUM_SAF_H_0004. EUMETSAT SAF on Support to Operational Hydrology and Water Management (cit. on p. 48).

H SAF ATBD (2018). *Algorithm Theoretical Baseline Document (ATBD) Metop ASCAT Soil Moisture CDR and offline products*. v0.7 (cit. on p. 48).

Hahn, Sebastian, Christoph Reimer, Mariette Vreugdenhil, Thomas Melzer, and Wolfgang Wagner (2017). "Dynamic characterization of the incidence angle dependence of backscatter using metop ASCAT". In: *IEEE Journal of Selected Topics in Applied Earth Observations and Remote Sensing* 10.5, pp. 2348–2359 (cit. on pp. 3–5, 15, 18, 21, 23, 43, 46, 48, 82).

Hahn, Sebastian, Wolfgang Wagner, Susan C Steele-Dunne, Mariette Vreugdenhil, and Thomas Melzer (2020). "Improving ASCAT Soil Moisture Retrievals With an Enhanced Spatially Variable Vegetation Parameterization". In: *IEEE Transactions on Geoscience and Remote Sensing* (cit. on pp. 4, 77, 101, 106).

Han, E, WT Crow, TR Holmes, and JD Bolten (2012). "Relative Skills of Soil Moisutre and Vegetation Optical Depth Retrievals for Agricultural Drought Monitoring". In: *AGU Fall Meeting Abstracts* (cit. on p. 21).

Hao, Guang-You, James K. Wheeler, N. Michele Holbrook, and Guillermo Goldstein (2013). "Investigating xylem embolism formation, refilling and water storage in tree trunks using frequency domain reflectometry". In: *Journal of Experimental Botany* 64.8, pp. 2321–2332 (cit. on p. 45).

Hao, Zengchao and Amir AghaKouchak (2014). "A nonparametric multivariate multi-index drought monitoring framework". In: *Journal of Hydrometeorology* 15.1, pp. 89–101 (cit. on p. 14).

Helman, David (2018). "Land surface phenology: What do we really 'see' from space?" In: *Science of The Total Environment* 618, pp. 665–673 (cit. on pp. 42, 66).

Hiebl, Johann and Christoph Frei (2016). "Daily temperature grids for Austria since 1961—concept, creation and applicability". In: *Theoretical and Applied Climatology* 124.1, pp. 161–178 (cit. on p. 50).

Jensen, Karsten H and Tissa H Illangasekare (2011). "HOBE: A hydrological observatory". In: *Vadose Zone Journal* 10.1, pp. 1–7 (cit. on p. 34).

Jiang, Lingmei, Jiancheng Shi, Saibun Tjuatja, Jeff Dozier, Kunshan Chen, and Lixin Zhang (2007). "A parameterized multiple-scattering model for microwave emission from dry snow". In: *Remote Sensing of Environment* 111.2-3, pp. 357–366 (cit. on p. 65).

Jones, Hamlyn G and Robin A Vaughan (2010). *Remote sensing of vegetation: principles, techniques, and applications*. Oxford university press (cit. on p. 43).

Jones, Matthew O, Lucas A Jones, John S Kimball, and Kyle C McDonald (2011). "Satellite passive microwave remote sensing for monitoring global land surface phenology". In: *Remote Sensing of Environment* 115.4, pp. 1102–1114 (cit. on pp. 30, 32, 42, 90, 101).

Jones, Matthew O, John S Kimball, and Lucas A Jones (2013). "Satellite microwave detection of boreal forest recovery from the extreme 2004 wildfires in Alaska and Canada". In: *Global change biology* 19.10, pp. 3111–3122 (cit. on p. 30).

Jones, Matthew O, John S Kimball, Lucas A Jones, and Kyle C McDonald (2012). "Satellite passive microwave detection of North America start of season". In: *Remote Sensing of Environment* 123, pp. 324–333 (cit. on p. 32).

Karthikeyan, L., Ila Chawla, and Ashok K. Mishra (2020). "A review of remote sensing applications in agriculture for food security: Crop growth and yield, irrigation, and crop losses". In: *Journal of Hydrology* 586, p. 124905 (cit. on p. 76).

Kern, Anikó, Hrvoje Marjanović, and Zoltán Barcza (2020). "Spring vegetation green-up dynamics in Central Europe based on 20-year long MODIS NDVI data". In: *Agricultural and Forest Meteorology* 287, p. 107969 (cit. on p. 64).

Kerr, Yann H, Philippe Waldteufel, J-P Wigneron, JAMJ Martinuzzi, Jordi Font, and Michael Berger (2001). "Soil moisture retrieval from space: The Soil Moisture and Ocean Salinity (SMOS) mission". In: *IEEE transactions on Geoscience and remote sensing* 39.8, pp. 1729–1735 (cit. on p. 14).

Khabbazan, S, SC Steele-Dunne, P Vermunt, J Judge, M Vreugdenhil, and G Gao (2022). "The influence of surface canopy water on the relationship between L-band backscatter and biophysical variables in agricultural monitoring". In: *Remote Sensing of Environment* 268, p. 112789 (cit. on p. 78).

Kim, Seokhyeon, Yi Y Liu, Fiona M Johnson, Robert M Parinussa, and Ashish Sharma (2015). "A global comparison of alternate AMSR2 soil moisture products: Why do they differ?" In: *Remote Sensing of Environment* 161, pp. 43–62 (cit. on p. 21).

Kim, Seongkyun, Hyunglok Kim, and Minha Choi (2016). "Evaluation of satellite-based soil moisture retrieval over the korean peninsula: using AMSR2 LPRM algorithm and ground measurement data". In: *Journal of Korea Water Resources Association* 49.5, pp. 423–429 (cit. on p. 21).

Koch, Elisabeth, Ekko Bruns, Frank-M Chmielewski, Claudio Defila, Wolfgang Lipa, and Annette Menzel (2007). "Guidelines for plant phenological observations". In: *World Climate Data and Monitoring Programme* (cit. on p. 64).

Konings, Alexandra G, Maria Piles, Narendra Das, and Dara Entekhabi (2017). "L-band vegetation optical depth and effective scattering albedo estimation from SMAP". In: *Remote Sensing of Environment* 198, pp. 460–470 (cit. on p. 22).

Konings, Alexandra G, Krishna Rao, and Susan C Steele-Dunne (2019). "Macro to micro: microwave remote sensing of plant water content for physiology and ecology". In: *New Phytologist* 223.3, pp. 1166–1172 (cit. on p. 76).

Konings, Alexandra G, María Piles, Kathrina Rötzer, Kaighin A McColl, Steven K Chan, and Dara Entekhabi (2016). "Vegetation optical depth and scattering albedo retrieval using time series of dual-polarized L-band radiometer observations". In: *Remote sensing of environment* 172, pp. 178–189 (cit. on p. 76).

Koster, Randal D, Paul A Dirmeyer, Zhichang Guo, Gordon Bonan, Edmond Chan, Peter Cox, CT Gordon, Shinjiro Kanae, Eva Kowalczyk, David Lawrence, et al. (2004). "Regions of strong coupling between soil moisture and precipitation". In: *Science* 305.5687, pp. 1138–1140 (cit. on p. 14).

Lawrence, Heather, Jean-Pierre Wigneron, Philippe Richaume, Nathalie Novello, Jennifer Grant, Arnaud Mialon, Ahmad Al Bitar, Olivier Merlin, Dominique Guyon, Delphine Leroux, et al. (2014). "Comparison between SMOS Vegetation Optical Depth products and MODIS vegetation indices over crop zones of the USA". In: *Remote Sensing of Environment* 140, pp. 396–406 (cit. on p. 30).

Lechowicz, Martin J. (1984). "Why Do Temperate Deciduous Trees Leaf Out at Different Times? Adaptation and Ecology of Forest Communities". In: *The American Naturalist* 124.6, pp. 821–842 (cit. on pp. 53, 64).

Li, Xiaojun, Jean-Pierre Wigneron, Frédéric Frappart, Lei Fan, Philippe Ciais, Rasmus Fensholt, Dara Entekhabi, Martin Brandt, Alexandra G Konings, Xiangzhuo Liu, et al. (2021). "Global-scale assessment and inter-comparison of recently developed/reprocessed microwave satellite vegetation optical depth products". In: *Remote Sensing of Environment* 253, p. 112208 (cit. on p. 101).

Ling, Peter (2004). "A review of soil moisture sensors". In: *Assn. Flor. Prof. Bull* 886, pp. 22–23 (cit. on p. 14).

Liu, Yi Y, Richard AM De Jeu, Matthew F McCabe, Jason P Evans, and Albert IJM Van Dijk (2011). "Global long-term passive microwave satellite-based retrievals of vegetation optical depth". In: *Geophysical Research Letters* 38.18 (cit. on pp. 5, 15, 21, 30, 76).

Liu, Yi Y, Albert IJM Dijk, Matthew F McCabe, Jason P Evans, and Richard AM Jeu (2013). "Global vegetation biomass change (1988–2008) and attribution to environmental and human drivers". In: *Global ecology and biogeography* 22.6, pp. 692–705 (cit. on p. 21).

Martínez-Fernández, J, A González-Zamora, N Sánchez, A Gumuzzio, and CM Herrero-Jiménez (2016). "Satellite soil moisture for agricultural drought monitoring: Assessment of the SMOS derived Soil Water Deficit Index". In: *Remote Sensing of Environment* 177, pp. 277–286 (cit. on p. 14).

Matgen, P, S Heitz, S Hasenauer, C Hissler, L Brocca, L Hoffmann, W Wagner, and HHG Savenije (2012). "On the potential of MetOp ASCAT-derived soil wetness indices as a new aperture for hydrological monitoring and prediction: a field evaluation over Luxembourg". In: *Hydrological Processes* 26.15, pp. 2346–2359 (cit. on p. 15).

Mattia, Francesco, Thuy Le Toan, Ghislain Picard, Francesco I Posa, Angelo D'Alessio, Claudia Notarnicola, Anna Maria Gatti, Michele Rinaldi, Giuseppe Satalino, and Guido Pasquariello (2003). "Multitemporal C-band radar measurements on wheat fields". In: *IEEE transactions on geoscience and remote sensing* 41.7, pp. 1551–1560 (cit. on p. 63).

Matzler, Christian (1998). "Microwave permittivity of dry sand". In: *IEEE Transactions on Geoscience and Remote Sensing* 36.1, pp. 317–319 (cit. on p. 65).

McMaster, Gregory S. and W.W. Wilhelm (1997). "Growing degree-days: one equation, two interpretations". In: *Agricultural and Forest Meteorology* 87.4, pp. 291–300 (cit. on p. 53).

Melzer, T (2013). "Vegetation modelling in WARP 6.0". In: *Proc. EUMETSAT Meteorological Satellite Conf.* Pp. 1–7 (cit. on pp. 4, 20, 23, 30, 48, 78, 82).

Menzel, Annette, Tim H Sparks, Nicole Estrella, Elisabeth Koch, Anto Aasa, Rein Ahas, Kerstin Alm-Kübler, Peter Bissolli, Ol'ga Braslavská, Agrita Briede, et al. (2006). "European phenological response to climate change matches the warming pattern". In: *Global change biology* 12.10, pp. 1969–1976 (cit. on p. 42).

Miyaoka, Kengo, Alexander Gruber, Francesca Ticconi, Sebastian Hahn, Wolfgang Wagner, Julia Figa-Saldana, and Craig Anderson (2017). "Triple collocation analysis of soil moisture from Metop-A ASCAT and SMOS against JRA-55 and ERA-Interim". In: *IEEE Journal of Selected Topics in Applied Earth Observations and Remote Sensing* 10.5, pp. 2274–2284 (cit. on p. 101).

Mousa, BG and Hong Shu (2020). "Spatial evaluation and assimilation of SMAP, SMOS, and ASCAT satellite soil moisture products over Africa using statistical techniques". In: *Earth and Space Science* 7.1, e2019EA000841 (cit. on p. 101).

Muñoz Sabater, J (2019). *ERA5-Land hourly data from 1981 to present, Copernicus Climate Change Service (C3S) Climate Data Store (CDS)*. (Accessed on 28-Sep-2020) (cit. on pp. 84, 103).

Naeimi, Vahid, Zoltan Bartalis, and Wolfgang Wagner (2009a). "ASCAT soil moisture: An assessment of the data quality and consistency with the ERS scatterometer heritage". In: *Journal of Hydrometeorology* 10.2, pp. 555–563 (cit. on p. 77).

Naeimi, Vahid, Klaus Scipal, Zoltan Bartalis, Stefan Hasenauer, and Wolfgang Wagner (2009b). "An improved soil moisture retrieval algorithm for ERS and METOP scatterometer observations". In: *IEEE Transactions on Geoscience and Remote Sensing* 47.7, pp. 1999–2013 (cit. on pp. 4, 15, 18, 20, 23, 25, 46).

Nemani, Ramakrishna R, Charles D Keeling, Hirofumi Hashimoto, William M Jolly, Stephen C Piper, Compton J Tucker, Ranga B Myneni, and Steven W Running (2003). "Climate-driven increases in global terrestrial net primary production from 1982 to 1999". In: *science* 300.5625, pp. 1560–1563 (cit. on p. 84).

Njoku, Eni G and Dara Entekhabi (1996). "Passive microwave remote sensing of soil moisture". In: *Journal of hydrology* 184.1-2, pp. 101–129 (cit. on p. 22).

Owe, Manfred, Richard de Jeu, and Thomas Holmes (2008a). "Multisensor historical climatology of satellite-derived global land surface moisture". In: *Journal of Geophysical Research: Earth Surface* 113.F1 (cit. on p. 21).

– (2008b). "Multisensor historical climatology of satellite-derived global land surface moisture". In: *Journal of Geophysical Research: Earth Surface* 113.F1. eprint: `https://agupubs.onlinelibrary.wiley.com/doi/pdf/10.1029/2007JF000769` (cit. on p. 76).

Papagiannopoulou, Christina, Diego G Miralles, Stijn Decubber, Matthias Demuzere, Niko EC Verhoest, Wouter A Dorigo, and Willem Waegeman (2017). "A non-linear Granger-causality framework to investigate climate–vegetation dynamics". In: *Geoscientific Model Development* 10.5, pp. 1945–1960 (cit. on p. 88).

Parinussa, Robert M, Thomas RH Holmes, Niko Wanders, Wouter A Dorigo, and Richard AM de Jeu (2015). "A preliminary study toward consistent soil moisture from AMSR2". In: *Journal of Hydrometeorology* 16.2, pp. 932–947 (cit. on pp. 14, 21).

Perry, Thomas O (1971). "Dormancy of trees in winter". In: *Science* 171.3966, pp. 29–36 (cit. on p. 45).

Petchiappan, Ashwini, Susan C Steele-Dunne, Mariette Vreugdenhil, Sebastian Hahn, Wolfgang Wagner, and Rafael Oliveira (2021). "The influence of vegetation water dynamics on the ASCAT backscatter-incidence angle relationship in the Amazon". In: *Hydrology and Earth System Sciences Discussions*, pp. 1–29 (cit. on pp. 102, 105, 108).

Pfeil, Isabella, Mariette Vreugdenhil, Sebastian Hahn, Wolfgang Wagner, Peter Strauss, and Günter Blöschl (2018). "Improving the seasonal representation of ASCAT soil moisture and vegetation dynamics in a temperate climate". In: *Remote Sensing* 10.11, p. 1788 (cit. on pp. 43, 48, 78, 90, 101).

Pfeil, Isabella, Felix Reuß, Mariette Vreugdenhil, Claudio Navacchi, and Wolfgang Wagner (2020a). "Classification of Wheat and Barley Fields Using Sentinel-1 Backscatter". In: *IGARSS 2020-2020 IEEE International Geoscience and Remote Sensing Symposium*. IEEE, pp. 140–143 (cit. on p. 107).

Pfeil, Isabella, Wolfgang Wagner, Matthias Forkel, Wouter Dorigo, and Mariette Vreugdenhil (2020b). "Does ASCAT observe the spring reactivation in temperate deciduous broadleaf forests?" In: *Remote Sensing of Environment* 250, p. 112042 (cit. on pp. 77, 83).

Pierdicca, Nazzareno, Fabio Fascetti, Luca Pulvirenti, Raffaele Crapolicchio, and Joaquin Muñoz-Sabater (2015). "Analysis of ASCAT, SMOS, in-situ and land model soil moisture as a regionalized variable over Europe and North Africa". In: *Remote Sensing of Environment* 170, pp. 280–289 (cit. on p. 101).

Pitts, David E, Gautam D Badhwar, and E Reyna (1987). "Estimation of biophysical properties of forest canopies using C-band microwave data". In: *Advances in Space Research* 7.11, pp. 89–95 (cit. on p. 45).

Polgar, Caroline A. and Richard B. Primack (2011). "Leaf-out phenology of temperate woody plants: from trees to ecosystems". In: *New Phytologist* 191, pp. 926–941 (cit. on pp. 45, 53).

Proisy, Christophe, Eric Mougin, Eric Dufrêne, and Valérie Le Dantec (2000). "Monitoring seasonal changes of a mixed temperate forest using ERS SAR observations". In: *IEEE Transactions on Geoscience and Remote Sensing* 38.1, pp. 540–552 (cit. on p. 45).

Quast, Raphael and Wolfgang Wagner (2016). "Analytical solution for first-order scattering in bistatic radiative transfer interaction problems of layered media". In: *Applied optics* 55.20, pp. 5379–5386 (cit. on p. 78).

Richards, John A, Guo-qing Sun, and David S Simonett (1987). "L-band radar backscatter modeling of forest stands". In: *IEEE Transactions on Geoscience and Remote Sensing* 4, pp. 487–498 (cit. on p. 65).

Richardson, Andrew D, Amey Schenck Bailey, Ellen G Denny, C Wayne Martin, and JOHN O'KEEFE (2006). "Phenology of a northern hardwood forest canopy". In: *Global Change Biology* 12.7, pp. 1174–1188 (cit. on p. 66).

Richardson, Andrew D, Koen Hufkens, Thomas Milliman, Donald M Aubrecht, Morgan E Furze, Bijan Seyednasrollah, Misha B Krassovski, John M Latimer, W Robert Nettles, Ryan R Heiderman, et al. (2018). "Ecosystem warming extends vegetation activity but heightens vulnerability to cold temperatures". In: *Nature* 560.7718, pp. 368–371 (cit. on p. 43).

Richardson, Andrew D., Trevor F. Keenan, Mirco Migliavacca, Youngryel Ryu, Oliver Sonnentag, and Michael Toomey (2013). "Climate change, phenology, and phenological control of vegetation feedbacks to the climate system". In: *Agricultural and Forest Meteorology* 169, pp. 156–173 (cit. on pp. 42, 66).

Rodell, M, PR Houser, UEA Jambor, J Gottschalck, K Mitchell, CJ Meng, K Arsenault, B Cosgrove, J Radakovich, M Bosilovich, et al. (2004). "The Global Land Data Assimilation System". In: *Bulletin of the American Meteorological Society* 85.3, pp. 381–394 (cit. on p. 22).

Rodell, Matthew, Isabella Velicogna, and James S Famiglietti (2009). "Satellite-based estimates of groundwater depletion in India". In: *Nature* 460.7258, p. 999 (cit. on p. 14).

Rohde, Antje, Catherine Bastien, and Wout Boerjan (2011). "Temperature signals contribute to the timing of photoperiodic growth cessation and bud set in poplar". In: *Tree physiology* 31.5, pp. 472–482 (cit. on p. 43).

Rubel, Franz, Katharina Brugger, Klaus Haslinger, and Ingeborg Auer (2017). "The climate of the European Alps: Shift of very high resolution Köppen-Geiger climate zones 1800-2100". In: 26.2, pp. 115–125 (cit. on p. 46).

Rüetschi, Marius, Michael E Schaepman, and David Small (2018). "Using multitemporal sentinel-1 c-band backscatter to monitor phenology and classify deciduous and coniferous forests in northern switzerland". In: *Remote Sensing* 10.1, p. 55 (cit. on p. 45).

Saatchi, Sassan, Kerry Halligan, Don G. Despain, and Robert L. Crabtree (2007). "Estimation of Forest Fuel Load From Radar Remote Sensing". In: *IEEE Transactions on Geoscience and Remote Sensing* 45.6, pp. 1726–1740 (cit. on p. 76).

Santoro, Maurizio, André Beaudoin, Christian Beer, Oliver Cartus, Johan E.S. Fransson, Ronald J. Hall, Carsten Pathe, Christiane Schmullius, Dmitry Schepaschenko, Anatoly Shvidenko, Martin Thurner, and Urs Wegmüller (2015). "Forest growing stock volume of the northern hemisphere: Spatially explicit estimates for 2010 derived from Envisat ASAR". In: *Remote Sensing of Environment* 168, pp. 316–334 (cit. on p. 76).

Sanz-Pérez, V, P Castro-Díez, and F Valladares (2009). "Differential and interactive effects of temperature and photoperiod on budburst and carbon reserves in two co-occurring Mediterranean oaks". In: *Plant Biology* 11.2, pp. 142–151 (cit. on p. 53).

Satalino, Giuseppe, Anna Balenzano, Francesco Mattia, and Malcolm WJ Davidson (2013). "C-band SAR data for mapping crops dominated by surface or volume scattering". In: *IEEE Geoscience and Remote Sensing Letters* 11.2, pp. 384–388 (cit. on pp. 63, 65).

Schmugge, T, P Gloersen, Tom Wilheit, and F Geiger (1974). "Remote sensing of soil moisture with microwave radiometers". In: *Journal of Geophysical Research* 79.2, pp. 317–323 (cit. on p. 21).

Schoch, Werner, I Heller, Fritz Hans Schweingruber, and Felix Kienast (2004). *Wood anatomy of central European Species*. Accessed: 2020-02-14. Swiss Federal Institute for Forest (cit. on p. 60).

Seneviratne, Sonia I., Thierry Corti, Edouard L. Davin, Martin Hirschi, Eric B. Jaeger, Irene Lehner, Boris Orlowsky, and Adriaan J. Teuling (2010). "Investigating soil moisture–climate interactions in a changing climate: A review". In: *Earth-Science Reviews* 99.3, pp. 125–161 (cit. on p. 76).

Shutko, AM (1986). "Microwave radiometry of water surface and grounds". In: *M., Nauka*, p. 189 (cit. on p. 22).

Sinha, S, C Jeganathan, LK Sharma, and MS Nathawat (2015). "A review of radar remote sensing for biomass estimation". In: *International Journal of Environmental Science and Technology* 12.5, pp. 1779–1792 (cit. on p. 45).

Soulis, Konstantinos X, Stamatios Elmaloglou, and Nicholas Dercas (2015). "Investigating the effects of soil moisture sensors positioning and accuracy on soil moisture based drip irrigation scheduling systems". In: *Agricultural Water Management* 148, pp. 258–268 (cit. on p. 14).

Steele-Dunne, Susan C, Sebastian Hahn, Wolfgang Wagner, and Mariette Vreugdenhil (2019). "Investigating vegetation water dynamics and drought using Metop ASCAT over the North American Grasslands". In: *Remote Sensing of Environment* 224, pp. 219–235 (cit. on pp. 4, 43, 62, 77, 83, 105, 108).

– (2021). "Towards including dynamic vegetation parameters in the EUMETSAT H SAF ASCAT soil moisture products". In: *Remote Sensing* 13.8, p. 1463 (cit. on pp. 78, 101).

Sun, Guoqing and K Jon Ranson (1995). "A three-dimensional radar backscatter model of forest canopies". In: *IEEE Transactions on Geoscience and Remote Sensing* 33.2, pp. 372–382 (cit. on p. 65).

Svoboda, Mark, Doug LeComte, Mike Hayes, Richard Heim, Karin Gleason, Jim Angel, Brad Rippey, Rich Tinker, Mike Palecki, David Stooksbury, et al. (2002). "The drought monitor". In: *Bulletin of the American Meteorological Society* 83.8, pp. 1181–1190 (cit. on p. 14).

Templ, Barbara, Elisabeth Koch, Kjell Bolmgren, Markus Ungersböck, Anita Paul, Helfried Scheifinger, This Rutishauser, Montserrat Busto, Frank-M Chmielewski, Lenka Hájková, Sabina Hodzić, Frank Kaspar, Barbara Pietragalla, Ramiro Romero-Fresneda, Anne Tolvanen, Višnja Vučetič, Kirsten Zimmermann, and Ana Zust (2018). "Pan European Phenological database (PEP725): a single point of access for European data." In: (cit. on p. 48).

Teubner, Irene E., Matthias Forkel, Martin Jung, Yi Y. Liu, Diego G. Miralles, Robert Parinussa, Robin van der Schalie, Mariette Vreugdenhil, Christopher R. Schwalm, Gianluca Tramontana, Gustau Camps-Valls, and Wouter A. Dorigo (2018). "Assessing the relationship between microwave vegetation optical depth and gross primary production". In: *International Journal of Applied Earth Observation and Geoinformation* 65, pp. 79–91 (cit. on p. 76).

Tian, Feng, Martin Brandt, Yi Y Liu, Aleixandre Verger, Torbern Tagesson, Abdoul A Diouf, Kjeld Rasmussen, Cheikh Mbow, Yunjia Wang, and Rasmus Fensholt (2016). "Remote sensing of vegetation dynamics in drylands: Evaluating vegetation optical depth (VOD) using AVHRR NDVI and in situ green biomass data over West African Sahel". In: *Remote Sensing of Environment* 177, pp. 265–276 (cit. on pp. 15, 21).

Toté, Carolien, Else Swinnen, Sindy Sterckx, Dennis Clarijs, Carine Quang, and Ronny Maes (2017). "Evaluation of the SPOT/VEGETATION Collection 3 reprocessed dataset: Surface reflectances and NDVI". In: *Remote Sensing of Environment* 201, pp. 219–233 (cit. on p. 65).

Ulaby, Fawwaz T (1981). "Microwave remote sensing". In: *Active and passive* (cit. on p. 79).

Ulaby, Fawwaz T and RP Jedlicka (1984). "Microwave dielectric properties of plant materials". In: *IEEE Transactions on Geoscience and Remote Sensing* 4, pp. 406–415 (cit. on p. 65).

Ulaby, Fawwaz T and William H Stiles (1980). "The active and passive microwave response to snow parameters: 2. Water equivalent of dry snow". In: *Journal of Geophysical Research: Oceans* 85.C2, pp. 1045–1049 (cit. on p. 65).

Ulaby, Fawwaz T., Richard K. Moore, and Adrian K. Fung (1981). *Microwave Remote Sensing Active and Passive-Volume I: Microwave Remote Sensing Fundamentals and Radiometry* (cit. on pp. 3, 65).

Veloso, Amanda, Stéphane Mermoz, Alexandre Bouvet, Thuy Le Toan, Milena Planells, Jean-François Dejoux, and Eric Ceschia (2017). "Understanding the temporal behavior of crops using Sentinel-1 and Sentinel-2-like data for agricultural applications". In: *Remote sensing of environment* 199, pp. 415–426 (cit. on p. 63).

Vermunt, Paul C., Saeed Khabbazan, Susan C. Steele-Dunne, Jasmeet Judge, Alejandro Monsivais-Huertero, Leila Guerriero, and Pang-Wei Liu (2021). "Response of Subdaily L-Band Backscatter to Internal and Surface Canopy Water Dynamics". In: *IEEE Transactions on Geoscience and Remote Sensing* 59.9, pp. 7322–7337 (cit. on pp. 78, 89).

Vitasse, Yann, Annabel Josée Porté, Antoine Kremer, Richard Michalet, and Sylvain Delzon (2009). "Responses of canopy duration to temperature changes in four temperate tree species: relative contributions of spring and autumn leaf phenology". In: *Oecologia* 161.1, pp. 187–198 (cit. on p. 66).

VITO (2017). *Copernicus Global Land Operations "Vegetation and Energy", "CGLOPS-1". Product User Manual Leaf Area Index (LAI), Collection 1 km, Version 1, Issue I2.40.* https://land.copernicus.eu/global/sites/cgls.vito.be/files/products/CGLOPS1_PUM_LAI1km-V1_I2.40.pdf. Accessed: 2020-02-12 (cit. on p. 49).

– (2019). *Copernicus Global Land Operations "Vegetation and Energy", "CGLOPS-1". Product User Manual Leaf Area Index (LAI) - Version 1, SPOT/VGT.* https://land.copernicus.eu/global/sites/cgls.vito.be/files/products/CGLOPS1_PUM_LAI1km-VGT-V1_I1.20.pdf. Accessed: 2020-02-12 (cit. on p. 50).

Vreugdenhil, Mariette, Wouter A Dorigo, Wolfgang Wagner, Richard AM de Jeu, Sebastian Hahn, and Margreet JE van Marle (2016). "Analyzing the Vegetation Parameterization in the TU-Wien ASCAT Soil Moisture Retrieval". In: *IEEE Transactions on Geoscience and Remote Sensing* 54.6, pp. 3513–3531 (cit. on pp. 3, 5, 15, 18, 20, 23, 30, 43, 46, 48, 76–78, 83, 105).

Vreugdenhil, Mariette, Sebastian Hahn, Thomas Melzer, Bernhard Bauer-Marschallinger, Christoph Reimer, Wouter Arnoud Dorigo, and Wolfgang Wagner (2017). "Assessing vegetation dynamics over mainland Australia with metop ASCAT". In: *IEEE Journal of Selected Topics in Applied Earth Observations and Remote Sensing* 10.5, pp. 2240–2248 (cit. on pp. 4, 21, 30, 32, 43, 105).

Vreugdenhil, Mariette, Wolfgang Wagner, Bernhard Bauer-Marschallinger, Isabella Pfeil, Irene Teubner, Christoph Rüdiger, and Peter Strauss (2018). "Sensitivity of Sentinel-1 backscatter to vegetation dynamics: An Austrian case study". In: *Remote Sensing* 10.9, p. 1396 (cit. on pp. 63, 107).

Wagner, Wolfgang (1998). "Soil moisture retrieval from ERS scatterometer data". PhD thesis. Citeseer (cit. on p. 25).

Wagner, Wolfgang, Guido Lemoine, Maurice Borgeaud, and Helmut Rott (1999a). "A Study of Vegetation Cover Effects on ERS Scatterometer Data". In: *IEEE Transactions on Geoscience and Remote Sensing* 37.2, pp. 938–948 (cit. on pp. 3, 20, 43, 77).

Wagner, Wolfgang, Guido Lemoine, and Helmut Rott (1999b). "A method for estimating soil moisture from ERS scatterometer and soil data". In: *Remote sensing of environment* 70.2, pp. 191–207 (cit. on pp. 3, 4, 14, 18, 20, 46, 77).

Wagner, Wolfgang, Josef Noll, Maurice Borgeaud, and Helmut Rott (1999c). "Monitoring soil moisture over the Canadian Prairies with the ERS scatterometer". In: *IEEE Transactions on Geoscience and Remote Sensing* 37.1, pp. 206–216 (cit. on pp. 3, 4, 18, 20, 43, 46, 65, 77, 78, 81–83).

Wagner, Wolfgang, Wouter Dorigo, Richard de Jeu, Diego Fernandez, Jerome Benveniste, Eva Haas, and Martin Ertl (2012). "Fusion of active and passive microwave observations to create an essential climate variable data record on soil moisture". In: *ISPRS Annals of the Photogrammetry, Remote Sensing and Spatial Information Sciences (ISPRS Annals)* 7, pp. 315–321 (cit. on p. 14).

Wagner, Wolfgang, Sebastian Hahn, Richard Kidd, Thomas Melzer, Zoltan Bartalis, Stefan Hasenauer, Julia Figa-Saldana, Patricia De Rosnay, Alexander Jann, Stefan Schneider, et al. (2013). "The ASCAT soil moisture product: A review of its specifications, validation results, and emerging applications". In: *Meteorologische Zeitschrift* (cit. on pp. 2, 14, 15, 19, 27, 76).

Wagner, Wolfgang, Luca Brocca, Vahid Naeimi, Rolf Reichle, Clara Draper, Richard de Jeu, Dongryeol Ryu, Chun-Hsu Su, Andrew Western, Jean-Christophe Calvet, et al. (2014). "Clarifications on the "Comparison between SMOS, VUA, ASCAT, and ECMWF soil moisture products over four watersheds in US"". In: *IEEE Transactions on Geoscience and Remote Sensing* 52.3, pp. 1901–1906 (cit. on pp. 15, 34).

Wanders, N, D Karssenberg, A de Roo, SM De Jong, and MFP Bierkens (2014a). "The suitability of remotely sensed soil moisture for improving operational flood forecasting". In: *Hydrology and Earth System Sciences* 18.6, pp. 2343–2357 (cit. on p. 14).

Wanders, Niko, Marc FP Bierkens, Steven M de Jong, Ad de Roo, and Derek Karssenberg (2014b). "The benefits of using remotely sensed soil moisture in parameter identification of large-scale hydrological models". In: *Water resources research* 50.8, pp. 6874–6891 (cit. on p. 14).

Way, Danielle A (2011). "Tree phenology responses to warming: spring forward, fall back?" In: *Tree physiology* 31.5, pp. 469–471 (cit. on p. 43).

Wolf, Sebastian, Trevor F Keenan, Joshua B Fisher, Dennis D Baldocchi, Ankur R Desai, Andrew D Richardson, Russell L Scott, Beverly E Law, Marcy E Litvak, Nathaniel A Brunsell, et al. (2016). "Warm spring reduced carbon cycle impact of the 2012 US summer drought". In: *Proceedings of the National Academy of Sciences* 113.21, pp. 5880–5885 (cit. on p. 42).

Xiao, Xiangming, Junhui Zhang, Huimin Yan, Weixing Wu, and Chandrashekhar Biradar (2009). "Land surface phenology". In: *Phenology of ecosystem processes*. Springer, pp. 247–270 (cit. on pp. 42, 66).

Xu, Shuai, Zhixin Qi, Xia Li, and Anthony Gar-On Yeh (2019). "Investigation of the effect of the incidence angle on land cover classification using fully polarimetric SAR images". In: *International Journal of Remote Sensing* 40.4, pp. 1576–1593 (cit. on p. 80).

Al-Yaari, Amen, J-P Wigneron, Agnès Ducharne, Yann H Kerr, Wolfgang Wagner, Gabrielle De Lannoy, Rolf Reichle, Ahmad Al Bitar, Wouter Dorigo, Philippe Richaume, et al. (2014). "Global-scale comparison of passive (SMOS) and active (ASCAT) satellite based microwave soil moisture retrievals with soil moisture simulations (MERRA-Land)". In: *Remote Sensing of Environment* 152, pp. 614–626 (cit. on p. 101).

Yebra, Marta, Philip E Dennison, Emilio Chuvieco, David Riano, Philip Zylstra, E Raymond Hunt Jr, F Mark Danson, Yi Qi, and Sara Jurdao (2013). "A global review of remote sensing of live fuel moisture content for fire danger assessment: Moving towards operational products". In: *Remote Sensing of Environment* 136, pp. 455–468 (cit. on p. 66).

Yee, Mei Sun, Jeffrey P Walker, Christoph Rüdiger, Robert M Parinussa, Toshio Koike, and Yann H Kerr (2017). "A comparison of SMOS and AMSR2 soil moisture using representative sites of the OzNet monitoring network". In: *Remote Sensing of Environment* 195, pp. 297–312 (cit. on p. 21).

Young-Robertson, Jessica M., W. Robert Bolton, Uma S. Bhatt, Jordi Cristóbal, and Richard Thoman (2016). "Deciduous trees are a large and overlooked sink for snowmelt water in the boreal forest". In: *Scientific Reports* 6.1, p. 29504 (cit. on pp. 45, 107).

Zreda, M, WJ Shuttleworth, X Zeng, C Zweck, D Desilets, T Franz, and R Rosolem (2012). "COSMOS: the cosmic-ray soil moisture observing system". In: *Hydrology and Earth System Sciences* 16.11, pp. 4079–4099 (cit. on p. 21).